A spectral and timing study of MAXI J1820+070 during outburst

A dissertation submitted in partial fulfilment of the
requirements for the degree of
Master of Science in Astronomy
Department of Astronomy
University of Cape Town

Author:
Kyle Solomons

January 2024

Supervisors:
Dr. Sunil Chandra
Dr. Itumeleng Monageng

I, Kyle Solomons, hereby declare that the work presented in this thesis, titled "A spectral and timing study of MAXI J1820+070 during it's outburst", is entirely my own. I affirm that all ideas, concepts, data, and written content contained within this thesis are the result of my own intellectual efforts and research unless otherwise acknowledged through proper citation.

Abstract

Black Hole X-ray binaries (BHXRBs) represent a unique class of astrophysical systems where a stellar-mass black hole accretes matter from a companion star via accretion disks. The accretion disk emits in X-ray and UV because of the radiative losses. The transfer of matter can occur through continuous donor supply or episodic capturing of material from stellar winds, leading to sudden enhancements in X-ray flux known as outbursts. The instabilities in the disk, the geometry of the inner disk, the coupling between the disk and corona, etc, also contribute to the observed variability. The exploration of BHXBs contributes significantly to our understanding of the broader astrophysical landscape. These offer a unique testing ground for theories related to accretion physics, extreme gravity, jet formation, and the evolution of binary systems. Moreover, the BHXBs play a pivotal role in shaping galactic dynamics and evolution in their neighbourhood. Among the myriad BHXBs, MAXI J1820+070 stands out as a particularly intriguing target. This low-mass X-ray binary, located in the constellation Ophiuchus, garnered attention due to its exceptional outburst in March of 2018. The intense luminosity of MAXI J1820+070, which reached a peak X-ray flux of $\sim$ 4 Crab, allowed for detailed multi-wavelength campaigns, facilitating comprehensive investigations into its properties and behaviour. MAXI J1820+070 provides a unique opportunity to deepen our understanding of accretion processes near black holes, enabling the refinement of theoretical models and enhancing our ability to interpret observations across the electromagnetic spectrum.

This study presents a comprehensive analysis of the archival X-ray data of MAXI J1820+070 from *Nu*STAR, *NICER*, and *Swift*-XRT. The investigation focusses primarily on the system's spectral properties and timing characteristics. Spectral evolution and transitions between the hard and soft states are examined, with key parameters defining these states extracted. The inner disk radius was constrained to $\lesssim$ 2.6 ISCO, extending down to 1.5 ISCO before the state transition. The disk temperature steadily increases from 0.71 keV, peaking at 0.8 keV. Our simplistic spectral model prefers different inclinations at various stages of the outburst, varying from $\sim$ 45 to 73 degrees, probably due to the model's limitations. Furthermore, the power-law index was restricted to $\sim$ 1.6 and the coronal electron temperature to $\sim$24-38 keV. We identify the presence and evolution of quasi-periodic oscillations and quantify them through Lorentzian curve fitting. Additionally, we identified hard and soft time lags, varying in amplitude and frequency during the outburst. Together, the spectral and timing results suggest a QPO originating from the corona, with the corona contracting during the hard state and expanding during the state transition. Possible signatures of outflows are detected through absorption features between 6.9-7.3 keV.

Contents

List of Figures

List of Tables

1 Introduction

In the realm of celestial phenomena, binary star systems are a significant focus of astronomical research. Representing up to 85% of the stellar population (Australia Telescope National Facility, 1999), these systems consist of two stars bound by gravity, providing valuable insights into dynamic cosmic processes. Within this category, compact binaries are particularly noteworthy, often featuring remnants of massive stars such as white dwarfs, neutron stars, or black holes. These remnants are essential for understanding the complexities of stellar evolution. Interactions within compact binaries serve as a unique laboratory for studying extreme physical conditions, thereby offering critical insights into specific stages of stellar life cycles. This section provides a detailed overview of a specific subset of compact binaries – the X-ray binary class – and highlights their significance. The comprehensive scope of this study involves analyzing the accretion dynamics within the binary system MAXI J1820+070..

1.1 X-ray binaries

The X-ray binary (XRB) is a binary system comprising a compact object accreting mass from a donor star via an accretion disk. As the name implies, X-ray binaries are highly luminous in the X-rays, with most of the X-ray radiation emanating from an accretion disk. XRBs are divided into two classes based on the mass of the donor star: low-mass XRBs for systems with a donor star of $\lesssim 1$ $M_\odot$ and high-mass X-ray binaries for donor stars with mass $\gtrsim 10$ $M_\odot$ (Jorge Casares et al., 2017).

The energy generated by XRBs arises from the transformation of gravitational energy into radiation across the electromagnetic spectrum as material is accreted onto the compact object. Consider a body of mass M and radius R, where the gravitational potential energy released during the accretion of mass m onto the central object's surface is given by

$$\Delta E_{\text{acc}} = \frac{GMm}{R}$$

Assuming a steady spherically symmetrical accretion flow, the maximum luminosity is constrained by the Eddington luminosity:

$$L_{\text{Edd}} \approx 1.3 \times 10^{38} \left(\frac{M}{M_\odot} \right) \text{erg/s}$$

Beyond this limit, radiation pressure prevails over gravitational binding forces, leading to the suppression of the accretion flow. Assuming all kinetic energy of infalling matter is radiated at the central object's surface, the accretion luminosity is given by

$$L_{\text{acc}} = \frac{GM\dot{M}}{R}$$

where $\dot{M}$ ($g\ s^{-1}$) is the mass accretion rate. However, for a black hole, characterized by its immaterial surface with a radius defined by the Schwarzschild radius $R_s = \frac{2GM}{c^2}$, the nature of accretion changes. As R_s does not denote a physical surface but rather the boundary at which matter becomes trapped, a fraction of the accretion energy is

expected to be absorbed into the black hole rather than radiated away. The accretion luminosity for a black hole is then expressed as

$$\begin{aligned} L_{\text{acc}} &= 2\eta M\dot{M}/R_s \\ &= \eta\dot{M}c^2 \end{aligned}$$

Here, η represents the efficiency parameter, quantifying how effectively the rest mass of the infalling material converts to radiation.

While X-ray binaries emit most of their energy in the X-rays, these systems emit across a large energy range. Figure 1 depicts a schematic representation of an XRB indicating the various emitting regions and their associated energies. These regions include the companion star, the compact central object, the accretion disk, the companion star, the corona and a transient relativistic jet. Γ in Fig. 1 refers to the bulk Lorentz factor: $1/\sqrt{1-\frac{v^2}{c^2}}$ where v is the speed of the material and c is the speed of light, which is used to describe how time, length and other physical properties of matter change when at a significant fraction of the speed of light.

The mass transfer in low-mass X-ray binaries (LMXRBs) is facilitated by the Roche-lobe overflow mechanism, depicted in Figure 2(b). When the companion star exceeds its Roche lobe, the teardrop-shaped region containing gravitationally bound material, the efficient transfer of mass occurs through a stream flowing via the first Lagrangian point. After traversing this point, the material orbits the compact object, spiralling inward as it loses angular momentum through viscous interactions, forming what is commonly known as an accretion disk (Savonije, 1978). High-mass X-ray binaries (HMXRBs) are known to undergo mass transfer via robust stellar winds emanating from the companion star, as illustrated in Figure 2(a). These winds effectively remove mass from the system, subsequently captured by the compact object, thereby fueling its activity. However, other forms of mass accretion such as Roche-lobe overflow may also contribute to the mass transfer within these systems (Kretschmar et al., 2016) In the Be/X-ray binary subclass, featuring a fast-rotating Be star as the donor and a neutron star, an equatorial disk surrounds the companion star, however, the process by which it forms is not fully understood. This disk becomes a significant site for interactions, where the neutron star may collide and accrete matter powering the emission of X-rays (Reig, 2011).

XRBs which contain a compact object too massive to be a neutron or degenerate star (i.e. $M > 3\ M_\odot$) are known as black hole binaries (BHBs). BHBs offer a distinctive environment for investigating the accretion process onto an extremely compact object and the highly curved space-time surrounding a black hole. The strong gravitational field in this region presents an opportunity to study the important effects of General Relativity (e.g. Psaltis, 2008). The first BHB, Cygnus X-1, was discovered in the early years of X-ray astronomy using instruments onboard sounding rockets. The observation of its binary nature and the subsequent estimation of the mass of its compact object allowed it to become the first candidate for a black hole system. Cyg X-1's X-ray properties were characterized by strong fluctuations on short time scales and an extremely hard energy spectrum. Due to its perpetual high accretion rate and high X-ray luminosity emission ($> 10^{37}$ erg/s), Cyg X-1 is classified as a persistent system.

Although Cyg X-1 is a persistent system, these types of systems are relatively uncommon. Most BHBs are transient and can be challenging to identify without the aid of a wide-field X-ray instrument.

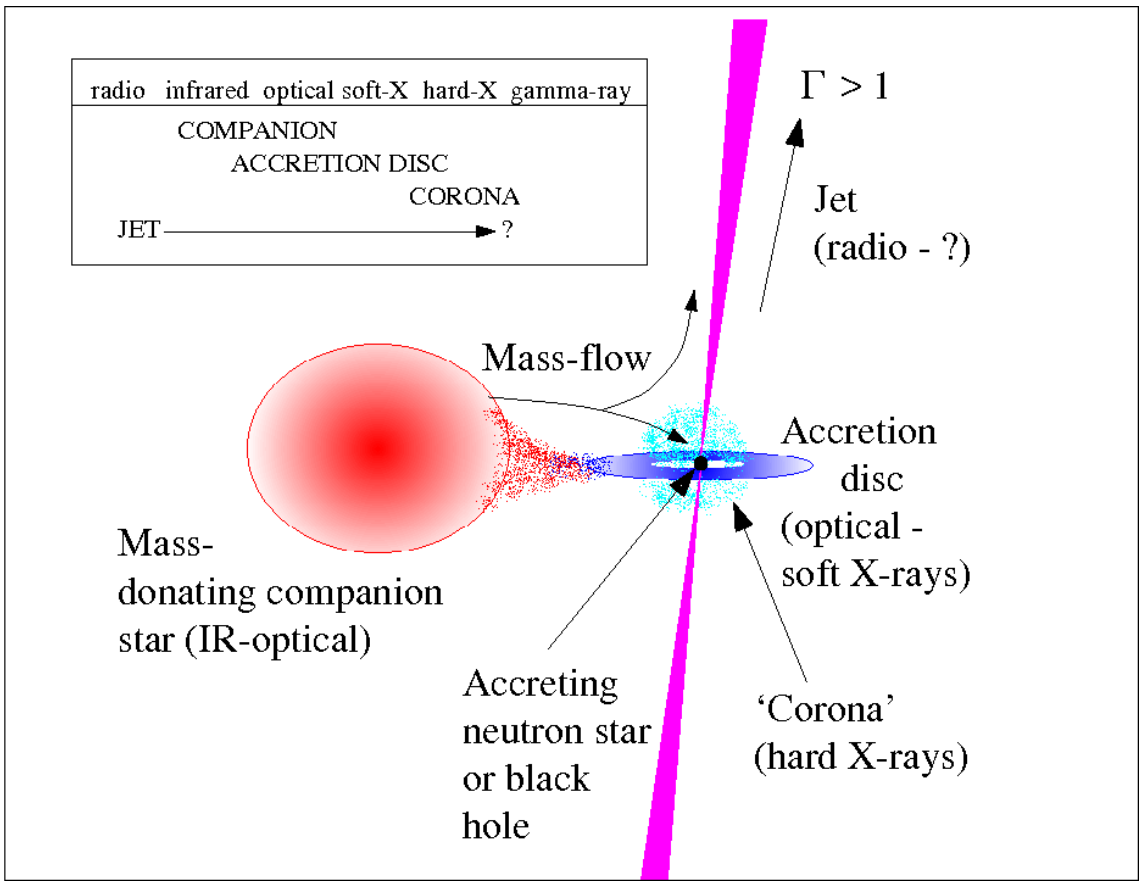

Figure 1: A schematic diagram depicting the geometry of a typical X-ray binary system, indicating the locations associated with the observed emissions across various wavelengths (source: Rob Fender, 2001).

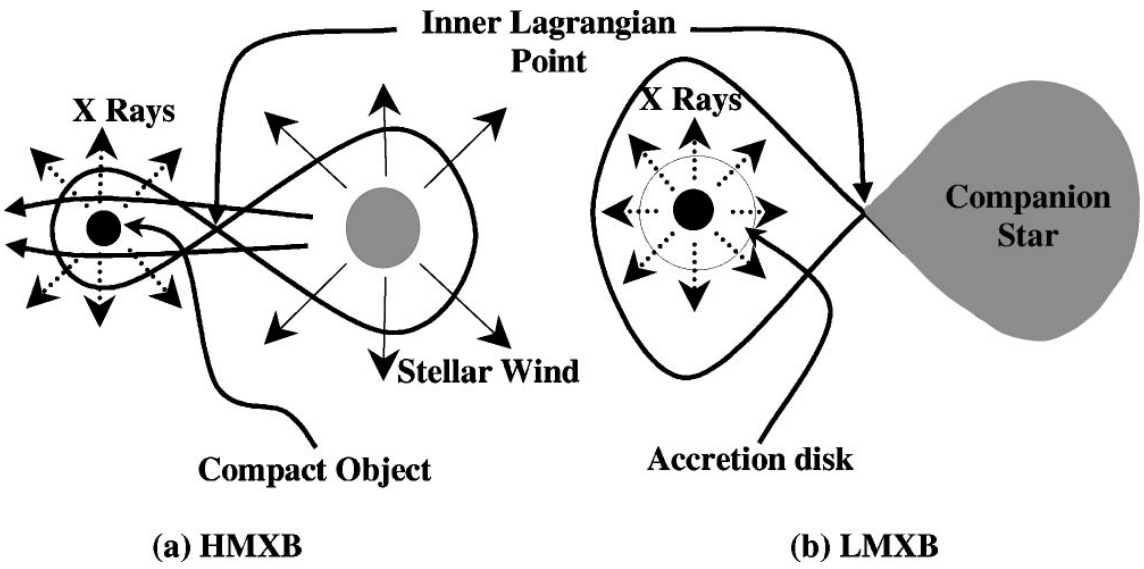

Figure 2: Schematic of the mass transfer mechanisms in XRBs. (a) HMXRB system with mass transfer via stellar wind (b) LMXRB with mass transfer via Roche-lobe overflow. (source: Moret et al., 2003)

In the realm of general relativity, the so-called "no-hair theorem" (Carter, 1971) states that a black hole can be fully characterized by three intrinsic parameters:it's mass (M), electric charge (Q) and its specific angular momentum or spin ($a = J/cM$), where J signifies the angular momentum of the black hole, and c is the speed of light. The spin is commonly represented as a dimensionless spin parameter, $a^* = a/R_g$, with R_g defined as the gravitational radius, given by $R_g \equiv GM/c^2$. The mass establishes a scale for the black hole, while the spin influences the geometric properties. While black holes theoretically possess an electric charge, it is expected to be negligible. The spin parameter varies between 0, indicating a non-rotating 'Schwarzschild' black hole, and 1, signifying a maximally rotating 'Kerr' black hole. A fundamental feature of a black hole is its event horizon—a theoretical boundary that marks the innermost region from which no mass or light can escape, owing to the overwhelming gravitational force exerted by the black hole. Beyond this boundary, there exists another boundary known as the innermost stable circular orbit (ISCO), where any matter will inevitably succumb to the gravitational pull and free-fall into the black hole (see e.g. Kato et al., 2008 and Shapiro and Teukolsky, 1983). The ISCO depends on the mass and spin of the black hole. For a Schwarzschild black hole ($a^* = 0$), the event horizon has a radius of $R_S = 2R_g = 30\text{km}(M/10M_\odot)$, the ISCO is positioned at $R_{\text{ISCO}} = 6R_g$, and the corresponding maximum orbital frequency is $\nu_{\text{ISCO}} = 220\text{Hz}(M/10M_\odot)^{-1}$. In the case of an extreme Kerr black hole ($a^* = 1$), both the event horizon and the ISCO radii (for prograde orbits) coincide, denoted as $R_K = R_{\text{ISCO}} = R_g$, and the maximum orbital frequency is $\nu_{\text{ISCO}} = 1615\text{Hz}(M/10M_\odot)^{-1}$.

In the past, stellar-mass black holes were primarily investigated in the X-ray spectrum. However, advancements in observations, particularly in the infrared and radio domains, have revealed additional phenomena, including the ejection of relativistic jets perpendicular to the accretion disk. These relativistic jets, in conjunction with non-relativistic wind-like outflows, contribute to an accretion-ejection paradigm. In this framework, the jets and outflows serve as mechanisms to carry away accretion

energy into the surrounding environment. It is hypothesized that the launching of these jets is somehow linked to the accretion process. Nevertheless, the precise cause-and-effect relationship between accretion and ejection, as well as the mechanisms responsible for launching, collimating, and accelerating relativistic jets and wind-like outflows, remain open questions.

1.2 Exploring Black Hole X-ray Binaries through X-ray Observations

BHBs typically spend the majority of their existence in a quiescent state, which is characterized by an X-ray luminosity of around 10^{32} erg/s and with a spectrum that is distinctly non-thermal and hard. BHBs are known to enter a phase of dramatically increased accretion, known as an outburst, where the source can produce peak luminosities ranging from 10^{36} to 10^{39} ergs/s and can persist for a period of a few weeks to several months (Tetarenko et al., 2016). However, some XRBs have been observed to undergo an extended outburst that can persist for many years, such as GRS 1915+105 and 4U 1755-338 (S.E. Motta et al., 2021). Most BHBs are discovered undergoing an outburst. This phase is characterized by transitions between different spectral states, most notably the thermal, disc-dominated state and the non-thermal, Comptonization-dominated state, historically referred to as the high/soft state (HSS) and low/hard state (LHS) respectively. X-ray outbursts that persist for a few weeks to several months are thought to be caused by instabilities that originate within the accretion disk. As the accretion rate from the donor star fails to sustain a continuous viscous flow to the compact object, the matter accumulates in the outer disk until it reaches a critical surface density, triggering an outburst. This theoretical model was originally formulated for dwarf novae and later expanded to encompass X-ray novae. This model also predicts recurrent outbursts, which have been observed in the past. Outbursts are known to occur on shorter timescales, however, these outbursts cannot be understood in terms of the disk-instability model.

1.2.1 X-ray energy spectra

The X-ray energy spectra of BHBs are composed of two components: soft (thermal) and hard (non-thermal). These components dominate different accretion states during an outburst, namely HSS and LHS respectively. The thermal component can be effectively modelled using a multi-temperature disk black-body, originating from the inner regions of the optically thick, geometrically thin accretion disk, with a characteristic temperature of approximately 1 keV. On the other hand, the non-thermal component is typically represented by a power-law, believed to originate from an optically thin, geometrically thick corona enveloping the black hole. The power-law exhibits a photon index denoted by Γ, with the photon spectrum following the form $N(E) \propto E^{-\Gamma}$. The non-thermal component extends to higher energies and often exhibits an exponential cutoff at high energies.

In certain BHBs, particularly those observed from nearly face-on angles, the spectral model needs to incorporate an additional component known as disk reflection. This phenomenon occurs when the X-ray power-law emission is reflected by the weakly

ionized, cold accretion disk, resulting in a family of fluorescent lines and edges (Ross and A. C. Fabian, 1993; J. García and Kallman, 2010). The reprocessed X-rays from disk reflection provide valuable information about the composition and state of matter in the vicinity of the black hole's strong gravitational field. Notably, the spectrum displays a distinctive emission feature known as the fluorescent Fe K complex, observed at energy levels of 6-7 keV. The reflection component also introduces a prominent bump in the spectrum around 10 to 30 keV, often referred to as the Compton hump. Unlike the fluorescent lines, which are produced by absorption and reprocessing of soft energy photons, the Compton hump is formed through Compton downscattering of high-energy photons (E. Kara, A. C. Fabian, et al., 2015). Figure 3 illustrates a schematic representation of the components present in a typical BHB spectrum. Due to the proximity of the reflection region to the black hole's intense gravitational well, the line profiles are frequently broadened and distorted by relativistic Doppler effects, light bending, and gravitational redshift (A. C. Fabian, Rees, et al., 1989; Dauser, Garcia, et al., 2013).

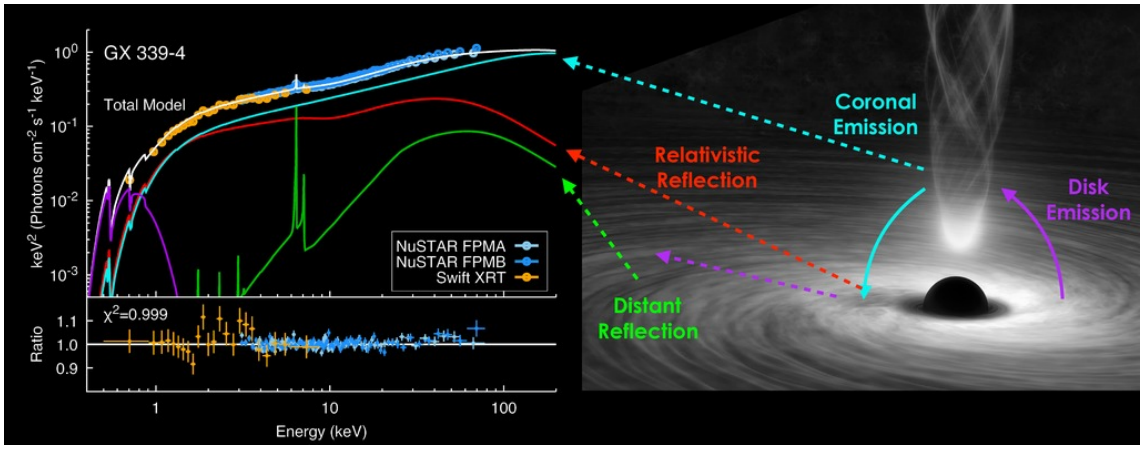

Figure 3: Left: Observed X-ray spectrum of the black hole X-ray binary GX 339-4 during its 2017 outburst, showing different spectral components: Compton continuum (blue), relativistic reflection (red), distant reflection (green), and thermal disk emission (violet). Fit residuals are shown in the lower panel. Right: Schematic representation of the origin of the spectral components in an accreting black hole. The disk's thermal emission (violet) is Compton scattered by electrons in a hot 'corona', resulting in a power-law component (blue). Some of this emission illuminates the disk, giving rise to relativistic reflection (red arrows) and distant reflection (green). (Source: J. A. García, Bachetti, et al., 2019

1.2.2 X-ray timing methods

The rapid fluctuations in X-ray intensity observed near the inner regions of a BH serve as a valuable avenue in understanding the processes occurring close to the black hole (Klis, 2004; McClintock and Remillard, 2006). To investigate these fast variations, a commonly utilized analysis tool is the power-density spectrum (PDS; e.g., Leahy et al., 1983). The PDS offers valuable insights into the continuum power in terms of both its shape and integrated amplitude, often expressed as rms fluctuations scaled to the mean count rate. In the case of BHBs, PDSs exhibit transient and distinct features known as quasi-periodic oscillations (QPOs) that span frequencies ranging from 0.01

to 450 Hz. These QPOs are typically characterized by Lorentzian profiles and can be distinguished from broad power peaks based on a coherence parameter (M. A. Nowak, 2000;Klis, 2004). The coherence parameter, Q, is defined as the ratio of the centroid frequency to the FWHM ($\nu_{\rm peak}/\Delta\nu$) of the QPO.

1.3 Accretion states of black hole binaries during outbursts

1.3.1 A brief history

The concept of X-ray states was first introduced when Tananbaum et al. (1972) discovered a significant change in the spectral properties of the persistent X-ray binary system Cyg X-1, where the soft X-ray flux (2-6 keV) decreased by a factor of 4, while the hard flux (10-20 keV) increased by a factor of 2 and the radio signal became active. This pattern was later observed in other sources, indicating a similar emission mechanism at play in both persistent and transient systems. Over the last decade, a coherent understanding of the properties of most XRB systems has emerged. The time evolution of outbursts in X-ray binaries can vary considerably between different systems and even within the same object during multiple outbursts. However, when plotted on a Hardness-Intensity Diagram (HID), regular patterns can be observed. An HID is similar to a hardness-magnitude diagram in the optical band, where the x-axis represents the ratio of photon counts in two separate bands (hard and soft), indicating the spectral hardness, while the y-axis represents the sum of the count rate over the two bands, acting as a proxy for the luminosity and accretion rate. HIDs are a common tool used to examine the spectral evolution of BHBs.

Figure 4 shows the HID for the XRB GX 339-4, providing an ideal sketch of the typical evolution of an XRB outburst. The overall progression follows a consistent pattern, a 'q'-shaped trajectory moving counterclockwise from the lower right corner where the spectrum is faint and hard. The two primary spectral states can be identified as the two "vertical" branches in the HID plot. The Low-Hard State (LHS) is indicated by the hard branch extending to the stem of the 'q' and is visible only at the beginning and end of an outburst, but not in the middle. Although the logarithmic axis may suggest a perfectly vertical alignment, there is a noticeable softening as the source brightens. On the other hand, the left branch denotes the High-Soft State (HSS). A transition between the LHS and HSS of a source occurs at two distinct levels of flux. When the flux is high, the source switches from LHS to HSS, while at low flux, it returns to the LHS state, forming a hysteresis cycle that completes the transition.

The term "high-soft state" originated from the observation that the source emits ~ 1 keV thermal emission from a multi-temperature accretion disk and is typically seen at higher luminosities in X-rays. The term "low/hard state" was used to describe a state in which the source emits radiation with a typical photon index of $\Gamma \sim 1.7$ and is typically faint. In this state, the disk is either not detected above 2 keV or appears cooler and more distant from the black hole. During the Ginga era, researchers identified an additional X-ray state characterized by the emergence of several Hertz QPOs, a relatively high luminosity greater than 0.1 of the Eddington luminosity, and a spectrum consisting of both a thermal component and a power-law component (Miyamoto and Kitamoto, 1991;Miyamoto, Iga, et al., 1993). The power-law component in this state was steeper ($\Gamma \sim 2.5$) than in the hard state and was eventually named the "very high"

state.

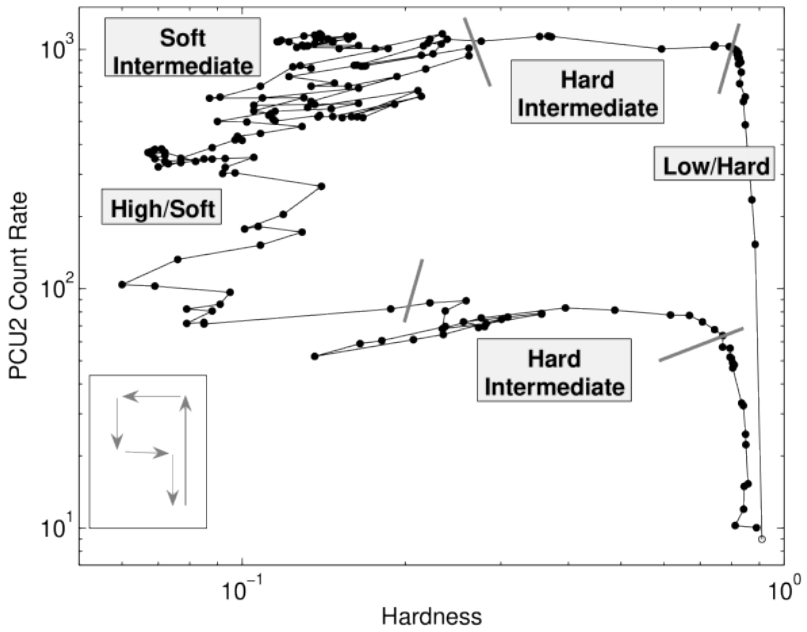

Figure 4: Hardness-intensity diagram of the XRB GX 339-4 observed by the RXTE PCA during the 2002/2003 outburst period. The state transitions are marked by grey lines. The 'q'-shaped pattern's overall time evolution during the outburst is illustrated in the inset located at the lower right corner. (Source: (T. Belloni et al., 2005))

In the era of the RXTE, new observations challenged the previous understanding of X-ray states in BH binaries. For instance, the soft state of Cyg X-1 was found to be dominated by a steep power-law component instead of a thermal component (Zhang, W. Cui, et al., 1997). BHBs near maximum luminosity were also found to exhibit a steep power-law spectrum (McClintock and Remillard, 2006), and different types of QPOs were commonly observed across a wide range of luminosities (e.g., Morgan et al., 1997; Sobczak et al., 2000; Homan et al., 2001). These discoveries prompted a great interest in understanding the nature of the very high state in BHBs. Concurrently, gamma-ray observations of seven BHBs revealed significant differences between the low/hard state and the very high state (Grove et al. (1998) and Tomsick et al. (1999)). Sources in the LHS exhibited an exponential cutoff near 100 keV, while sources in the VH state maintained a steep, strong, and unbroken power-law component out to the limit of gamma-ray detectors at around 1 keV.

Historically, the study of BHB accretion states has relied exclusively on X-ray spectral and timing studies. In recent times, collaborations between X-ray, radio, optical, and gamma-ray observers have led to a more comprehensive and productive framework for understanding emission states more physically. Radio observations have strengthened the link between the low/hard state in black hole binaries and the presence of a compact and quasi-steady radio jet. The observational evidence that supports this association, outlined by McClintock and Remillard (2006), includes the presence of compact jets in Very Long Baseline Interferometry (VLBI) images of two BH sources

(Dhawan et al., 2000; Stirling et al., 2001), correlated X-ray and radio intensities and/or flat or inverted radio spectra (e.g.,Gallo et al., 2003), an observed 2% linear radio polarization at an almost constant position angle in the XRB GX 339-4 (Corbel et al., 2000), and the frequent quenching of persistent radio emission when a BHB transitions from the LHS to the HSS (e.g. Robert Fender et al., 1999).

1.3.2 A three-state model for outbursts

McClintock and Remillard (2006) proposed a new approach for defining X-ray states in BHBs that moves beyond a purely phenomenological description and abandons luminosity as a defining criterion (except the quiescent state). They based their framework on prior discoveries and extensive data from the RXTE archive, and the new set of names for the spectral states is motivated by the emergent physical properties of each state and multiwavelength results. However, the authors still attempted to define the states primarily based on X-ray data, using PDSs and a practical approach of fitting a spectral model consisting of a multi-temperature accretion disk and a power-law component (with a potential break near 15 keV or an exponential cutoff in the 30-100 keV range). This model also incorporated features such as photoelectric absorption by neutral hydrogen, and an inclusion of an iron emission line or a reflection component when needed. The characteristics of each state are illustrated in Figure 6, which shows examples of PDSs and energy spectra for GRO J1655-40.
Four parameters were used to define the X-ray states, namely:

1. Disk fraction (f): It represents the proportion of the disk flux (emission from a disk) to the total flux (all emission, excluding absorption) at energy levels between 2 and 20 keV. This parameter helps assess the relative contribution of the disk to the overall emission.

2. power-law photon index (Γ): This parameter measures the spectral shape of the emission at energies lower than any spectral break or cutoff. It provides information about the energy distribution of photons. A lower Γ value indicates a steeper spectrum, while a higher value indicates a flatter spectrum.

3. RMS power (r) in the PDS: The power density spectrum (PDS) is a way to analyze the distribution of power as a function of frequency in a time series. The RMS power parameter quantifies the integrated power in the PDS over a frequency range of 0.1 to 10 Hz . It is expressed as a fraction of the average count rate of the source. This parameter helps understand the variability or fluctuations in the source's emission.

4. Integrated RMS amplitude (a) of the QPO: The integrated RMS amplitude parameter measures the strength of any detected QPO signal in the frequency range, usually in the range of 0.1 to 30 Hz. It provides information about the amplitude or magnitude of the periodic variations.

   Notably, the PDS criteria mentioned in (3) and (4) utilize a wide energy range, typically the bandwidth of the RXTE PCA instrument, which covers the energy range of 2 to 30 keV.

The subsequent sections describe the accretion states based on the aforementioned criteria outlined by McClintock and Remillard (2006). Additionally, some of the physical models that have been proposed to explain each of these states are discussed.

Thermal state

In the thermal state, previously known as the high/soft state, the dominant source of flux is the thermal radiation emitted from the inner disk region. This state is characterized by a faint integrated power continuum and usually lacks strong or noticeable QPO. Although there is still a non-thermal component present, it contributes to less than 25% of the total flux in the energy range of 2-20 keV. The middle row of Fig. 6 illustrates this state. The spectrum deconvolution analysis reveals that the thermal component (represented by the red line) is responsible for the majority of the flux below 10 keV, in contrast to the power-law component (represented by the blue line). On the right panel of the Figure, the power density spectrum (PDS) plot demonstrates a featureless behaviour. Similar patterns have been observed in other BHBs.

The steady-state, thin accretion disk model is a well-known hydrodynamic model used to describe a radiating gas orbiting around a compact object under the influence of gravitational potential (Shakura and Sunyaev, 1973; Pringle, 1981). A significant challenge in this model is determining the appropriate viscosity that facilitates the inward motion of matter, its heating, and the outward transport of angular momentum. Initially, an ad hoc scaling assumption was employed to model the viscosity (Shakura and Sunyaev, 1973). This particular model predicts a temperature profile, T(R), that follows a power-law relationship with the radius given by

$$T(R) \propto R^{-3/4}$$

Consequently, it suggests that the inner annulus within the disk dominates the thermal spectrum, as the luminosity (L(R)) is proportional to R^{-2}, resulting in

$$\pi R dR \sigma T^4 \propto L(R) \propto R^{-2}$$

This result holds significant implications for X-ray astronomy, suggesting that X-ray observations are ideal for exploring the intense gravitational forces around accreting stellar-mass black holes.

The significance of the inner disk region underscores the necessity for a precise model to understand the radiation emitted near the ISCO. In the case of a Schwarzschild black hole (with a = 0), the ISCO is situated at 6 times the gravitational radius (R_g). However, as the spin parameter approaches 1, the ISCO shifts closer to 1 R_g. The observed thermal-state spectra of BHBs can be effectively characterized by the conventional model of a multi-temperature accretion disk (Mitsuda et al., 1984; Makishima et al., 1986; Kubota and Makishima, 2004, Kubota, Ebisawa, et al., 2005), available in XSPEC as '`diskbb`'.

Caution is warranted when interpreting the spectral parameters of the '`diskbb`' model, such as the temperature and radius of the inner disk. The classical model overlooks the torque-free boundary condition at the ISCO (Gierliński et al., 2001;

Zimmerman et al., 2005). Additionally, the classical model fails to account for significant effects arising from general relativity and radiative transfer (Zhang, Wei Cui, et al., 1997). Nevertheless, more advancements have been made in developing accretion disk models for Kerr black holes (Li et al., 2005; Dovčiak et al., 2004). Furthermore, there exists a fully relativistic approach that considers the effects of spectral hardening, as demonstrated by Davis et al. (2005).

Advancements in magnetohydrodynamic (MHD) simulations have significantly contributed to the understanding of viscosity in accretion disks. These simulations have demonstrated that the magnetorotational instability (MRI) serves as a source of turbulent viscosity (Balbus and Hawley, 1991). The validity of this finding has been further supported by various global general relativity MHD simulations (e.g. De Villiers et al., 2003, McKinney and Gammie, 2004 and Matsumoto et al., 2004). Researchers have been exploring the influence of MRI and MHD turbulence on different aspects of accretion disk dynamics, including investigating its impact on disk structure, the formation of thermal spectra, and the effects of Compton scattering (Gammie, 2004; Merloni, 2003; Socrates et al., 2004).

Hard state

The hard state, previously referred to as the low/hard state, is defined by a prominent hard power-law component with a photon index (Γ) of approximately 1.4-2.1, which typically accounts for more than 80% of the total X-ray flux in the 2–20 keV energy range. In this state, the power-law continuum emission is notably luminous, characterized by RMS power (r) exceeding 0.1, and the presence or absence of QPOs is observed. In Fig. 6, the lower row of panels depicts a representative observation of GRO J1655–40 in the hard state. Notably, in this state, the accretion disk tends to exhibit lower luminosity and a relatively cooler temperature compared to the thermal state. As highlighted earlier, the hard state is closely associated with the emergence of a quasi-steady radio jet. Furthermore, discernible correlations between the intensities of radio emissions and X-ray emissions have been consistently observed in this state.

Earlier models of BHB spectra in the quiescent state suggest that the blackbody radiation of the accretion disk is truncated at some radius larger than the ISCO (Narayan, 1996; Narayan, McClintock, et al., 1996). The physical state of material within this large-radius, truncated blackbody radiation zone remains uncertain. A possible scenario is a thermal advection-dominated accretion flow model (ADAF; Narayan and Yi, 1994; Narayan, McClintock, et al., 1996; Ann A. Esin et al., 2001), where the truncated region is filled with a hot radiatively inefficient accretion flow. In this regime, most of the energy released via viscous dissipation is advected with the flow instead of being radiated away. An illustration of the ADAF model is depicted in Figure 7 across various accretion states (see section 1.3.3 for more details).

Alternative models include static corona with various configurations (illustrated in Figure 5) including a slab-like geometry that 'sandwiches' the disk (e.g. Haardt and Maraschi, 1993), or a 'lamp-post' configuration wherein a compact magnetized region resides above the disk, with possible velocity component directed away from the compact object (e.g. Matt et al., 1992; Merloni and A. C. Fabian, 2002). The lamp-post model has been physically interpreted as the base of the relativistic jet (e.g. Markoff

and M. Nowak, 2004; Markoff, M. Nowak, and Jörn Wilms, 2005; Maitra et al., 2009; Dauser, Garcia, et al., 2013). Alternatively, the jet may be supplied by hot gas from a surrounding ADAF flow (Yuan et al., 2005).

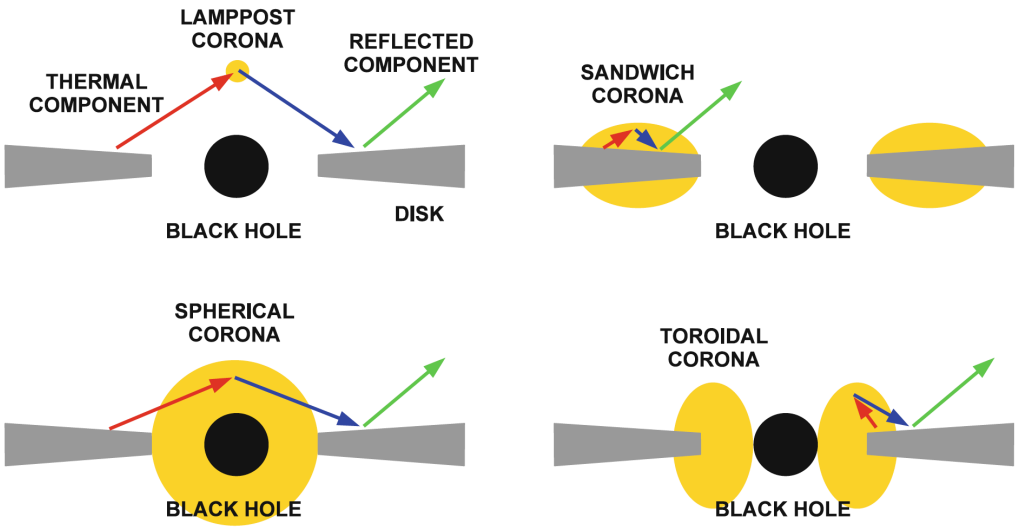

Figure 5: Coronal Geometries: (Top left) Base of the jet illustrated as a 'lamp-post corona.' Top right: depiction of the hot atmosphere above the accretion disk, known as a 'sandwich corona.' (Bottom left and bottom right) Spherical and toroidal coronae (respectively) are situated in the plunging region between the inner edge of the accretion disk and the black hole. (Source: Bambi et al. (2023))

Steep power-law state

The Steep power-law state, previously known as the very high state, is defined by a robust power-law component with a photon index $\Gamma \sim 2.5$. This state often exhibits an unbroken power-law extending to energies around 1 MeV or higher. It is characterized by the presence of a substantial thermal component and frequent QPOs. An example of the SPL state is shown in the top panels of Fig. 6. While similarities exist between the SPL and thermal states, including both having a thermal component and a power-law component, the SPL state is notably distinguished by its powerful power-law component and the frequent occurrence of QPOs. The SPL state typically dominates BHB spectra as luminosity approaches the Eddington limit and is associated with high-frequency QPOs (McClintock and Remillard, 2006).

The origin of the SPL state remains a major challenge in high-energy astrophysics. Understanding this state is crucial due to its ability to produce HFQPOs, exceptionally high luminosity, and spectra extending beyond 1 MeV. Many SPL state models propose that inverse Compton scattering is the primary radiation mechanism (Andrzej A. Zdziarski and Gierliński, 2004). The presence of MeV photons suggests that this scattering takes place in a non-thermal corona, often depicted as a simple slab interacting with photons from the underlying disk (Andrzej A. Zdziarski, Gierlinski, et al., 2005).

Efforts to identify the origin of Comptonizing electrons have given rise to more intri-

cate models featuring feedback mechanisms. For instance, some models propose flare regions triggered by magnetic instabilities within the accretion disk (Poutanen and Andrew C. Fabian, 1999). Alternative models, such as bulk motion Comptonization, have been suggested in the context of a converging sub-Keplerian flow within 50 R_g of the black hole (Titarchuk and Shrader, 2002; Turolla et al., 2002). An examination of extensive RXTE spectral observations of GRO J1655–40 and XTE J1550–564 indicates that as the power-law component strengthens and steepens, the disk's luminosity and radius tend to decrease while the temperature remains high. These findings lend support to the notion of substantial Comptonization of disk photons in SPL state, originally proposed by Kubota and Makishima (2004).

Intermediate states

Intermediate states and state transitions are vital components of BHB research. McClintock and Remillard (2006) introduced three distinct states to describe quasi-stable conditions in BHBs with specific spectral and timing characteristics. However, these states leave gaps in parameter ranges, leading to the emergence of intermediate states. Of particular interest is the hybrid state that combines features of both the hard state and the SPL state. This state exhibits intriguing correlations with radio properties as well as characteristics of the accretion disk.

The Hard Intermediate State (HIMS) represents a transitional phase in the evolution of BHBs. It occurs between the thermal state and the hard state and can appear after the initial hard state phase and before the source returns to the hard state at the end of an outburst. In HIMS, the softening compared to the hard state is influenced by two factors: the emergence of thermal disc flux in the observational range and the steepening of the hard component. This state exhibits fast variability, characterized by increasing characteristic frequencies and decreasing total fractional rms. Additionally, Type-C QPOs are observed (§1.4).

The Soft Intermediate State (SIMS) features a slightly softer energy spectrum compared to HIMS. Although not immediately distinguishable in the HID and the RMS-Intensity Diagram (RID), SIMS can be identified in the Hardness-RMS Diagram (HRD). Key characteristics of SIMS include the absence of a significant high-energy cutoff in its spectrum, unlike HIMS. Notably, SIMS is marked by the disappearance of band-limited noise components in the power density spectrum, replaced by a weaker power-law component, and the presence of type-B QPOs (§1.4).

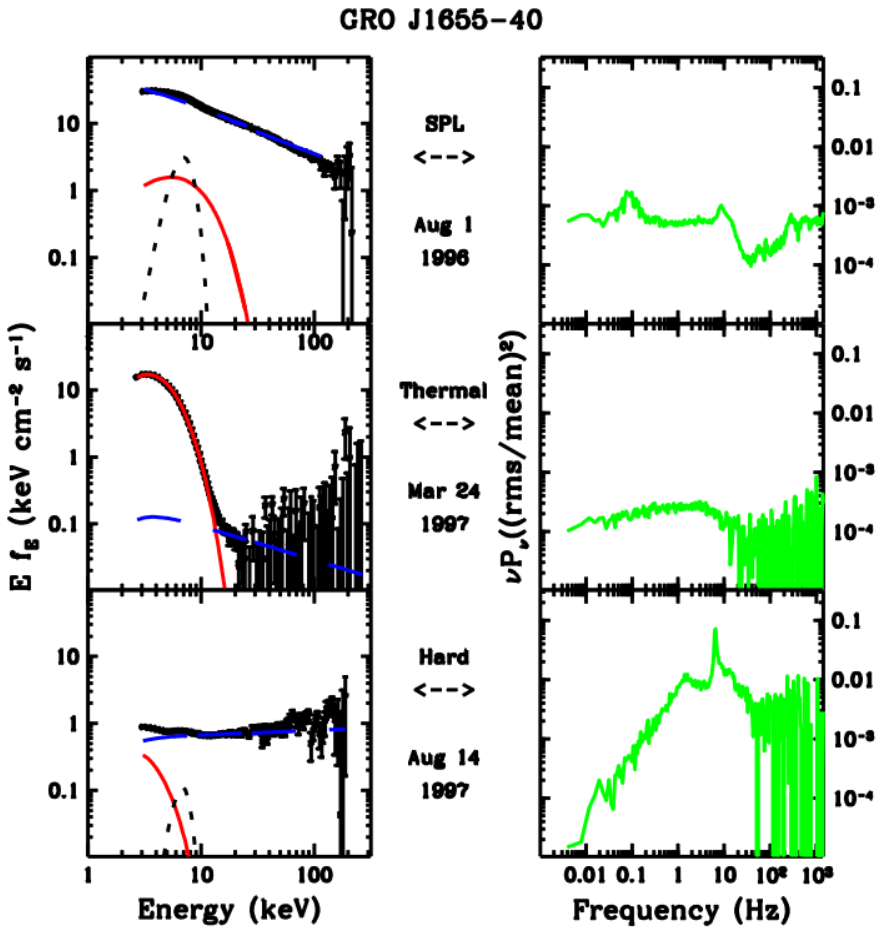

Figure 6: Sample spectra of the black hole binary GRO J1655-40 demonstrating the three outburst states: steep power law, thermal, and hard. Each state is represented by a pair of panels. The left panels show the spectral energy distribution separated into three components: thermal (red, solid line), power-law (blue, dashed line), and a broadened Fe Kα line (black, dotted line) with relativistic effects. The right panels illustrate the PDS plotted as $\log(\nu \times P_\nu)$ versus $\log \nu$ (source: Remillard and McClintock, 2006).

1.3.3 Unifying the accretion states

A notable endeavour in the domain of BHB accretion states aimed to consolidate the accretion states of a BHB, employing both the Multi-temperature accretion disk and ADAF models (Esin, McClintock, et al., 1997). The conceptualization of this approach is visually depicted in Figures 7 and 8, illustrating the dynamic alterations in the accretion flow's geometry as the mass accretion rate ($\dot{m}$) varies, with $\dot{m}$ represented in Eddington units.

This model describes the progression of a BHB system through five discernible states, each marked by an increment in the mass accretion rate in Fig. 7, ranging from the quiescent state to the Steep power law state, previously known as the very high state. In the three states characterized by lower values of $\dot{m}$ in Fig. 7, the accretion flow is demarcated into two zones, specifically the accretion disk and the ADAF, as explained

previously. Conversely, in the two states with the highest values of $\dot{m}$, the accretion disk extends down to the ISCO. As depicted in Fig. 8, both the low/hard state and quiescent state exhibit magnetic field lines, with the low/hard state additionally featuring prominent jet outflows. Notably, in all five states, the accretion disk is enshrouded by a corona that seamlessly extends from the ADAF. The model maintains a comprehensive approach by consistently addressing the dynamics of the accreting gas, the thermal equilibrium of ions and electrons within the ADAF and corona, as well as the radiation processes. Its efficacy is underscored by its ability to successfully describe the spectral evolution of several BHBs (Esin, McClintock, et al., 1997; Esin, Narayan, et al., 1998).

It is important to acknowledge that the multi-state model does have certain limitations. Firstly, it does not encompass the SPL state. Additionally, the simplistic ordering of states based solely on mass accretion rate or luminosity represents a rudimentary classification. The model also falls short in providing a comprehensive account of the dynamic behaviour exhibited by the corona, including intense flares and potent low-frequency quasi-periodic oscillations. Moreover, it does not consider the radio emission detected in the majority of BHBs. Furthermore, the "evaporation" mechanism, which describes the transition of cold gas from a thin disk to a hot ADAF is only understood qualitatively.

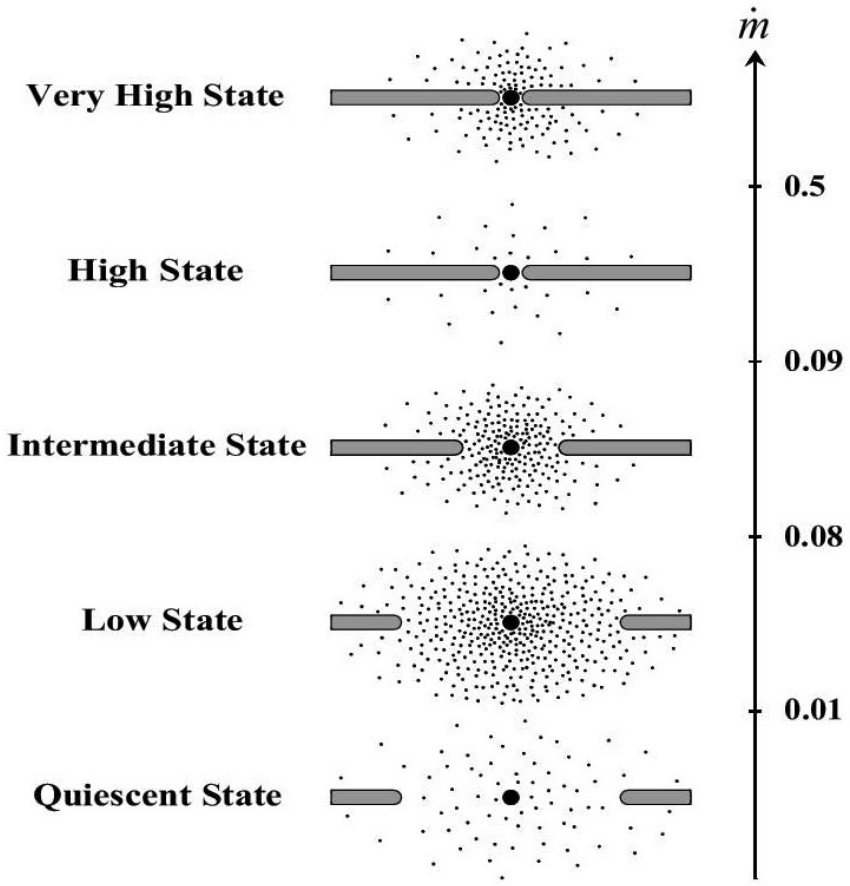

Figure 7: This schematic diagram depicts the accretion flow in various spectral states as a function of the total Eddington-scaled mass accretion rate ($\dot{m}$). The Figure uses dots to represent the ADAF and horizontal bars to denote the thin accretion disk. It includes the SPL/VHS for illustrative purposes, although it is not incorporated into the unification scheme described by Esin, McClintock, et al. (1997).

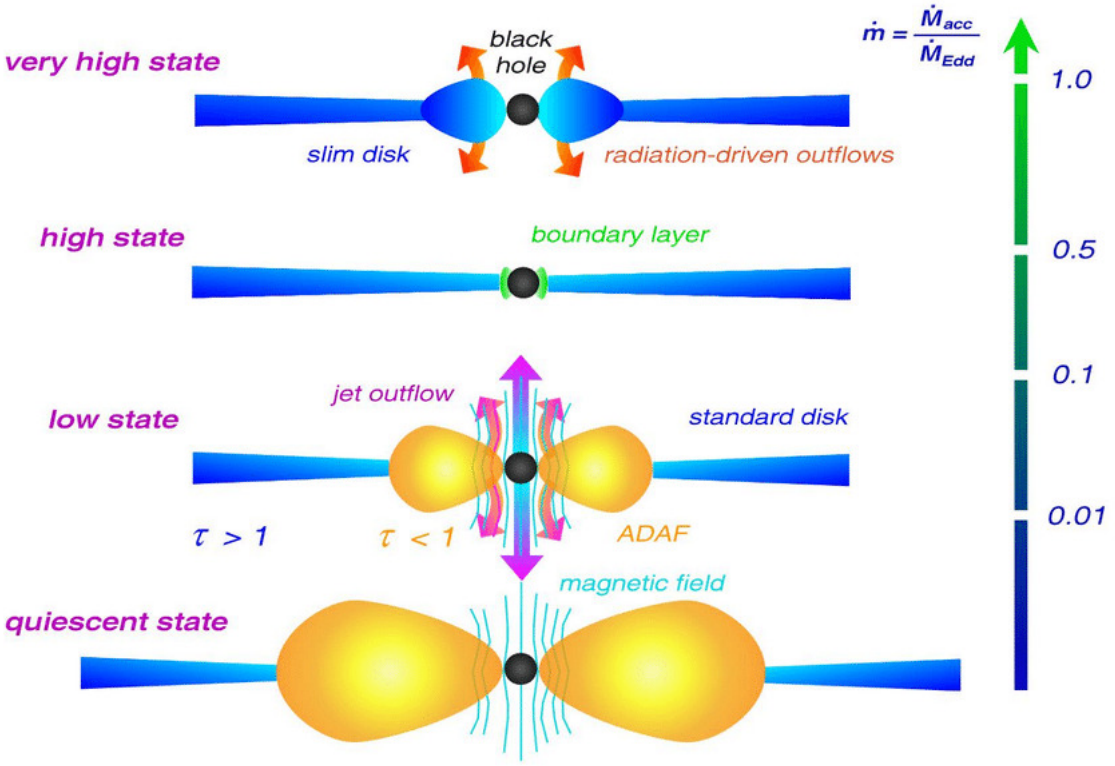

Figure 8: This schematic diagram depicts a more detailed version of the Esin, McClintock, et al., 1997 unified accretion state model, excluding the intermediate state and incorporating magnetic fields and jet outflows (Müller, Ph. D thesis, 2004).

1.3.4 The Unified Model for X-ray States and Radio Jets

In the realm of BHBs, HIDs provide a model-independent approach for monitoring the behaviour of XRBs. However, relating results to physical quantities can be challenging. Figure 9 presents a schematic depicting the relationships between the disk, jets and X-ray states. The HID illustrates the "Unified Model for Radio Jets" proposed by R. P. Fender et al. (2004). Observations distinguish the state of an X-ray source based on the HR value. The Figure shows how the jet's Lorentz factor and morphology evolve with changes in the X-ray state. Tracks for state transitions in the HID are also provided. The solid vertical "jet line" separates the X-ray spectrum's hard region on the right, indicative of a steady radio jet, from the soft spectrum region on the left where the jet is suppressed.

The trajectory for state evolution in the HID was influenced by observations of GX 339–4 (Tomaso Belloni, 2005). Different HR values define distinct states, such as the low/hard or hard state (HR $>$ 0.8) and the high/soft or thermal state (HR $<$ 0.2). Intermediate HR values lead to classifications such as the soft intermediate and hard intermediate states, expanding the unified jet model's state definitions. While the HID format is suitable for studying disk-jet coupling and is easy to apply to observations, McClintock and Remillard (2006) provides more quantitative state definitions, offering spectral information directly applicable to physical models.

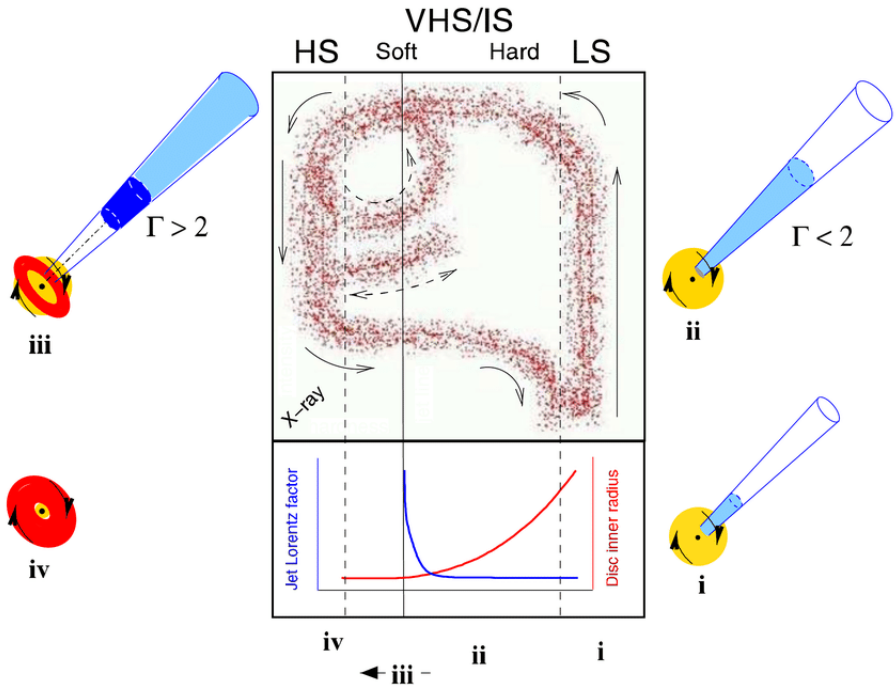

Figure 9: A schematic illustration of the model depicting disk-jet coupling in black hole binaries, as presented by R. P. Fender et al., 2004. The upper panel displays evolutionary trajectories within an HID, where X-ray intensity increases upward, and X-ray hardness increases to the right. In the lower panel, we observe a qualitative depiction of how the jet's bulk Lorentz factor (represented by the blue curve) and the inner disk radius (indicated by the red curve) vary with respect to X-ray hardness. The X-ray states are identified at the top using the conventional terminology, where HS stands for high/soft state, VHS/IS denotes very high and intermediate states, and LS represents the low/hard state."

1.4 X-ray Quasi-periodic Oscillations

The fast time variability is a significant feature of BHBs and is crucial in understanding the underlying physical processes within these systems. Researchers commonly examine PDS to analyse this variability, which provides insights into the aperiodic and quasiperiodic fluctuations. In the PDS of BHBs, most of the power spectral components are broad, spanning several frequency decades, or they can manifest as localized peaks known as Quasi-Periodic Oscillations (QPOs). QPOs were initially observed in the X-ray emissions from accreting neutron stars and have subsequently been detected in numerous BHB systems. These QPOs are now recognized as a common characteristic of both accreting black holes and neutron star binaries, as well as in cataclysmic variables, ultra-luminous X-ray sources, and even AGN. The regular occurrence of QPOs across various astrophysical objects suggests their relevance in understanding the dynamics of accretion processes and the properties of compact objects.

1.4.1 Low-frequency QPOs

Low-frequency Quasi-Periodic Oscillations (LFQPOs), characterized by frequencies spanning from a few mHz to $\sim$ 30 Hz, constitute a ubiquitous phenomenon in nearly all

transient BHBs. Early investigations, such as those employing the Ginga satellite, have categorized LFQPOs into distinct classes, as exemplified by GX 339-4 and GS 1124-68 (Miyamoto and Kitamoto, 1991). The advent of the Rossi X-ray Timing Explorer (RXTE) heralded a significant advancement in our understanding of variability within BHBs. It is noteworthy that the detection of LFQPOs in the majority of observed BHBs became feasible only after the launch of RXTE.

LFQPOs are classified into three main types: A, B, and C, initially discovered in the PDS of the black hole binary XTE J1550-564 (Wijnands, Homan, et al., 1999;Homan et al., 2001;Remillard, Muno, et al., 2002). These LFQPO types have been observed in various other sources as well. Examples of the different types of QPOs observed in GX 339-4 observations are illustrated in Figure 10. The classification of QPOs is primarily based on their inherent characteristics, such as the centroid frequency and Full Width at Half Maximum (FWHM). This distinction is further quantified using the coherence parameter (Q). Additionally, factors like energy dependence, phase lags, properties of the underlying broad-band noise components (including noise shape and total variability level), and the relationships among these quantities are also considered for identification and classification. By taking into account these diverse factors, researchers gain a comprehensive understanding of the QPO properties, enabling a more robust and meaningful categorization of the observed LFQPOs.

Type-A QPOs are characterized by a weak signal with a broad peak around 6-8 Hz. Typically, neither a subharmonic nor a second harmonic is observed, possibly due to the width of the fundamental peak. Additionally, Type-A QPOs exhibit very low-amplitude red noise and are predominantly observed in the thermal state, shortly after transitioning from the HIMS. Type-B QPOs are relatively strong (approximately 4% rms) and have a narrow peak, with frequencies typically around 6 Hz or 1-3 Hz, as described in S. Motta, Muñ oz-Darias, et al., 2011. They are a key characteristic of the SIMS and may display weak red noise at low frequencies and are often accompanied by a weak second harmonic or a subharmonic peak. Rapid transitions in which Type-B LFQPOs appear or disappear, often within a few seconds, are common in some sources (Nespoli et al., 2003).

Type-C QPOs exhibit a strong signal, with rms variability of up to 20%, and a narrow peak. Their centroid frequency and intensity can vary significantly over a few days (S. E. Motta, Casella, et al., 2015). These QPOs are observed in the frequency range of 0.1-15 Hz and are superimposed onto a flat-top noise, which steepens at frequencies higher than the QPO frequency. Type-C QPOs often show subharmonic and second harmonic peaks and occasionally a third harmonic. The total fractional rms variability can reach as high as 40%. The frequency of Type-C QPOs correlates with the flat-top noise break-frequency, as noted in Wijnands and Klis (1999), and with the characteristic frequency of some broad components seen in the PDS at higher frequencies (Psaltis et al., 1999). Type-C QPOs are typically observed during the bright end of the hard state and the HIMS. They are also observed in the thermal state of some sources, where their frequencies can reach around 30 Hz (e.g. S. Motta, Homan, et al., 2012; S. E. Motta, Casella, et al., 2015).

1.4.2 Physical mechanisms behind LFQPOs

While LFQPOs have been a subject of study for several decades, their origin remains enigmatic, and a consensus regarding their physical nature has yet to be reached. Nonetheless, the investigation of LFQPOs offers an indirect avenue for probing the dynamics of accretion flows around both black holes and neutron stars. Existing models designed to explain the origins of LFQPOs predominantly fall into two categories: those rooted in instabilities and those driven by geometrical effects. In the latter case, the phenomenon of precession plays a central role.

One notable model, introduced by Titarchuk and Fiorito (2004), is the transition layer model. According to this framework, type-C QPOs result from viscous magneto-acoustic oscillations within a spherical transition layer formed by matter from the accretion disc. This layer adjusts to sub-Keplerian boundary conditions in proximity to the central compact object. Another model, proposed by Cabanac et al. (2010), explains both type-C QPOs and the associated broad-band noise. It postulates that magneto-acoustic waves within the corona induce oscillations, modulating the efficiency of the Comptonization process on embedded photons. This modulation gives rise to both type-C QPOs, through a resonance effect, and the accompanying noise.

The relativistic precession model (RPM) seeks to explain the origin and behaviour of a specific type of LFQPO, the horizontal-branch oscillation, as well as two high-frequency QPOs (kHz QPOs) in neutron star X-ray binaries (Stella and Vietri, 1998). It posits that these phenomena arise from nodal precession, periastron precession, and Keplerian motion of a self-luminous material blob within the accretion flow around the compact object. Subsequently, this model is extended to black holes by Stella, Vietri, and Morsink (1999) and S. E. Motta, Muñ oz-Darias, et al. (2014), who demonstrate its applicability to type-C QPOs and high-frequency QPOs in at least two black hole systems.

A different perspective is offered by Ingram, Done, and Fragile (2009), who proposes a model based on relativistic precession as predicted by the theory of General Relativity. This model aims to explain type-C QPOs and their associated noise. It requires a geometrically thin, optically thick accretion disc that is truncated at some radius greater than the ISCO and filled with a hot, geometrically thick accretion flow as in the truncated disk model previously discussed. In this framework, type-C QPOs are attributed to the Lense-Thirring precession of a radially extended section of the hot inner flow, modulating X-ray flux through a combination of self-occultation, projected area changes, and relativistic effects that intensify with inclination. The broad-band noise linked to type-C QPOs is posited to arise from variations in mass accretion rate from the outer regions of the accretion flow, propagating toward the central compact object and modulating the inner region's variations, resulting in inclination-independent radiation changes.

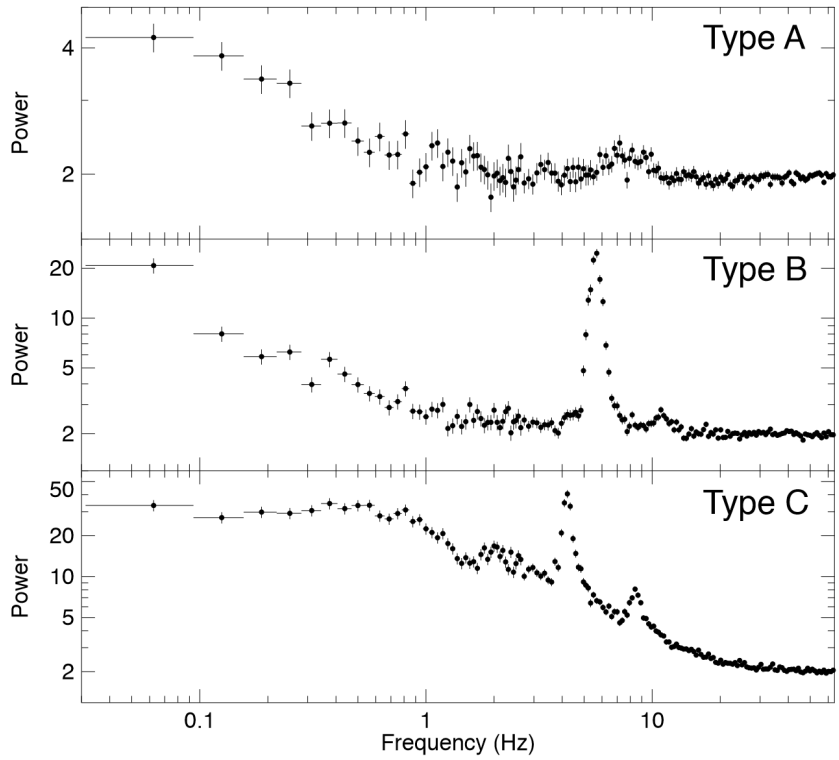

Figure 10: Examples of type A, B and C QPOs from GX 339-4 observations (S. Motta, Muñ oz-Darias, et al., 2011)

1.5 Open questions

Our knowledge and understanding of black hole objects have had a significant increase over the past two decades, owing to the availability of high-quality data from past and current high-energy missions. The advancements in observations at other wavelengths, from radio to gamma rays, have allowed us to study various phenomena surrounding black hole objects previously ignored, such as relativistic jets and outflows. Multi-wavelength studies have become imperative in properly understanding and characterising the physical properties of these objects.

There are still many outstanding questions surrounding black hole objects. These questions include, but are not limited to:

- **Origin of the Corona:** What is the precise geometry, location, and origin of the corona in BHXBs? Despite extensive research, the illuminating source remains poorly understood. The hypothesis of photons emanating from a hot corona undergoing Comptonization, potentially linked to the base of a jet, needs further investigation.
- **Relativistic Jet Launching Mechanism:** How do relativistic jets get launched in BHXBs, and what role do magnetic fields play in their formation? Magnetic fields are believed to be crucial in the accretion process, extracting rotational energy from the black hole. However, the detailed mechanisms of jet formation and the specific involvement of magnetic fields remain incompletely understood.

- **Ubiquity of Relativistic Jets in the Hard State:** Why are relativistic jets consistently observed in the hard state of BHXBs, while being quenched in the soft state, where non-relativistic wind-like outflows are prevalent? Understanding the conditions and transitions between these states is vital for unravelling the dynamics of accretion processes in BHXBs.

- **Origin of Quasi-Periodic Oscillations (QPOs):** What is the origin of Quasi-Periodic Oscillations (QPOs) in X-ray binaries, and how are they related to the accretion process? Despite their widespread occurrence, the underlying physical mechanisms of QPOs are not well understood. Theories range from accretion disk instabilities to oscillations within the corona, necessitating further exploration.

- **Connection Between X-ray Binaries and AGN:** What is the relationship between X-ray binaries and AGN? While AGNs are powered by accretion onto supermassive black holes and X-ray binaries are fueled by accretion onto stellar-mass black holes or neutron stars, some AGNs exhibit properties akin to X-ray binaries. Understanding this connection, particularly regarding rapid variability and outflows, can provide insights into the broader mechanisms of accretion in the universe.

1.6 Motivation

Over the past two decades, X-ray spectroscopy and timing techniques have emerged as potent probes for analyzing the evolution of AGN and black hole X-ray binaries. The study of BHB through X-ray spectra and timing is motivated by the unique and dynamic astrophysical phenomena exhibited by these systems, offering a window into the fundamental processes governing their behaviour. X-ray observations provide a direct means to probe the high-energy emission associated with accretion onto black holes, allowing for the characterization of the accretion disk, corona, and other components. Spectral analysis enables the ability to discern key properties such as the temperature and ionization state of the emitting material, shedding light on the physical conditions near the black hole. Concurrently, timing studies offer insights into the temporal variability of X-ray emission, unveiling phenomena QPOs and variability patterns that encode information about the accretion flow and the geometry of the emitting regions. This dual approach of spectral and timing analysis is instrumental in unravelling the complex interplay between gravitational forces, accretion processes, and relativistic effects in black hole binaries, contributing to a comprehensive understanding of the physics governing these enigmatic cosmic entities.

1.7 Objectives

Our primary objective is to better understand the X-ray spectral evolution of BHBs throughout their outburst. To achieve this goal, we need to gain an understanding of the emission components that dominate the system, including the disk, jet and coronal emission, and the reflected emission of the corona by the disk. Since both the jet and corona of an X-ray binary emit non-thermal X-rays, we can establish a link between the two components by modelling the non-thermal emission under various accretion

states. Moreover, through the implementation of timing analysis, particularly in characterizing QPOs and monitoring the evolution of reverberation lag, our objective is to deepen our understanding of the geometry and characteristics of the emitting region responsible for the variability, which is believed to be associated with the corona. Additionally, we aim to test whether a single spectral model can accurately describe the system throughout the outburst, and if not, identify where the model fails.

In pursuit of our objectives, we leverage the combined strengths of four key observatories: *XMM*-Newton, *Nu*STAR, *Swift*-XRT, and *NICER*. Each observatory brings unique capabilities that collectively contribute to a comprehensive and multifaceted analysis, revealing the intricate nature of the astronomical phenomenon under investigation. *XMM*-Newton distinguishes itself through exceptional sensitivity across a broad energy spectrum, serving as a linchpin for spectral analysis. Its proficiency in capturing softer X-rays enables the discernment of subtle details, significantly enhancing our understanding of the spectral characteristics of BHBs.

*Nu*STAR specializes in higher energy X-rays, providing a distinctive perspective that allows exploration of specific regions of interest often obscured in other observations. Its contributions not only enhance our spectral insights but also significantly complement timing studies. *Swift*-XRT assumes a pivotal role as an additional soft X-ray telescope source, supplementing the observations gathered by XMM-Newton. While XMM-Newton excels in capturing softer X-rays, *Swift*-XRT significantly contributes by providing an additional perspective on the softer energies.

Furthermore, the inclusion of *NICER* for timing analysis adds another dimension to our investigation. Its precision in timing studies illuminates the dynamic behaviour and intricate timing characteristics of BHBs. The collaboration between *NICER* and *Nu*STAR amplifies our exploration, especially in the context of timing studies. The amalgamation of these observatories presents an unparalleled opportunity for conducting a holistic analysis. Leveraging their distinct strengths, we aim to delve into both spectral and timing intricacies, unravelling the complexities inherent in compact binaries.

1.8 MAXI J1820+070

MAXI J1820+070 stands out as one of the brightest transient X-ray sources ever recorded, discovered during a remarkable outburst. The optical counterpart, ASASSN-18ey, was initially identified by the All Sky Automated Search for Supernovae on March 3, 2018, followed by the discovery of the X-ray source on March 11, 2018, through the Monitor of All-Sky Image (MAXI), establishing their correlation (Kawamuro et al., 2018; Denisenko, 2018). Subsequent investigations confirmed MAXI J1820+070 as an outbursting black hole LMXRB (Baglio et al., 2018). The system comprises a black hole with a mass of $8.48^{+0.79}_{-0.72} M_{\odot}$ and a K3-K5 donor star of mass $M_2 = 0.61^{+0.13}_{-0.12} M_{\odot}$ (Torres, J. Casares, Jiménez-Ibarra, Álvarez-Hernández, et al., 2020), categorizing it as an LMXRB. With a radio parallax measurement establishing a distance of 2.96 ± 0.33 kpc (Atri et al., 2020), MAXI J1820+070 provides a compelling celestial laboratory for studying black hole binaries.

In recent years, MAXI J1820+070 has garnered considerable attention and has been the focal point of an extensive multi-wavelength campaign. Its extreme brightness and low absorbing column density ($N_{\rm H} \sim 10^{21}$ cm$^{-2/}$, Uttley et al., 2018) make it an exceptional target for detailed investigations into the outbursts and state transitions of black hole X-ray binaries (BHXRBs). Comprehensive radio observations, coupled with high spatial resolution Chandra observations, unveiled the ejection of long-lived discrete relativistic jets (Bright et al., 2020; Bright et al., 2020). Additionally, timing studies on MAXI J1820+070 have uncovered evolving QPOs (e.g, Buisson et al., 2019) and hard-vs-soft emission time lags (e.g, E. Kara, J. F. Steiner, et al., 2019; Wang, Mastroserio, et al., 2021), providing crucial insights into the dynamics of the accretion disk and corona.

The results of the work by Buisson et al. (2019) challenge inner disk precession models (e.g., Lense-Thirring precession) as the origin of QPOs, instead suggesting a temporal development of the corona. These findings are supported by observed changes in QPO frequency without significant disk truncation. Buisson et al. (2019) propose the use of two-point sources along the spin axis within the lamp-post model to differentiate between the illumination of the outer and inner disk. The necessity for a double lamp-post model is further substantiated by the work of Lucchini et al. (2023), which demonstrates that this model provides a better description of both the spectral and timing properties of MAXI J1820+070.

However, recent work by Gao et al. (2023) refutes the hypothesis that oscillations in the corona cause LFQPOs. Their findings suggest that a hot inner flow undergoing Lense-Thirring precession is responsible, a conclusion supported by changes in the corona's properties that are incompatible with the oscillation model. Similarly, the study by Bollemeijer et al. (2023) supports the precession of the hot inner flow as an explanation for the origin of QPOs and possibly for the observed time lags as well.

The rich literature on MAXI J1820+070 and availability of the data from a broad energy range in X-rays (0.3-80 keV), spanning over several months and extending to various flux and spectral states, were major drives to choose this source for this project. Many articles on this target, explaining one or multiple epochs comprehensively, are already published, hence enabling a strong background of the known properties, added to the motivation behind this object.

2 The telescopes

2.1 *XMM*-Newton

The European Space Agency's X-ray Multi-mirror (*XMM-Newton*) mission, launched from Kourou, French Guiana on 10 December 1999, is the ESA's most powerful telescope ever placed in orbit. The 3.8-tonne satellite harbours three advanced telescopes, each with a mirror module consisting of 58 Wolter I grazing-incidence mirrors, nested in a coaxial and co-focal configuration alongside baffles to suppress stray visible and X-ray photons and an electron deflector for diverting soft electrons. The optics design utilizes very shallow grazing angles to enable sufficient reflectivity at high energies. It is most efficient in the 0.1-10 keV energy band (ESA: XMM-Newton SOC, 2023).

The *XMM*-Newtonsatellite consists of 6 simultaneously operating, co-aligned instruments, the three EPIC (European Photon Imaging Camera) imaging X-ray cameras, the two RGS (Reflection Grating Spectrometer) grating X-ray spectrometers and the OM (Optical Monitor). EPIC is the prime focus of the three mirror modules aboard the *XMM*-Newtonsatellite, with two of the three modules equipped with the RGS. The optical monitor provides complementary data to X-ray observations by simultaneously observing the UV/visible region.

2.1.1 European Photon Imaging Camera (EPIC)

The EPIC comprises three X-ray CCD cameras, two of which consist of an array of seven EPIC-MOS ((Metal Oxide Semiconductor) CCD arrays installed behind the telescopes equipped with RGS. The third CCD is the EPIC-pn camera, consisting of 12 individually operated pn-CCDS. All EPIC CCDs offer extremely sensitive imaging observations over the telescope FOV of 30 arcmin and an energy range of 0.15-15 keV with a moderate spectral ($E/\Delta E \sim 20-50$) and angular resolution (6" FWHM) (ESA: XMM-Newton SOC, 2023). The angular resolution is determined by the X-ray mirror module's point-spread function (PSF), a critical parameter that defines the ability to focus incoming photons.

The EPIC cameras allow for several operating modes. In the full frame mode, all CCD pixels are read out, covering the full FoV. In the partial window mode for the central CCD of both MOS cameras, only part of the CCD is read out in either the small window mode (100 X 100 pixels) or large window mode (300 x 300 pixels). For EPIC-pn, half of the area of all 12 pn-CCDs is read out in large window mode, whilst only part of a single pn-CCD is read out in the small window mode. For MOS and pn, the timing mode maintains spatial information in only one dimension, along the column axis (RAWX). Spatial information in the row axis (RAWY) is lost due to the continuous shifting and collapsing of rows for fast readout times.

Each successive mode has a higher max count rate which is set by the deteriorating response due to photon pile-up. Photon pile-up occurs when more than one X-ray photon arrives at a camera pixel or adjacent pixels before being read out, compromising the PSF and spectral response (ESA: XMM-Newton SOC, 2023). When pile-up occurs, many photons arrive within one readout frame in the core of the PSF, creating multi-pixel photon patterns. The event reconstruction software onboard the MOS camera rejects these events whilst for pn it has to be done offline using SAS. Pile-up affects the spectral response because the charge of multiple photons in one readout frame is summed, creating an artificial hard or higher energy photon instead of multiple soft photons. A significant amount of X-ray events are expected to be split between pixels. The pile-up effects on the spectral shape can be reduced by selecting only mono-pixel events. For extreme cases of pile-up, high-accuracy spectra can still be built by excising the heavily piled-up core of the PSF.

2.2 *Nu*STAR

The *Nuclear Spectroscopic Telescope Array* (*Nu*STAR) mission was launched on June 13th, 2012 and marks a pioneering milestone in the field of astronomy by being the

first space-based telescope to harness cutting-edge hard X-ray optics and solid-state detector technologies. This advanced equipment empowers *Nu*STARto conduct exceptionally sensitive observations at X-ray energy levels exceeding 10 keV. The *Nu*STARinstrument is specifically engineered to concentrate X-rays within the energy range of 3 to 79 keV.

The *Nu*STARX-ray optics implements a Wolter-I conical approximation and consists of 133 concentric mirror shells, coated with depth-graded multilayers (*NuSTAR Instrumentation* 2023). Multilayers are thin layers of alternating material with differing densities, positioned on top of one another. A high-density contrast allows for enhanced reflectivity. *Nu*STARutilizes Tungsten(W) and Platinum (Pt) for high-density layers and Silicone(Si) and Silicon Carbide (SiC) for low-density layers. The multilayer coatings coupled with low-graze angle X-ray optics enable significant collective area up to 78.4 keV. At this point, it drops significantly due to the Pt K-absorption edge (Harrison et al., 2013).

*Nu*STARimplements two of the aforementioned optic units, each with its own detector unit or focal plane module. Each detector unit is comprised of a two-by-two array of solid-state Cadmium-Zinc-Telluride (CdZnTe) detectors, surrounded by Cesium-Iodide (CsI) crystals which act as an anti-coincidence shield. The anti-coincidence field identifies high-energy photons and cosmic rays crossing the focal plane from directions other than along the *Nu*STAROptical axis. For energies below 40 keV, the energy resolution is 0.4 keV FWHM, increasing to 1.0 keV at 70.0 keV (Harrison et al., 2013).

2.3 *NICER*

Launched on June 3, 2017, aboard a SpaceX Falcon 9 rocket, the Neutron Star Interior Composition Explorer (*NICER*) is a pioneering instrument installed on the International Space Station (ISS). Its primary focus is the study of neutron stars, among other celestial phenomena. *NICER*'s primary focus involves examining the soft X-ray emissions (0.2-12 keV) of these objects with precise timing and spectroscopy (Markwardt et al., 2023).

NICER's X-ray Timing Instrument (XTI) is a sophisticated assembly of 56 X-ray "concentrator" optics (XRC) coupled with silicon drift detector (SDD) pairs. Each XRC gathers X-rays from a substantial 30 arcmin^2 area of the sky and focuses them onto a small SDD. These detectors excel in capturing individual photons with both energy and timing precision, providing excellent spectral resolution ($6 < E/\Delta E < 80$ from 0.5 keV to 8.0 keV, absolute timing precision of < 300 ns and recording detection times of 100 ns RMS relative to Universal Time (Markwardt et al., 2023). This setup offers a high signal-to-noise-ratio photon-counting capability ideal for analyzing the diverse spectra of neutron stars and an array of astrophysical sources.

NICER's design allows it to precisely point and track various celestial targets across nearly a full hemisphere, effectively adapting to the ISS environment. Additionally, *NICER*includes tools such as WebPIMMS and WebSPEC to simulate observations, derive count rates, and generate spectra. The Viewing tool further assists in identifying when specific sky positions, relevant to various celestial objects, are observable by *NICER*. *NICER*'s deployment on the ISS signifies a substantial leap in exploring a range

of celestial objects, not only limited to neutron stars. Its primary focus on investigating soft X-ray emissions, coupled with its precise measurements and advanced observational capabilities, presents a valuable asset to the broader field of X-ray timing.

2.4 *Swift*

The *Swift* Gamma Ray Burst Explorer (Gehrels, 2004) was selected by NASA as their medium-sized explorer (MIDEX) mission in October 1999 and successfully launched on November 20, 2004. Equipped with three advanced instruments, this mission aimed to enhance our understanding of GRBs and various other astrophysical phenomena.

One of the key instruments on board is the Burst Alert Telescope (BAT; Barthelmy et al., 2005), which was primarily designed to identify GRBs and accurately determine their celestial coordinates within a few arcminutes. Complementing the BAT is the Ultraviolet/Optical Telescope (UVOT; Roming et al., 2005), boasting a remarkable sensitivity limit of 24th magnitude in just 1000 seconds of observation time. Additionally, the UVOT provides a remarkable position accuracy of 0.3 arcseconds. Completing the suite of instruments is the X-ray Telescope (XRT; Burrows et al., 2005). The *Swift*-XRTis an exceptionally sensitive and versatile X-ray imaging CCD, specifically engineered to measure fluxes, spectra, and light curves of GRBs and their afterglows. Notably, the XRT possesses a wide dynamic range, spanning over 7 orders of magnitude in flux.

Together, these instruments synergistically form a robust multiwavelength observatory, enabling the rapid determination of GRB positions with an impressive accuracy of arcseconds within 1-2 minutes of detection. This cutting-edge setup not only facilitates the measurement of light curves and redshifts of GRBs but also enables the study of a diverse range of astrophysical phenomena.

2.4.1 XRT

The XRT is an X-ray telescope that utilizes a grazing incidence Wolter 1 telescope to focus X-rays onto a state-of-the-art CCD. The telescope has an effective area of 110 cm2, a field of view of 23 arcmin, a resolution of 18 arcsec (half-power diameter), and an energy range of 0.2-10 keV. The mirror module of the XRT consists of the X-ray mirrors, thermal baffle, mirror collar, and electron deflector. The X-ray mirrors are FM3 units that have been built, qualified, and calibrated as flight spares for the JET-X instrument on the Spectrum X mission (Citterio et al., 1996; Wells, Stewart, et al., 1992; Wells, Castelli, et al., 1997). To maintain the performance of the mirror module in orbit, it will be actively controlled and maintained at a temperature of 20 ± 5°C with gradients of less than 1°C, similar to the thermal baffle used for JET-X.

The focal plane camera of the XRT is housed in a composite telescope tube and contains a single CCD-22 detector. The CCD-22 detector, originally designed for the EPIC MOS instruments on the *XMM*-Newtonmission, is a three-phase frame-transfer device that utilizes high resistivity silicon and an open-electrode structure to achieve a useful bandpass of 0.2-10 keV. The CCD consists of an image area of 600 × 602 pixels (40 × 40 mm) and a storage region of 600 × 602 pixels (39 × 12 mm). The energy resolution of the CCD, measured as the full width at half maximum (FWHM), decreases from

approximately 190 eV at 10 keV to approximately 50 eV at 0.1 keV (Gehrels, 2004). However, below 0.5 keV, the effects of charge trapping and loss to surface states become significant.

The XRT functions across three distinct readout modes, adapting to the diverse and dynamic behaviours frequently witnessed in the afterglows of Gamma-Ray Bursts (GRBs) (Burrows et al., 2005). With autonomous functionality, it selects the most appropriate readout mode based on the specific characteristics of the observed phenomenon. These modes sequenced according to their handling of bright flux and typically used following a GRB event, encompass the Image Mode, the Windowed Timing Mode, and the Photon-Counting Mode.

The Image Mode in the XRT operates by using the CCD like an optical CCD, collecting accumulated charge without specific X-ray event recognition. Its primary function is to generate images that provide accurate positional and flux data. However, it is not suitable for spectroscopic analysis due to the potential for pile-up in typical GRBs. This mode operates at a low gain, enabling observations up to the full-well capacity of the CCD. It dynamically selects exposure times of either 0.1 or 2.5 seconds based on the source's flux. Image Mode is most effective for source fluxes between 25 mCrabs and at least 45 Crabs, producing various data products such as GRB centroid positions, X-ray flux estimates, postage-stamp images, and compressed images, which are distributed through the Gamma-ray burst Coordinate Network (GCN).

The Windowed Timing Mode of the XRT utilizes a 200-column window that covers the central 8 arcminutes of the Field of View. This mode retains imaging in only one dimension but focuses on capturing timing information along each column. With a time resolution of 1.8 ms, it is highly effective for fluxes below 5000 mCrabs and minimizes pile-up concerns below 1000 mCrabs. Ground-processed data in this mode are provided as FITS binary table events files, detailing the 1-D position, arrival time, energy, and pattern of each X-ray event.

The Photon-counting Mode of the XRT maintains full imaging and spectroscopic resolution but offers a time resolution of 2.5 seconds. It follows a "normal" CCD readout sequence, reading the entire CCD every 2.5 seconds. This mode is ideal for fluxes below 1 mCrab and delivers ground-processed data as FITS binary table events files. These files include detailed information such as the 2-D position, arrival time, energy, a 3×3-pixel neighbourhood centred on the event, and the event grade (or pattern). Event grades are determined using a system similar to the *XMM*-Newton/EPIC MOS pattern library and are assigned during ground processing.

The XRT's automated operating modes are specifically designed to mitigate the effects of pileup in most observations. Typically, photon pileup remains minimal for source fluxes below 1 Crab. In the Windowed Timing mode, the CCD undergoes continuous clocking in the parallel shift direction, creating an image characterized by a vertical streak across the CCD. Pileup in WT mode manifests as a central streak that is heavily piled up, flanked by lower count rates emanating from the wings of the PSF. In instances where very bright sources exhibit severe pileup, WT mode allows for analysis by only utilizing the wings of the PSF. To facilitate this analysis, the `xrtmakearf`

program is capable of generating the specific ARFs required for pile-up analysis (Burrows et al., 2005).

3 Data analysis

3.1 Dataset Overview

The data used in this research study is tabulated in Table 1. The MAXI lightcurve in the 2-20 keV energy range is illustrated in Figure 11, where the black and magenta lines indicate the *Nu*STAR and *Swift*-XRT observations respectively. These observations were selected to cover the entire available range of *Nu*STAR observations, encompassing the hard state, the transition from the hard to the soft state, and specific instances of the soft state. Where feasible, *Swift*-XRT data within a day of the *Nu*STAR observations were chosen to complement *Nu*STAR's energy spectra in the softer energies. Correspondingly, *NICER* observations aligned within a day of the *Nu*STAR data were specifically selected for concurrent timing analysis. Epoch 9 of the dataset comprises 4 *NICER* observations, namely 1200120190/192/194/196, coinciding with the state transition. Due to *Nu*STAR's low observing cadence and the rapid state transition of MAXI J1820+070, *Nu*STAR alone has proved insufficient to completely characterize the state transition. *NICER* emerged as a more effective tool for probing the timing characteristics of the intermediate state due to its higher observation cadence. For this reason, we select 5 *NICER* observations (Observations 189, 190, 192, 194 and 196) to analyze the timing characteristics during the IMS.

MJD	**Swift/XRT** Obs ID	*Nu***STAR** Obs ID	**NICER** Obs ID	**Epoch**	**State**
58198	-	90401309006	1200120106	1	Hard
58201	-	90401309010	1200120110	2	Hard
58202	00010627014	-	-	2	Hard
58212	00088657001	90401309012	1200120120	3	Hard
58224	00010627043	-	-	4	Hard
58225	-	90401309014	1200120131	4	Hard
58241	00088657003	90401309016	1200120144	5	Hard
58255	00088657004	90401309019	-	6	Hard
58259	-	90401324002	1200120155	7	Hard
58297	00088657006	90401309021	1200120189	8	IMS
58[298-304]	-	-	1200120[190-196][1]	9	IMS
58314	00088657008	90401309025	-	10	Soft
58327	-	90401309027	-	11	Soft

[1] *NICER* observations aligned with the hard-to-soft state transition.

Table 1: Compilation of Swift/XRT, *Nu*STAR, and *NICER* observations of MAXI J1820+070 utilized in this study. Observations within a 1-day proximity are grouped into single epochs, excluding epoch 9.

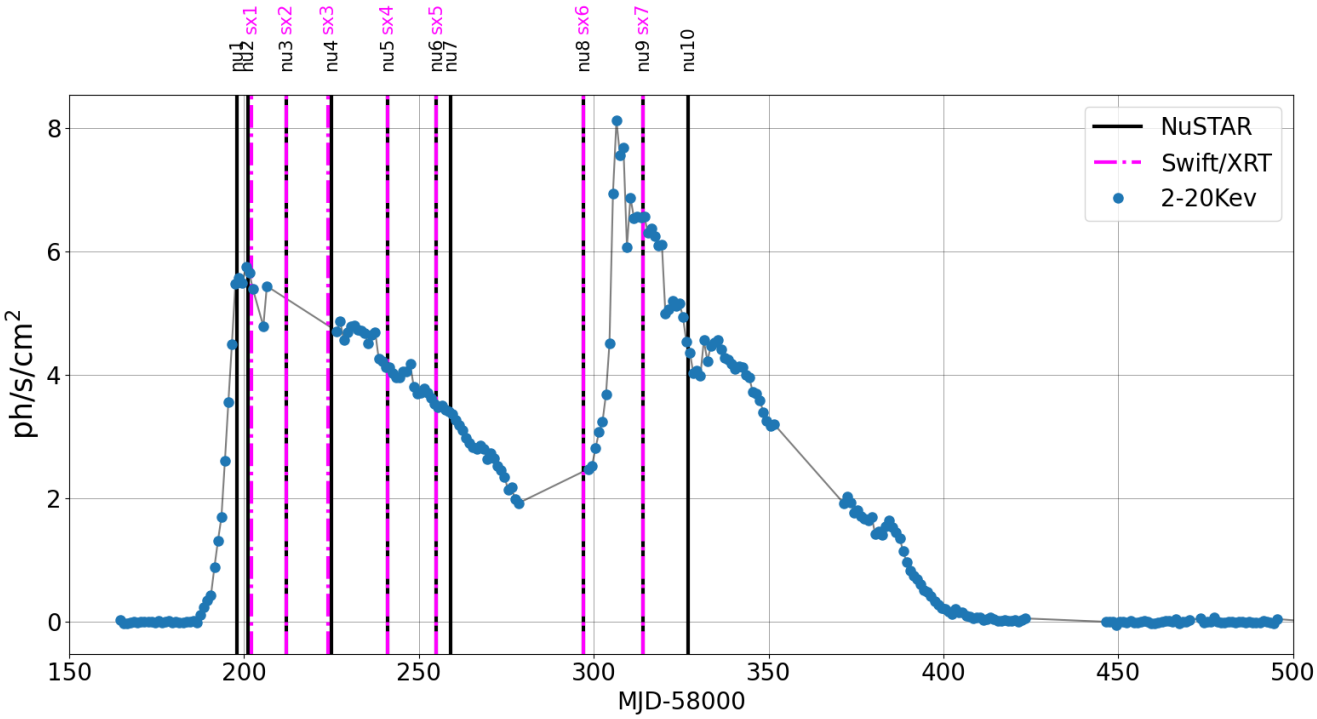

Figure 11: Lightcurve of MAXI J1820+070 captured by MAXI in blue, showcasing the temporal alignment of *Nu*STAR (black) and Swift/XRT (magenta) observations indicated by vertical bars. *NICER* observations, nearly simultaneous with *Nu*STAR data, are omitted for clarity.

3.2 Data reduction

3.2.1 XMM-Newton

The data reduction was performed using the *XMM*-Newton Science Analysis System (SAS version 20.0.0) and HEASoft (version 6.30.1) on Ubuntu 20.0.4. The retrieved *XMM*-Newton data come in two sub-directories, the Observation Data Files (ODF) and Pipeline Processing (PPS) files. For SAS to operate correctly, certain parameters must be configured. The script to initialize SAS handles two of these parameters, namely `SAS_DIR` and `SAS_PATH`, which both define the path to the SAS directory. The remaining parameters, `SAS_CCFPATH`, `SAS_ODF` and `SAS_CCF`, set the directory path to the Current Calibration File (CCF) data, ODF data and Calibration Index file (CIF) respectively. To carry out various SAS tasks, it is often necessary to obtain calibration information from the Calibration Access Layer (CAL). The relevant files can be accessed from the set of CCF data using the CIF. A CIF is included in the PPS files, however, if the CCF has been updated it can be created using the command `cifbuild`. By extracting data from instrument housekeeping data files and the calibration database, the task `odfingest` adds information to the summary file of the ODF. Once `odfingest` has been executed, it will be necessary to update the environment variable `SAS_ODF` to point to the output file it generates. After setting the appropriate environment variables, the pipeline is rerun with the command `epproc` to produce calibrated photon event files for the PN camera.

Before extracting the spectrum, the event list is filtered for periods of high background flaring activity. This is accomplished by creating a good time interval (gti) file with the command `tabgtigen`. The gti file is created by extracting a single-event, high-energy light curve and determining a threshold (count/second) just above the low steady background. The intervals above this threshold are ignored, and a gti file containing information on the low background intervals is created. Due to MAXI J1820+070's extreme brightness during its outburst, the EPIC-PN camera operated in timing mode. An image is created in sky coordinates, however, since the events list consists of timing mode events, the image only contains one physical dimension on the X-axis (RAWX) while the Y-axis (RAWY) contains timing information. An example image of an *XMM*-Newton observation of MAXI J1820+070 used in this study is displayed in Figure 12. The events list is then filtered with the gti using the command `evselect`.

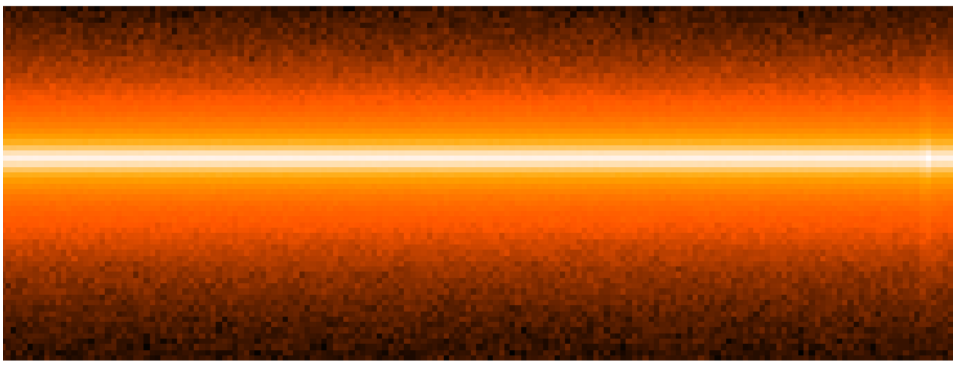

Figure 12: DS9 image of an *XMM*-Newton observation of MAXI J1820+070 using the EPIC-pn camera in windowed timing mode.

The *XMM*-Newton observations of MAXI J1820+070 suffer from the effects of pile-up. To remedy this effect, the central column is excised before extracting the spectrum. To evaluate whether pile-up is still present, a filtered events list is extracted including only photons within the source region, with the central column excised, and the task `epatplot` is applied to the filtered event list. The resulting 'POSTSCRIPT' file, displayed in Figure 13, shows the distribution of the observed versus expected pattern. If the source spectrum is affected by pile-up. there will be a significant discrepancy between the expected and observed distributions. `epatplot` computes a pair of diagnostic values (i.e. the single and double pattern ratios) that can be employed to evaluate the existence of pile-up. When no pile-up is detected, both the observed-to-model fractions of singles and doubles patterns, calculated for the default range of 0.5 - 2.0 keV, should exhibit consistency with 1.0, accounting for statistical errors (1 sigma

errors are provided). Conversely, if pile-up is present, the singles ratio will be less than 1.0 while the doubles ratio will exceed 1.0. The resulting ratios are outputted to the console and visualized on the plot. In case the event list that remains is still impacted by pile-up, it becomes necessary to increase the number of columns that are removed until the resulting event list is free from pile-up.

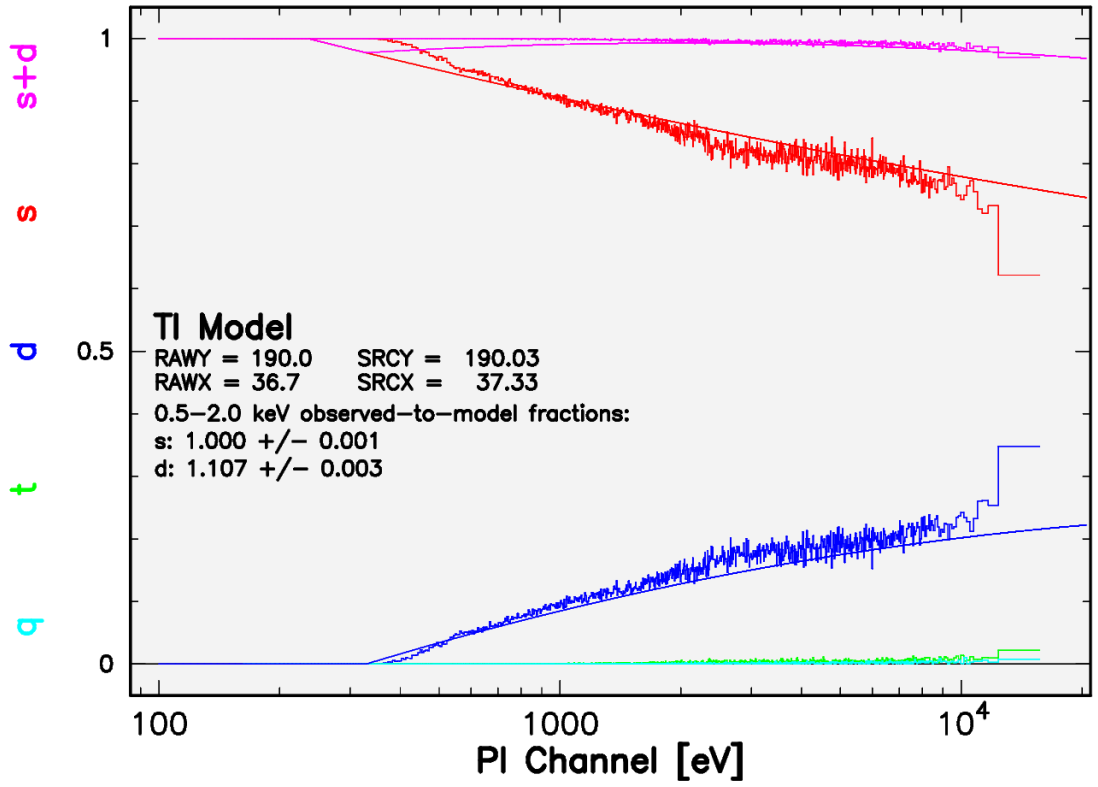

Figure 13: The Figure compares the expected pattern distribution functions (smooth solid lines) with the observed ones (histogram) of an *XMM*-Newton observation of MAXI J1820+070 using the EPIC-pn camera. The panel also displays the observed-to-model fractions for both single and double events in the 0.5-2.0 keV energy range. The colours distinguish distinct pattern classes: red for single events, blue for double events, green for triple events, and turquoise for quadruple events.

Once the source region is free from pile-up, a spectrum is extracted using a previously generated gti file. A background spectrum is extracted from a source-free region. The `backscale` task is employed to calculate the area of the source and background regions utilized in generating the spectral files. This area information is then stored in the spectrum table of the file as the keyword 'BACKSCAL' in the header. The SAS task `rmfgen` is employed to create a redistribution matrix file (rmf) for the previously extracted spectrum. The task `arfgen` is employed to generate an ancillary file (arf). The source spectrum, background spectrum, arf and rmf files are grouped using the task `ftgrouppha` using the Kaastra & Bleeker optimal binning scheme (Kaastra and Bleeker, 2016).

3.2.2 *Nu*STAR

The data reduction process was executed through HEASoft (version 6.30.1) on Ubuntu 20.0.4. Once HEASoft was initialized, the *Nu*STAR data underwent analysis using the `nupipeline`, included in the HEASoft software package. This involved specifying three primary details: the input path leading to the main directory encompassing the observations for processing, the stem name for the data files, and an output directory. Within the output directory, event files were processed to ensure calibration and cleaning, accounting for Good Time Intervals (GTIs) and screening for passages through the South Atlantic Anomaly (SAA) for both FPMA and FPMB detectors. Although *Nu*STAR comprises similar telescopes focusing on two similar focal plane arrays, each telescope and its corresponding array are not identical. Therefore, analyzing data from these telescopes necessitates separate treatments. The ultimate joint analysis of combined data occurs during the final stage, specifically during joint spectral fitting.

The cleaned event files were plotted as images in DS9, enabling the definition of source and background regions for both arrays. An example source and background region is displayed in Figure 14. The delineated region information was then saved using DS9. Background levels within *Nu*STAR exhibit variations across the field of view and among the four CZT detectors located on each focal plane. Addressing the background contributions to the spectrum of the source region remains a topic of ongoing discussion in the scientific community and is recognized as a complex issue. For this study, the background was estimated by extraction from a nearby region to approximate the background in the source region. Subsequently, the `nuproducts` task was executed to generate light curves, images, and spectra using the previously defined source and background region files. To ensure accuracy in the data analysis, barycenter correction was applied by setting the `barycorr` variable to 'yes'. The resultant output files comprised the barycenter-corrected, cleaned event file, source and background energy spectra, and the source Auxiliary Response File (ARF) and Redistribution Matrix File (RMF). These files were then grouped using the `ftgrouppha` task, employing the Kaastra & Bleeker optimal binning scheme(Kaastra and Bleeker, 2016). Barycenter correction is essential as it adjusts for the motion of the spacecraft or satellite relative to the barycenter of the solar system. This correction is necessary to ensure precise timing and positional accuracy in the recorded astronomical events.

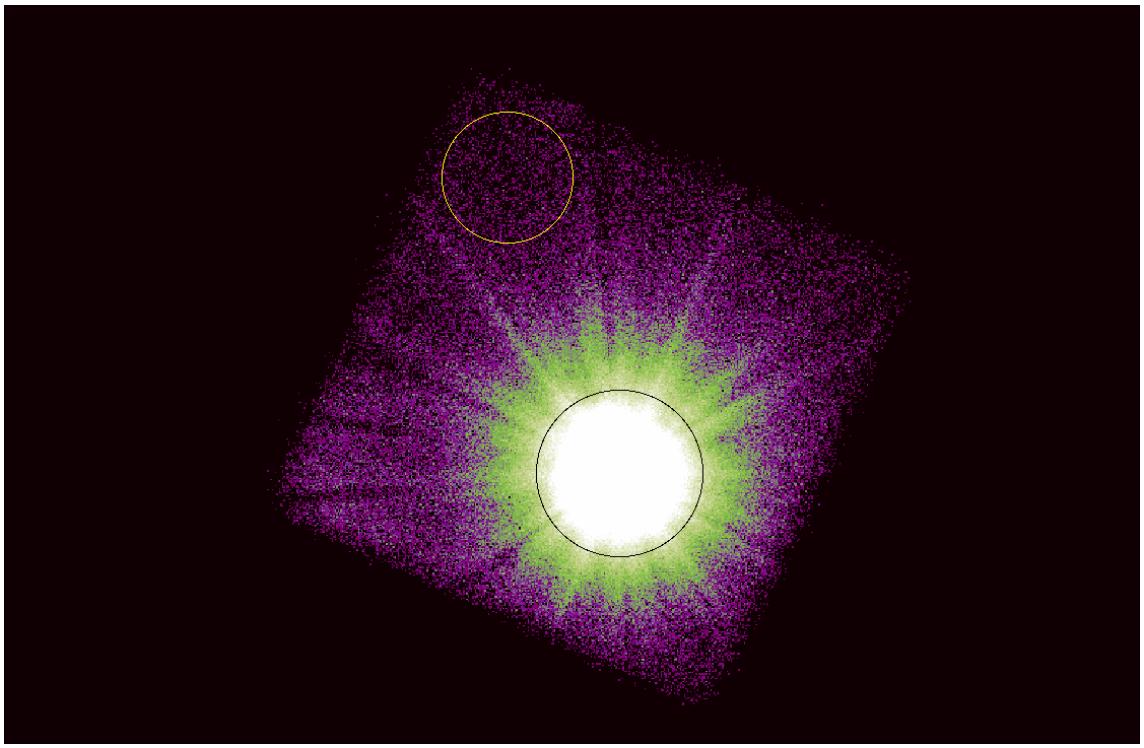

Figure 14: DS9 image of a *Nu*STAR observation of MAXI J1820+070. The black circle delineates the source region. The yellow circle denotes the selected background region

3.2.3 NICER

The data reduction process for *NICER* utilized the identical HEASoft software and Ubuntu configuration employed for the *Nu*STAR analysis. The processing of *NICER* data involved the utilization of the *NICER* level 2 standard calibration and filtering tool `nicerl2`, included in the HEASoft software package. This comprehensive tool facilitated the application of essential *NICER*-recommended calibration processes and standard screening procedures across the entire *NICER* observation dataset. Through a sequence of processing steps performed by the `nicerl2` task, including `nicercal` for standard *NICER* calibration, `niprefilter2` for deriving the calibrated filter (MKF) file, `nimaketime` to establish standard screening good time intervals, `nicermergeclean` for merging per-MPU data and filter/screen, and `niautoscreen` for automatic screening to identify problematic per-FPM and per-MPU conditions, the data underwent thorough processing.

The resulting output files were deposited into a designated directory specified by the 'cldir' variable. These outputs comprised per-module "Ufa" files, providing lightly screened and calibrated event files for each MPU, as well as a master "Ufa" file representing the entire array with the same screening and calibration. Additionally, a master 'cl' file, reflecting the screened and calibrated event file based on nimaketime screening, was generated. To ensure accuracy, a revised "mkf" file was updated using `niprefilter2`, integrating the applied calibrations. Finally, the `barycorr` task was run to apply barycenter correction to the master 'cl' file.

3.2.4 Swift/XRT

The data reduction process for *Swift*-XRT data utilized the identical HEASoft software and Ubuntu configuration employed for the *Nu*STAR and *NICER* analysis. To produce cleaned event files (i.e. the level 2 data file), the Swift/XRT pipeline `xrtpipeline` is employed. The main inputs required for the pipeline are the source RA and DEC positions, the target and output directly and lastly, the stem inputs for the raw FITS files. To produce an exposure map, the variable `createexpomap` is set to 'yes'. The exposure map is needed to generate an ARF file.

To generate an image from the processed event file, we employ the 'XSELECT' command, which serves as an interface for the image and spectra extraction script, known as `extractor`. After initializing the HEASoft environment and launching XSELECT, the cleaned event file is imported. Subsequently, an image is extracted and visualized within XSELECT using the 'plot image' command, with the resulting image viewable in DS9. All of the XRT observations used in this study were conducted in windowed-timing mode, owing to MAXI J1820+070's exceptionally bright outburst. The resulting extracted images are therefore one-dimensional. The DS9 image of an example *Swift*-XRT observation of MAXI J1820+070 can be seen in Figure 15. To ensure accurate analysis, both the source and background regions are defined using annuli. This approach is adopted to exclude the central bright region and mitigate pile-up effects, akin to the methodology employed in *XMM*-Newton data reduction. Specifically, for each observation, an annulus with an inner radius of 15 image pixels and an outer radius of 45 is used. To maintain consistency, an annulus for the background region with a difference between the inner and outer radii of 30 pixels for each observation is adopted.

Utilizing the outputs from the source and background regions, the source and background spectrum are extracted in `XSELECT` . For *Swift*-XRT observations, RMF files are readily available in the HEASoft calibration data (CALDB). However, ARFs need to be created for each specific observation. This is accomplished using the '`xrtmakearf`' command, utilizing the previously generated source spectrum and exposure map as inputs. Once the ARF file is generated, the source and background spectra and the RMF and ARF files are grouped using the `ftgrouppha` task using the Kaastra & Bleeker optimal binning scheme as before.

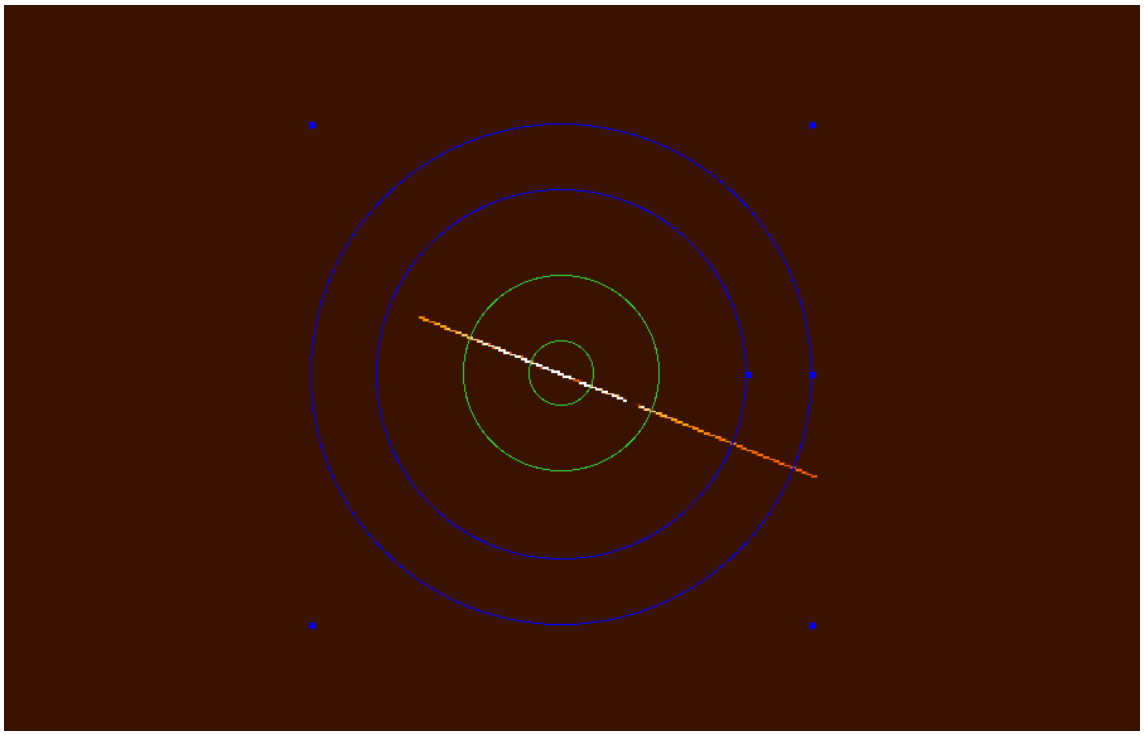

Figure 15: DS9 image of a *Swift*-XRT observation of MAXI J1820+070 in windowed timing mode. The green annulus defines the source region, the blue annulus serves as the background region, and the central line indicates the source flux.

4 Results

4.1 Light Curves and hardness-intensity diagram

The one-day averaged lightcurve data obtained from the MAXI archive were processed and plotted in PYTHON, as depicted in the upper panel of Figure 16. These light curves were segmented into four distinct energy bands: 2-20 keV, 2-4 keV, 4-10 keV, and 10-20 keV. Furthermore, a plot was created in PYTHON to illustrate the hardness versus time relationship, focusing on the 4-10 keV and 2-4 keV bands. This hardness vs time plot is shown in the lower panel of Figure 16, where the hard and soft states are highlighted in different shades of grey, with intermediate states in between. The boundaries for these state transitions were determined by referencing the lower plot in Fig. 16 and consulting the literature (Buisson et al., 2019).

The MAXI lightcurves exhibit a rapid ascent around MJD 58180, peaking at MJD 58200 with a luminosity of 6 ph/s/cm^2 within the 2-20 keV energy range, followed by a gradual descent over 20 days. This gentle decline persists for approximately 90 days, with the hardness ratio remaining relatively stable at around 0.75, indicative of the system remaining in the hard state. At MJD 58300, there is a marked intensification in the light curve across all energy bands, reaching a new peak of 8 ph/s/cm^2 in the 2-20 keV band. This pronounced ascent is once more succeeded by a gradual decline, lasting roughly 80 days. During this phase, the hardness ratio undergoes a significant reduction, signifying the transition to the soft state. Towards the end of this gradual descent, the light curve displays a subtle resurgence, particularly noticeable within the 4-10 and 10-20 keV energy bands. This resurgence is accompanied by a sharp elevation in the hardness ratio, indicating the system's reversion to the hard state.

Furthermore, a HID was generated using PYTHON based on the MAXI lightcurve data, as depicted in Figure 17. The hardness ratio was calculated by considering energy bands between 4-10 and 2-4 keV. The dynamic evolution path is illustrated through arrows, commencing from the right vertical arrow. Notably, MAXI J1820+070 exhibits a characteristic q-shaped trajectory in the HID. It ascends in intensity while maintaining a relatively stable hardness ratio, gradually shifting towards the left of the HID as the spectral hardness decreases. Subsequently, it experiences a decrease in intensity and transitions to the right side of the diagram as it becomes harder.

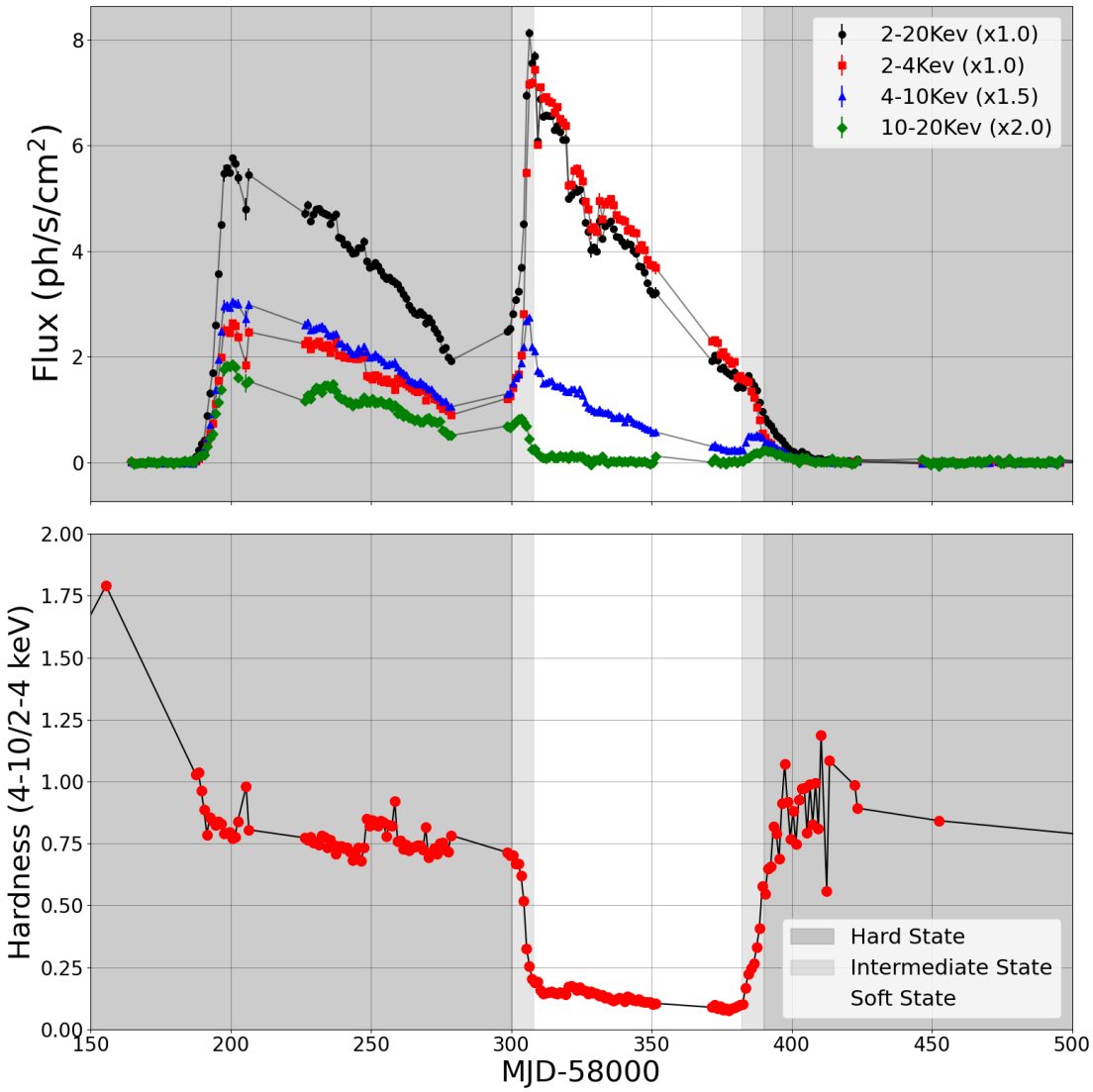

Figure 16: Top Figure: The one-day averaged MAXI light curves of MAXI J1820+070 in four different spectral bands. The different shades of grey represent the hard, intermediate and soft states from darkest to lightest respectively. Bottom Figure: The spectral hardness over time.

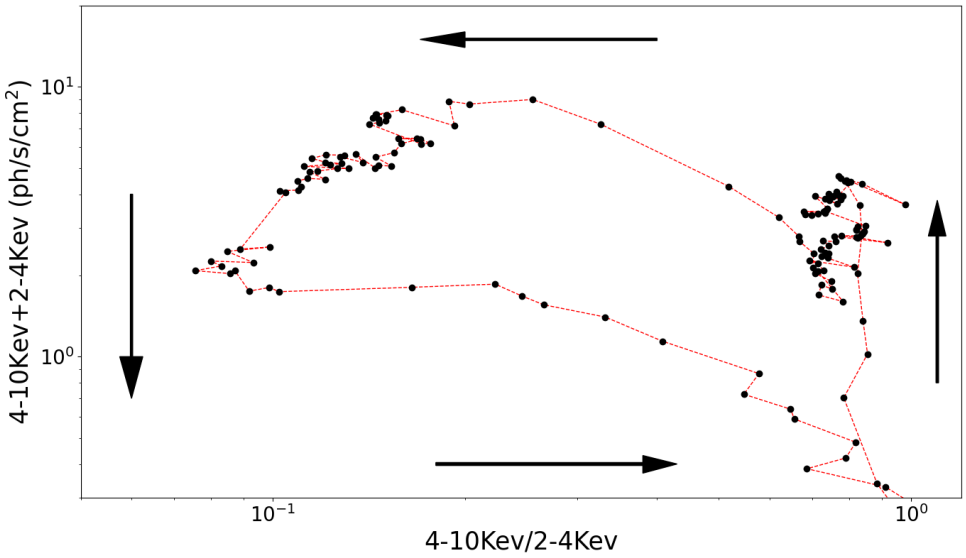

Figure 17: Hardness-intensity diagram of MAXI J1820+070 utilizing MAXI lightcurve data.

4.2 Spectral Modelling

4.2.1 Pile-up in XMM-Newton

To quantitatively characterize the *XMM*-Newton spectra of MAXI J1820+070, an example spectrum in the hard state was fitted with a phenomenological model consisting of a multi-temperature disk blackbody and a simple power-law: `diskbb + powerlaw`, available in the X-ray spectral fitting program XSPEC v12.13.1 (Arnaud, 1996). From Figure 18, there is an evident excess flux in the $\sim 6.0-10.0$ keV range which can be attributed to a relativistically broadened iron Kα line. Notably, between $\sim$ 3 and 5 keV, the model significantly deviates from the data, resulting in multiple spikes. The most likely explanation for these discrepancies is not of physical origin, but rather calibration errors introduced by sharp changes in the effective area of the detector. This explanation is supported by the lower panel of Figure 19, where the effective area versus spectral energy reveals that the positions of the residual spikes between $\sim 1.0-3.0$ keV roughly coincide with the positions of the detector's dips or edges. Furthermore, MAXI J1820+070 was exceptionally bright during the *XMM*-Newton observations, resulting in pile-up, possibly contributing to the residuals observed.

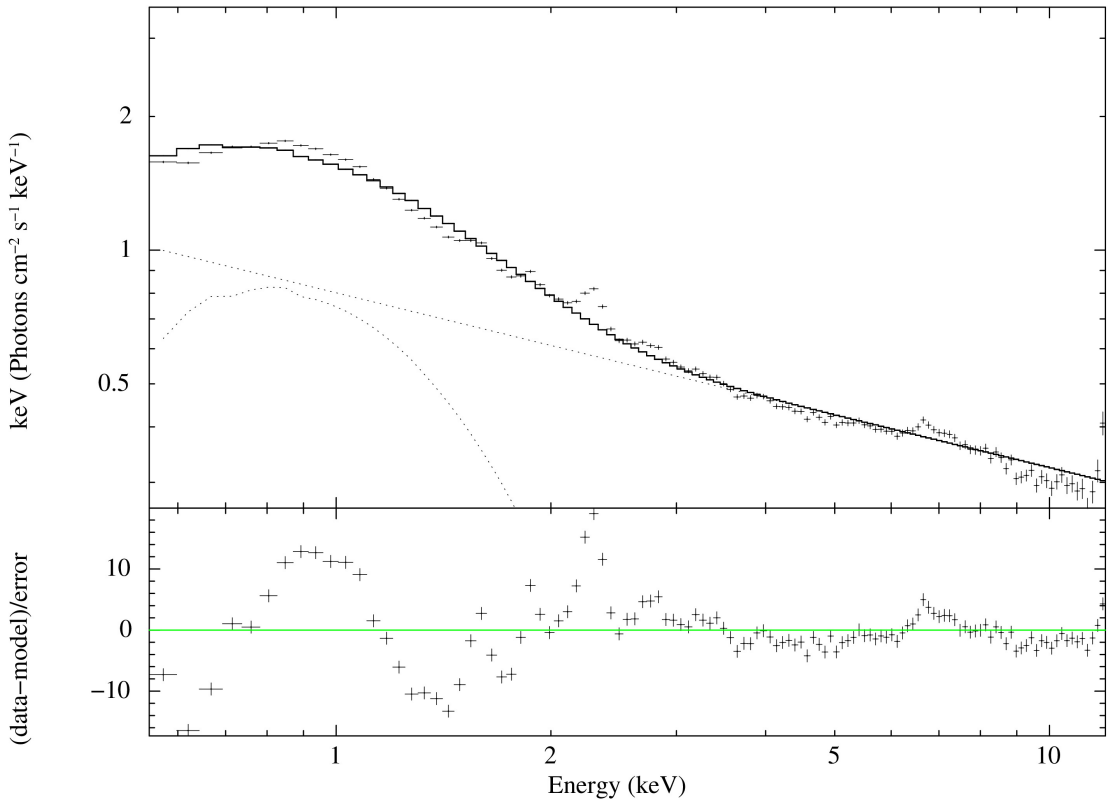

Figure 18: Top: Plot of the unfolded spectrum and model of an *XMM*-Newton observation of MAXI J1820+070 in the hard state, using the model `diskbb + powerlaw`. The data is illustrated by the crosses and the total model is shown by the solid black line. The dotted lines illustrate the individual components of the model. Bottom: Plot the difference between the data and the model, weighted by the error where the error is calculated as the square root of the model predicted number of counts.

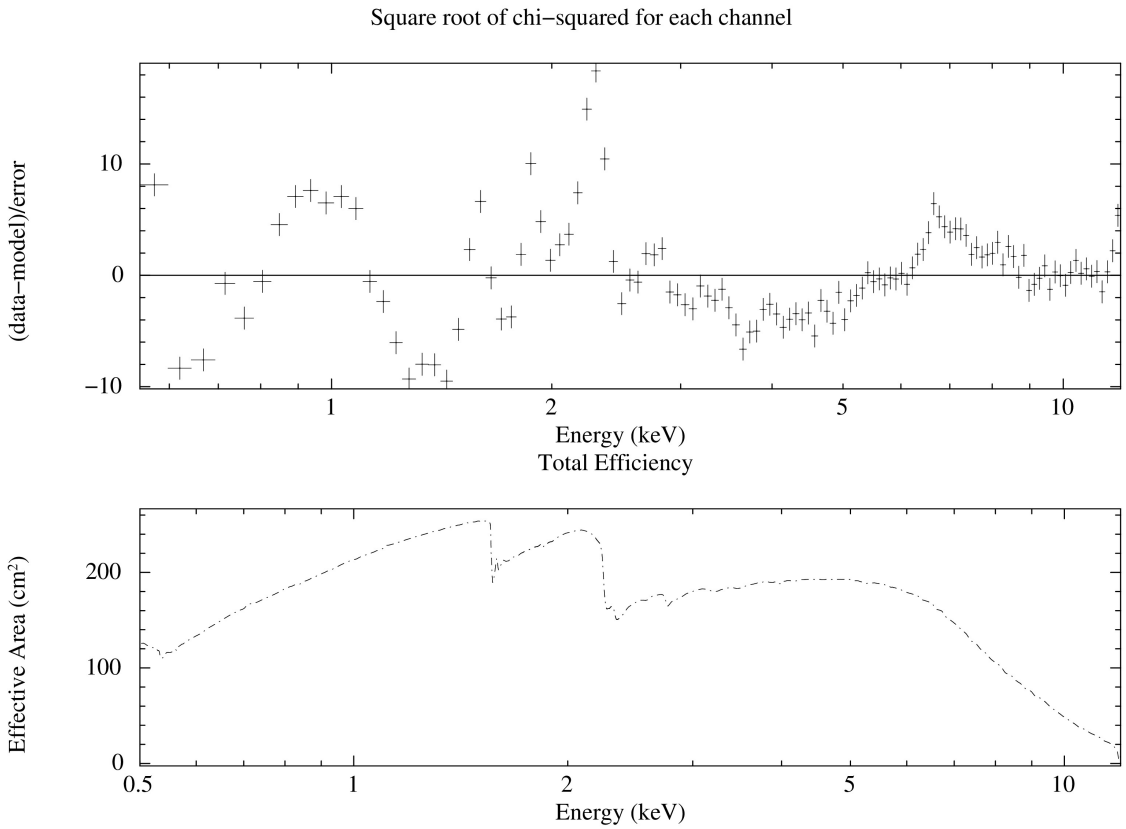

Figure 19: Top: Identical plot of the fit statistics shown in Figure 18.
Bottom: Plot of the total response efficiency of *XMM*-Newton versus incident photon energy.

After the initial phenomenological fit, the *XMM*-Newton observation was fit with a more comprehensive model to include the thermal, non-thermal and reflection component: `Diskbb + Nthcomp + RelxillCp`. The fit with this model is shown in Figure 20. The fit statistic χ^2/degrees-of-freedom is 798.46/93=8.59, a significantly poor fit. In general, a χ^2/d.o.f significantly greater than 1 indicates a poor fit (Bevington, 1969). The model fails to accurately fit the reflection component, likely due to the calibration residuals. An attempt was made to mitigate the effects of calibration residuals by modelling the peaks with a combination of two or three Gaussians. However, it became increasingly difficult to accurately model the residuals while simultaneously maintaining a reasonable fit for the physical emission components. The difficulty was particularly pronounced when attempting to model the thermal component, as the residuals centred around softer energy ranges.

An alternative approach involved excluding the spectral range affected by calibration residuals (1.5-3.0 keV). The fit using this method is shown in Figure 21. The resulting fit statistic is $81.54/68 = 1.20$, a significantly better fit. However, this method inherently excludes a significant portion of the spectral range of the thermal/soft emission, compromising the accurate characterization of the accretion disk. Additionally, the model still fails to fully characterise the reflection spectrum, as evidenced by the residuals still present between 6.0 keV and 8.0 keV.

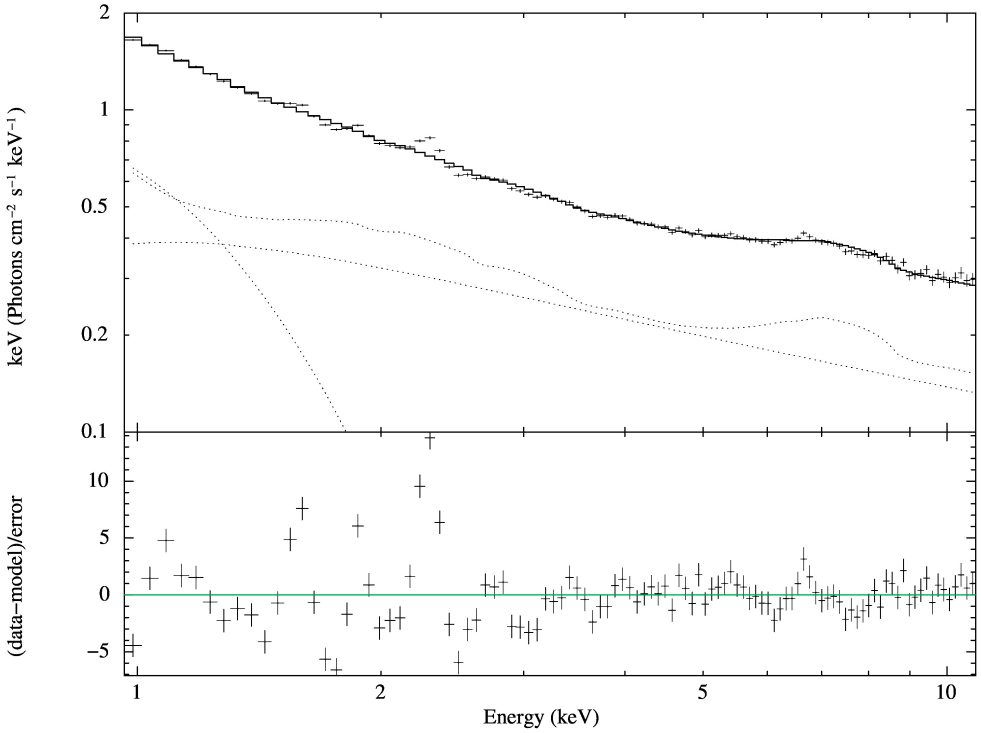

Figure 20: Plot of the unfolded spectrum in Figure 18, fit with the model `Diskbb + Nthcomp + Relxillcp`. The bottom panel depicts the residuals.

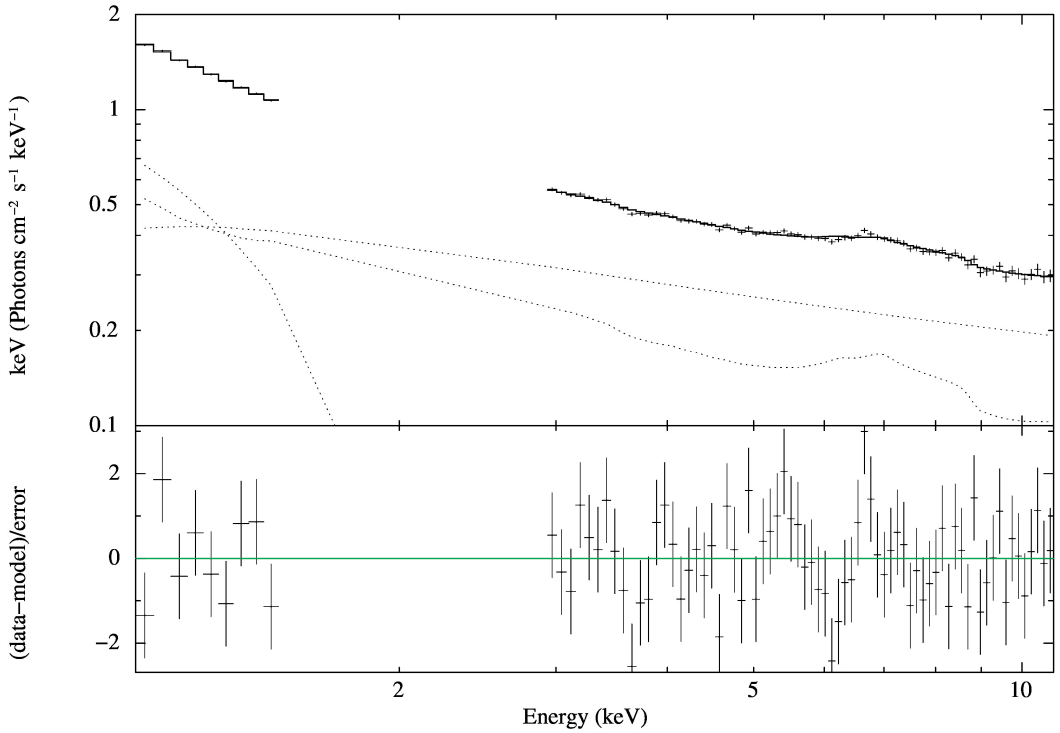

Figure 21: Plot of the unfolded spectrum in Figure 18, fit with the model `Diskbb + Nthcomp + Relxillcp`, excluding the 1.5-3.0 keV energy range from the fit. The bottom panel depicts the residuals.

The effects of calibration errors were present in all *XMM*-Newton observations during the hard state and transition into the soft state. The increasing complexity in modelling the spectra due to the effects of pile-up and calibration errors, coupled with the low observation cadence of *XMM*-Newton during the outburst of MAXI J1820+070, rendered *XMM*-Newton unsuitable for a comprehensive characterization of MAXI J1820+070 during its outburst. Consequently, *Swift*-XRT was employed as a substitute to effectively model the thermal emission.

4.2.2 Phenomenological modelling with *Nu*STAR

The initial spectral analysis of *Nu*STAR began with a simple power law to fit the spectra and assess the various spectral components. Figure 22 illustrates two example spectra in the hard and intermediate state, both fitted with a power law. *Nu*STAR is equipped with two focal plane modules, each producing its own spectrum. When fitting the spectra, the model `CONSTANT` is added to account for the calibration differences between the two modules. The constant value is held fixed for one spectrum and allowed to vary freely for the other.

Three prominent features are observed in both spectra: a soft energy excess below ~ 5 keV, a broad Fe Kα line centred between $6-7$ keV, and a Compton hump spanning $\sim 10-50$ keV. As previously discussed, the soft excess arises from thermal emission from the accretion disk, while the relativistically broadened Fe Kα line and the Compton hump originate from the reflection of the power-law continuum by the accretion disk. A qualitative comparison of Figures 22a and 22b highlights two significant variations. Firstly, there is a noticeable in increase the soft excess, indicating a transition to the soft state, where the thermal component is expected to dominate. Secondly, there is an evolving iron Kα line. In Figure 23, the temporal evolution of the iron Kα line in the hard state is illustrated. The iron Kα line appears to consist of a combination of a stable broad line component and a diminishing narrow line component. This evolving profile strongly suggests dynamic changes in either the disk or corona geometry or a synergistic interplay between the two.

It is evident that the soft excess extends below the lower limitations of *Nu*STAR (~ 3 keV), therefore we include *Swift*-XRT spectra and fit it simultaneously with *Nu*STAR to model the full spectrum of MAXI J1820+070. The *Swift*-XRT spectra allow better modelling of the thermal component by extending the modelled energy range down to ~ 0.5 keV.

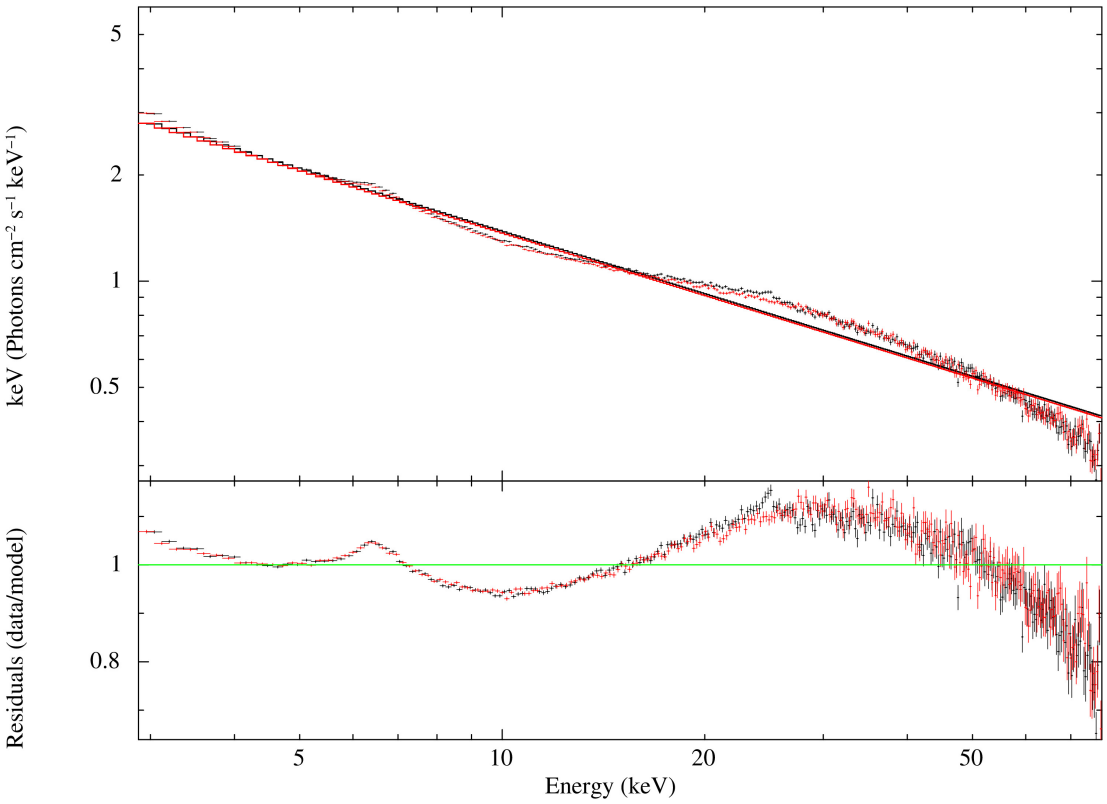

(a) Nu90401309012

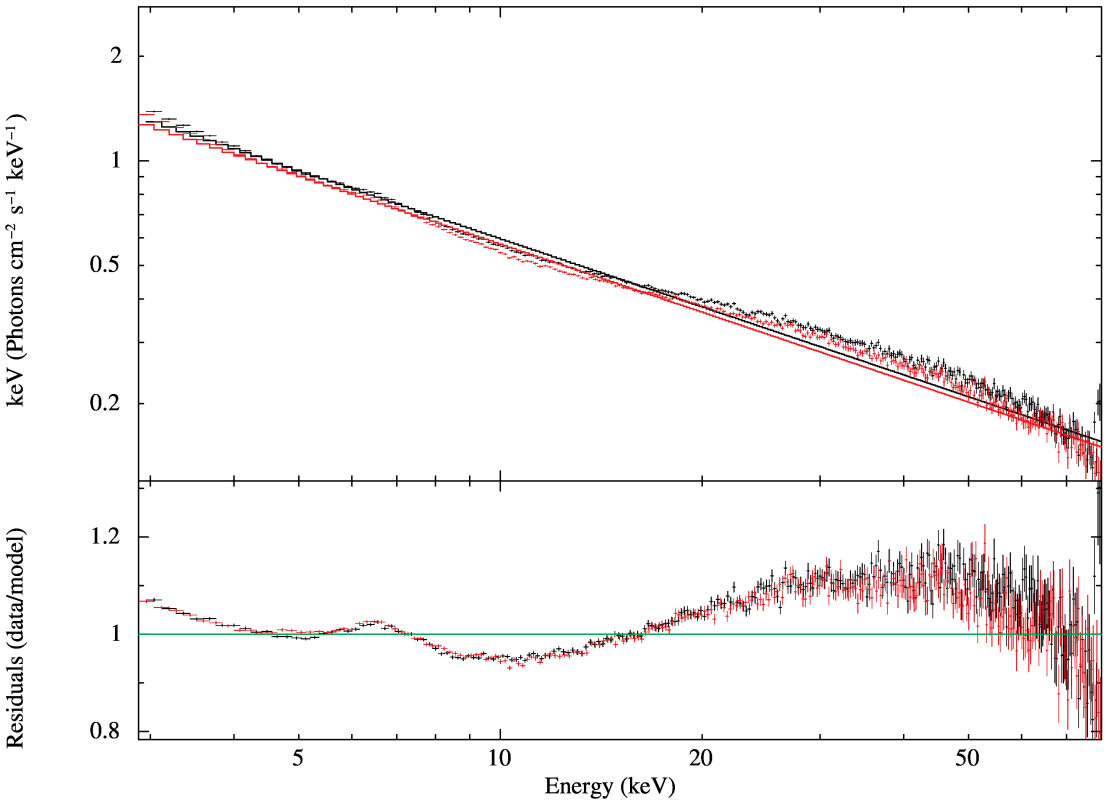

(b) Nu90401309021

Figure 22: Plots of the ratio of the *Nu*STAR spectra to the best-fitting power law. Panel (a) illustrates an observation captured during the hard state and panel (b) corresponds to the beginning of the intermediate state.

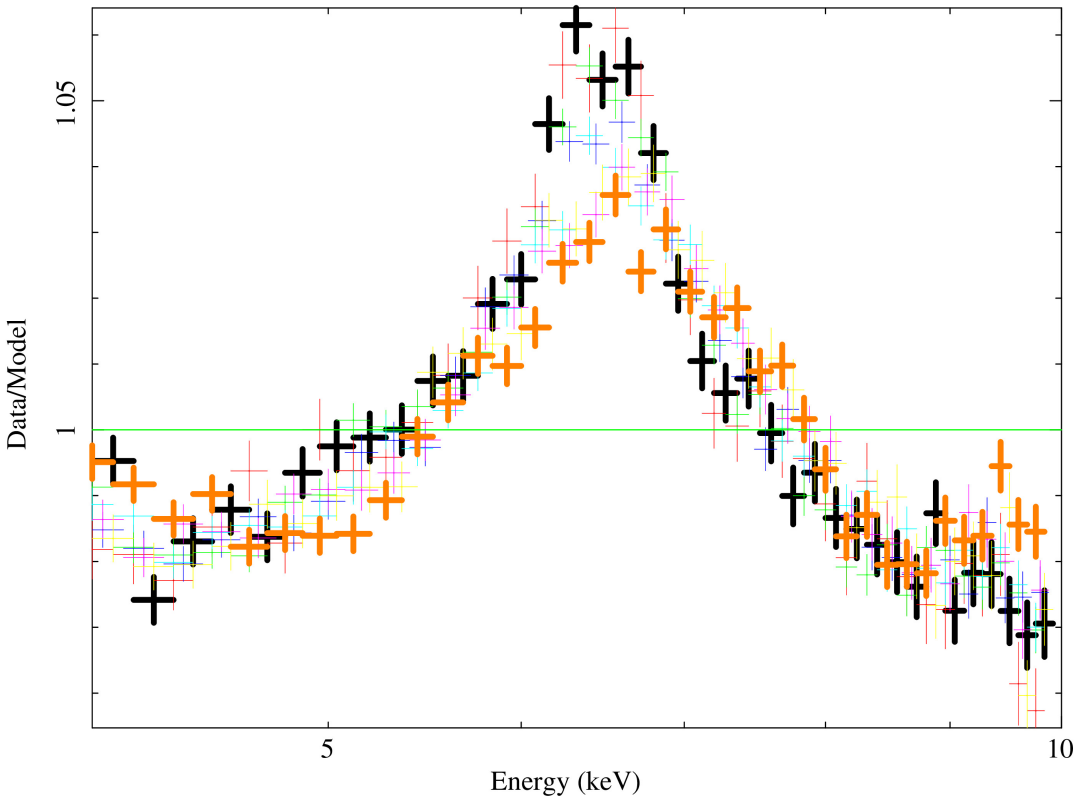

Figure 23: The *Nu*STAR spectra for epochs 1-8 fit with a simple power-law and a constant model for normalization between 4 keV and 10 keV. The black and orange markers, emphasized for clarity, represent epochs 1 and 8, respectively.

In Fig. 22a, a notable discrepancy arises between the FPMA and FPMB spectra within the 20.0-30.0 keV range. Likewise, in Fig. 22b, another disparity is present, spanning 4.0-5.0 keV. Analysis of the total efficiency plot in Figure 24 reveals that the discrepancies between 20.0-30.0 keV can be attributed to variations in the effective area between FPMA and FPMB. Similarly, sharp jumps, accompanied by variations between the effective area of FPMA and FPMB, are evident between $\sim 10.0 - 15.0$ keV and $4.0 - 5.0$ keV. In instances where these residuals are particularly prominent, the relative energy range has been excluded during spectral fitting.

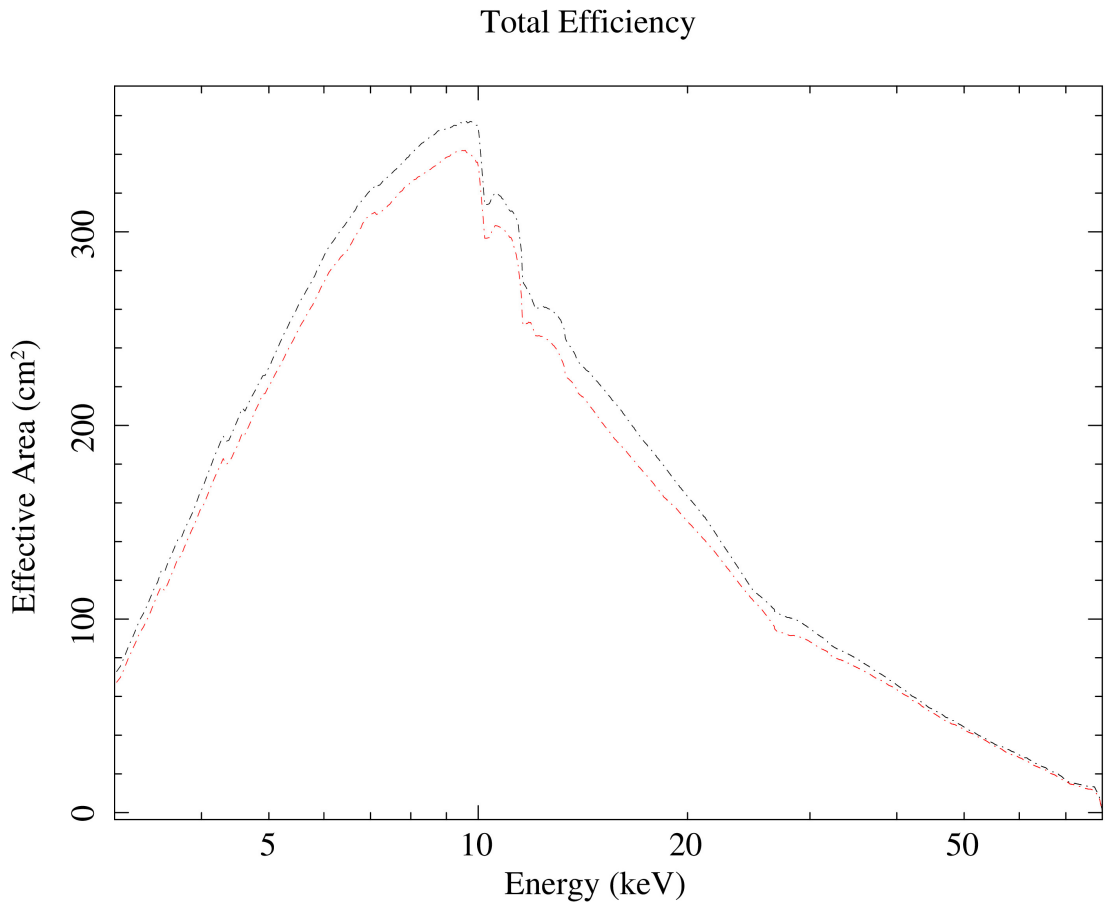

Figure 24: Plot the total response efficiency of *Nu*STAR versus incident photon energy.

4.2.3 A complete model for *Nu*STAR and *Swift*-XRT

After an examination of the spectral components present within the *Nu*STAR spectra, the subsequent step involved choosing a combination of models that accurately characterise the entire spectrum. To effectively model both the direct thermal and non-thermal emissions, a model comprising a multi-temperature disk blackbody (`Diskbb`) and a thermally comptonized continuum (`Nthcomp`: A. A. Zdziarski et al., 1996; Zycki et al., 1999) was employed. `Nthcomp` provides a more accurate representation of the continuum shape resulting from thermal comptonization compared to the commonly used exponentially cutoff power law for describing non-thermal emissions.

To account for interstellar absorption attributed to neutral hydrogen, the `Tbabs` model (J. Wilms et al., 2000) was incorporated as a multiplicative component. The `Tbabs` model was held constant at a value of 1.3, derived from the HI4PI survey (Ben Bekhti et al., 2016). Similar to the previous power-law fit of *Nu*STAR data, the `CONSTANT` model was included to accommodate cross-instrument calibration differences. The constant parameter was fixed at 1 for PFMA while allowing FPMB to vary freely.

4.2.3.1 Reflection modelling

The last feature to be modelled involves the reflection component (i.e. the Fe Kα lines and Compton hump), for which the RELXILL model is employed (Dauser, J. García, et al., 2014; J. García, Dauser, et al., 2014). RELXILL is a relativistic reflection model designed to compute the reflection emission originating from the innermost regions of accretion disks around black holes, neutron stars, and AGN using a combination of the ionized reflection model XILLVER and the relativistic blurring kernel RELLINE.

RELXILL comprises a family of models distinguished by their assumptions regarding the primary source. Firstly, there are varied approaches to implementing the irradiation of the accretion disk by the primary source which is defined by the emissivity, representing the radially dependent flux irradiating the disk from the source. It can take the form of either an empirical power law or a lamp-post geometry. The empirical power-law implementation avoids assuming a specific geometry or physical location for the primary source. Instead, it simply posits that the emissivity depends on the radius as a broken power law, with the break occurring at the radius R_{br}. The lamp-post implementation assumes a simple geometry where the primary source is point-like and located on the rotational axis of the black hole. This source is characterized by its height above the centre of the black hole and potentially its velocity along this axis (see Dauser, Garcìa, et al. (2013) for more detail on the lamp-post geometry and its implementation in RELXILL).

Secondly, the spectral shape of the primary source's spectrum directly impacts the intrinsic reflection calculations performed by XILLVER. The primary spectrum itself can manifest as a simple power law with a high-energy cutoff, a thermal Comptonized continuum (nthcomp), or a blackbody spectrum. In this specific study, the RELXILL model RelxillCp is employed. This model utilizes an empirical power law for emissivity and nthcomp as the primary spectrum. While RELXILL can model both direct and reflected emissions, this study confines its use to modelling the reflection component exclusively. Other flavours of RELXILL include the Rellxilllp, which assumes a lamp-post spectrum and an empirical power-law emissivity, and RelxilllpCp, which uses a lamp-post and a thermally comptonized continuum emissivity approach.

Parameters	Epoch				
	1	**2**	**3**	**4**	**5**
$\mathbf{T_{in}}$ **(keV)**	$0.71^{+0.02}_{-0.03}$	$0.70^{+0.01}_{-0.02}$	$0.71^{+0.01}_{-0.03}$	$0.71^{+0.02}_{-0.03}$	$0.76^{+0.03}_{-0.02}$
Γ	1.57±0.01	$1.574^{+0.002}_{-0.001}$	$1.588^{+0.008}_{-0.006}$	$1.604^{+0.005}_{-0.003}$	$1.629^{+0.003}_{-0.004}$
θ (°)	$45.40^{+2.53}_{-2.83}$	$35.12^{+2.04}_{-1.52}$	$43.49^{+2.11}_{-1.62}$	$42.85^{+3.04}_{-3.32}$	$50.55^{+3.84}_{-2.63}$
$\mathbf{R_{in}}$ **(ISCO)**	$2.615^{+0.33}_{-0.29}$	$1.74^{+0.27}_{-0.10}$	$2.68^{+0.35}_{-0.32}$	$1.96^{+0.57}_{-0.53}$	$2.05^{+0.21}_{-0.25}$
log ξ **(erg cm** $\mathbf{s^{-1}}$**)**	$3.22^{+0.08}_{-0.04}$	3.37 ± 0.03	$3.23^{+0.06}_{-0.05}$	$3.35^{+0.06}_{-0.08}$	$3.40^{+0.03}_{-0.06}$
kT (keV)	$24.70^{+1.21}_{-1.03}$	$23.46^{+0.24}_{-0.23}$	$27.41^{+2.16}_{-0.96}$	$27.96^{+1.65}_{-0.76}$	$31.35^{+1.15}_{-0.84}$
χ^2**/d.o.f**	559.18/478=1.17	641.95/581=1.10	880.09/737=1.19	779.99/642=1.21	646.54/612=1.06
Parameters	**Epoch**				
	6	**7**	**8**	**10**	**11**
$\mathbf{T_{in}}$ **(keV)**	$0.74^{+0.08}_{-0.04}$	$0.70^{+0.03}_{-0.04}$	$0.80^{+0.02}_{-0.09}$	0.781±0.001	0.757±0.001
Γ	$1.652^{+0.003}_{-0.006}$	1.65±0.01	$1.61^{+0.012}_{-0.002}$	$1.93^{+0.003}_{-0.01}$	$1.95^{+0.008}_{-0.003}$
θ (°)	$62.81^{+1.82}_{-3.54}$	$47.14^{+1.99}_{-2.75}$	$60.49^{+2.45}_{-3.84}$	$69.88^{+1.56}_{-8.87}$	$73.48^{+0.62}_{-1.45}$
$\mathbf{R_{in}}$ **(ISCO)**	$1.50^{+0.11}_{-0.07}$	$1.55^{+0.52}_{-0.24}$	$1.53^{+0.13}_{-0.14}$	$2.22^{+3.01}_{-0.35}$	$2.39^{+0.1}_{-0.01}$
log ξ **(erg cm** $\mathbf{s^{-1}}$**)**	3.22 ± 0.07	$3.31^{+0.07}_{-0.05}$	$3.05^{+0.35}_{-0.05}$	$3.16^{+0.04}_{-0.03}$	$3.16^{+0.11}_{-0.06}$
kT (keV)	$38.47^{+1.72}_{-3.68}$	$36.21^{+2.16}_{-1.31}$	$35.84^{+10.74}_{-1.51}$	[1000.0]	[1000.0]
χ^2**/d.o.f**	784.95/778=1.01	616.38/518/1.90	857.99/724=1.19	900.12/764=1.18	554.97/399=1.40

Table 2: Parameters of fits to *Nu*STAR and *Swift*-XRT spectra of MAXI J1820+070. The model is CONSTANT $*$ (TBABS(DISKBB + NTHCOMP + RELXILLCP). Errors represent 90% confidence intervals.

4.2.3.2 Joint spectral fitting with *Swift*-XRT

*Nu*STAR was simultaneously fit with *Swift*-XRT with observations that were performed within 12 hours of each other. Example simultaneously-fit spectra in the hard and soft states are shown in Figure 25, highlighting the clear dominance of the thermal component ('`diskbb`' in blue) in the soft state and the non-thermal component ('`nthcomp`' in cyan) in the hard state. Additionally, the reflection component ('Relxillcp' in magenta) depicts a prominent Compton-hump above $\sim$ 20 keV and a Fe K line profile.

The fit results of the key parameters with 90% confidence uncertainties are tabulated in Table 2. The evolution of these parameters is plotted as a function of time in Figures 27 and 28. Notably, there exists a strong degeneracy between the dimensionless spin parameter a^* and the inner-disk radius $\mathtt{R_{in}}$ as the true value of $\mathtt{R_{in}}$ is governed by a^* and the disk inclination. Using epoch 6 as an example, when the spin parameter is frozen at its maximum (0.998) the fit statistic χ^2/d.o.f is 784.95/778=1.01. When $\mathtt{R_{in}}$ is frozen at the ISCO and a^* is allowed to vary, the spin parameter continues to settle near the maximum value with a χ^2/d.o.f of 930.83/778=1.20. This result suggests that MAXI J1820+070 favours a system with a truncated accretion disk over a lower spin. These findings are supported by the research of Bharali et al. (2019).

It is essential to highlight that all fits necessitated the inclusion of a narrow Gaussian absorption component (`Gabs` in Xspec), with a centre around $\sim 6.9-7.3$ keV. This component shifts towards higher energies as the outburst progresses. In the soft state, an additional absorption feature is needed, located at approximately 4 keV. The residuals of the spectral fit in epoch 5 are illustrated in Figure 26. The inclusion of `Gabs` yields a slightly improved fit statistic (1.06), compared to the fit without it (1.09). Furthermore, a visual comparison of the residuals in Figures 26b and 26a reveals the presence of a residual feature between $\sim 6-9$ keV in the fit without the addition of `Gabs`.

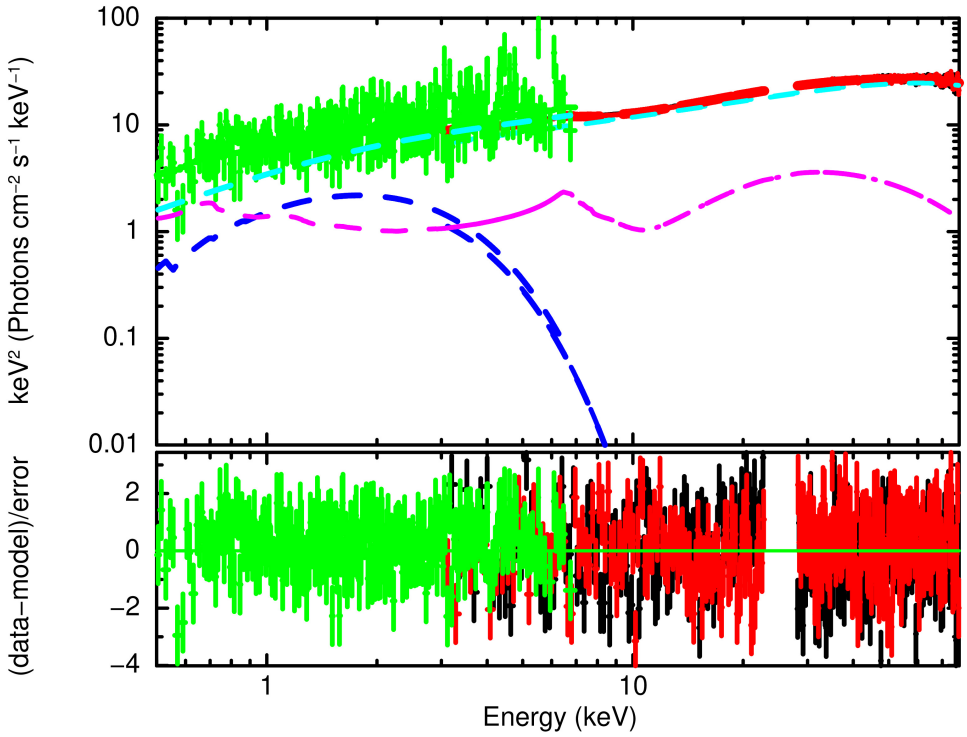

(a)

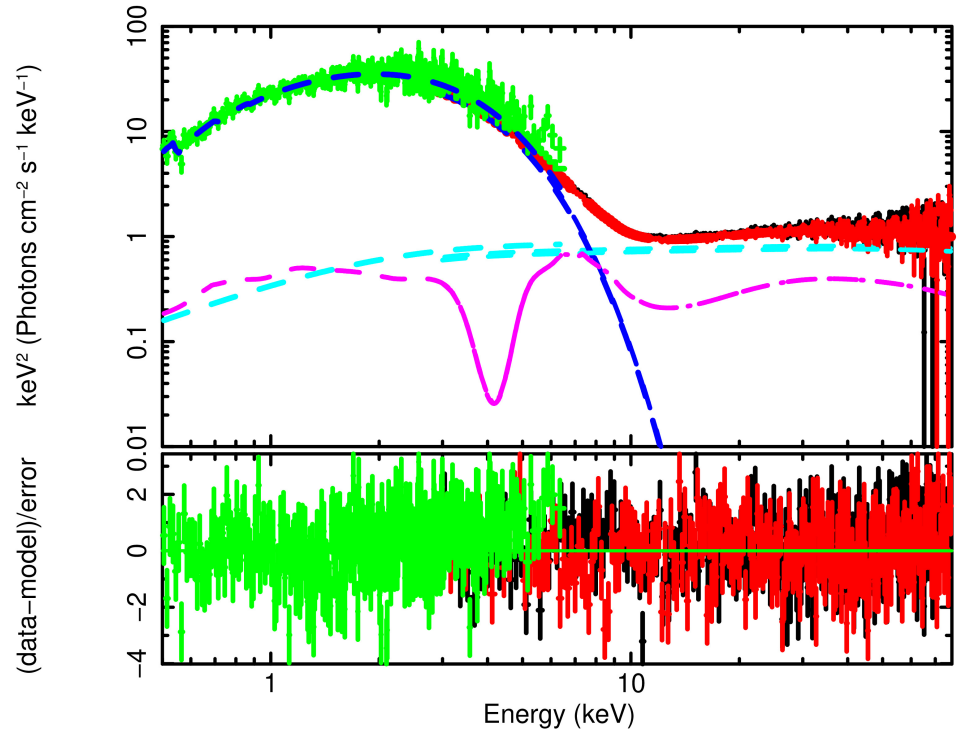

(b)

Figure 25: The hard and soft state simultaneously fit spectra of MAXI J1820+070 with *Nu*STAR and *Swift*-XRT. **(a)**: The hard state spectrum (epoch 3) with residuals in the lower panel. The black and red data points represent the two FPMs of *Nu*STAR while the *Swift*-XRT data is represented in green. The main components of the model are `Diskbb` (blue), `Nthcomp` (cyan) and `RelxillCp` (magenta). **(b)**: The soft state spectrum (epoch 10) following the same conventions as (a).

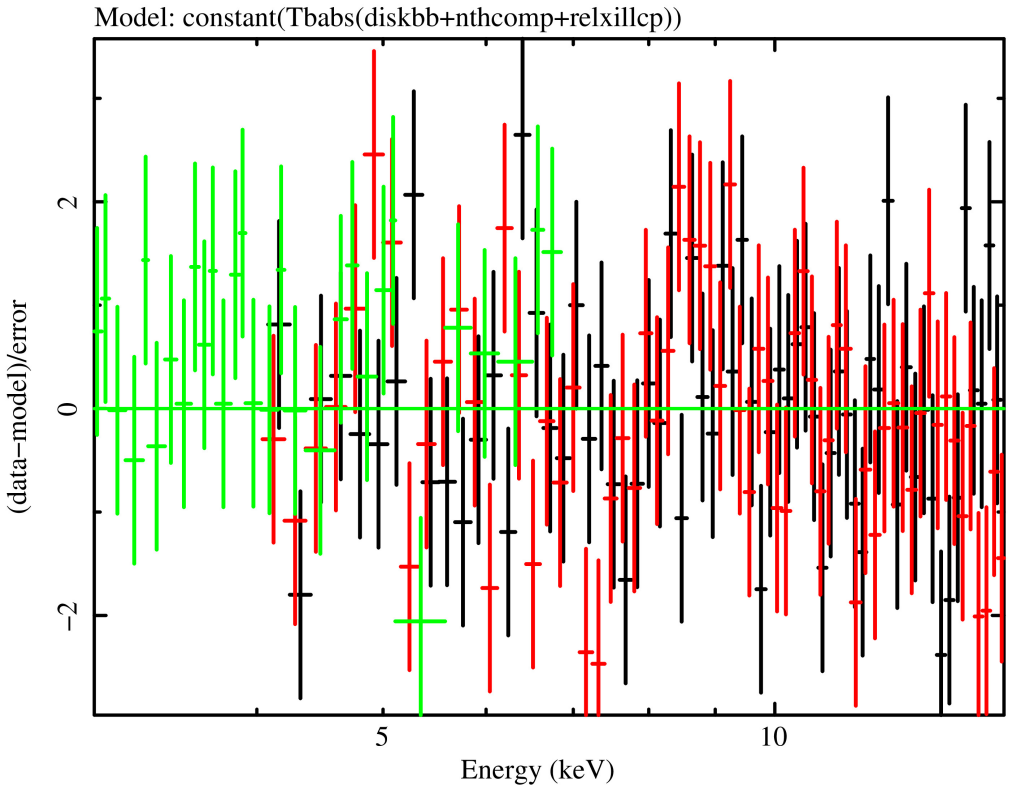

(a) χ^2/d.o.f = 1.09

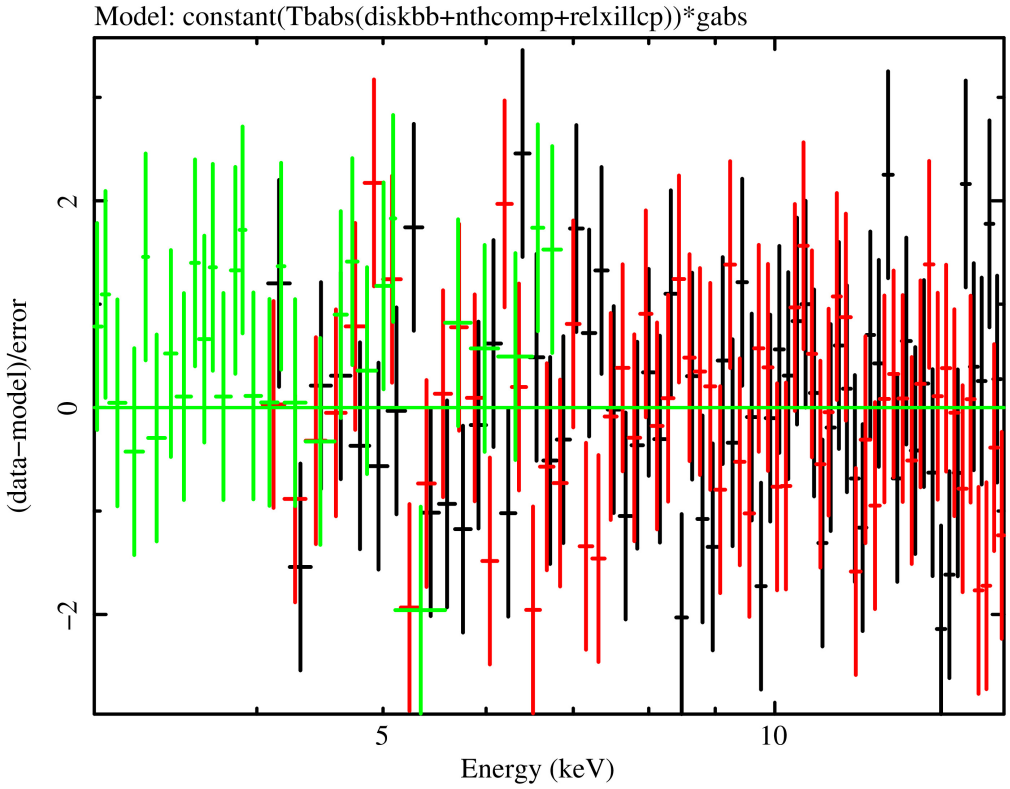

(b) χ^2/d.o.f = 1.06

Figure 26: The fit residuals of *Nu*STAR and *Swift*-XRT spectra in epoch 5. (a) Represents the fit with the addition of the Gabs model and (b) without Gabs.

4.2.4 Parameter evolution

In the hard state, the inner disk temperature ($T_{\rm in}$) of MAXI J1820+070, as depicted in the top plot of Fig. 27, remains relatively constant before undergoing a gradual increase. During the state transition, a notable temperature spike becomes evident, reaching approximately 0.8 keV, followed by a gradual decline. This increase in temperature is indicative of the soft state, signalling the prevalence of thermal emission. The inner disk radius ($R_{\rm in}$), illustrated in the middle plot of Fig. 27, appears to gradually extend toward the ISCO as the system shifts into the soft state, $R_{\rm in}$ once again moves away from the black hole. However, it is important to note that the apparent change in the inner disk radius is not substantial enough to provide evidence of disk truncation.

The lower plot in Fig. 27 illustrates the variability in disk inclination, with 0° representing a face-on orientation and 90° indicating an edge-on orientation. The inclination of a BHB is typically assumed to be static unless the disk warping is present (Wijers and Pringle, 1999). However, the true inclination of MAXI J1820+070 is not well-established in the literature (see §5.5 for more details). Therefore, the inclination parameter is set as a free parameter. From analysis of the plot, it is evident that the model prefers a lower inclination in the early phases, with an increasing inclination as the source begins to transition to the soft state. It is worth noting that the variation in inclination is most likely not due to physical factors, but rather a result of the model's inability to accurately describe the system.

The characteristic photon index, presented in the top plot of Fig. 28, undergoes a gradual increase during the hard state, briefly dipping at the onset of the state transition before experiencing a sudden surge in the soft state. Caution is warranted when interpreting the photon index in the soft state, as the diminished dominance of the non-thermal spectrum presents challenges in characterising the non-thermal emitting region and necessitates a nuanced analysis. Throughout the hard state, the temperature of the Comptonizing electrons in the corona, as depicted in the bottom plot of Fig. 28, steadily rises, plateauing just before the state transition. In the soft state, the electron temperature becomes pegged at a maximum of 1000 keV. This increase can again be attributed to the diminishing intensity of non-thermal emission, introducing challenges in accurately characterizing this parameter during the soft state. Consequently, the electron temperature was fixed for this period when performing spectral fits.

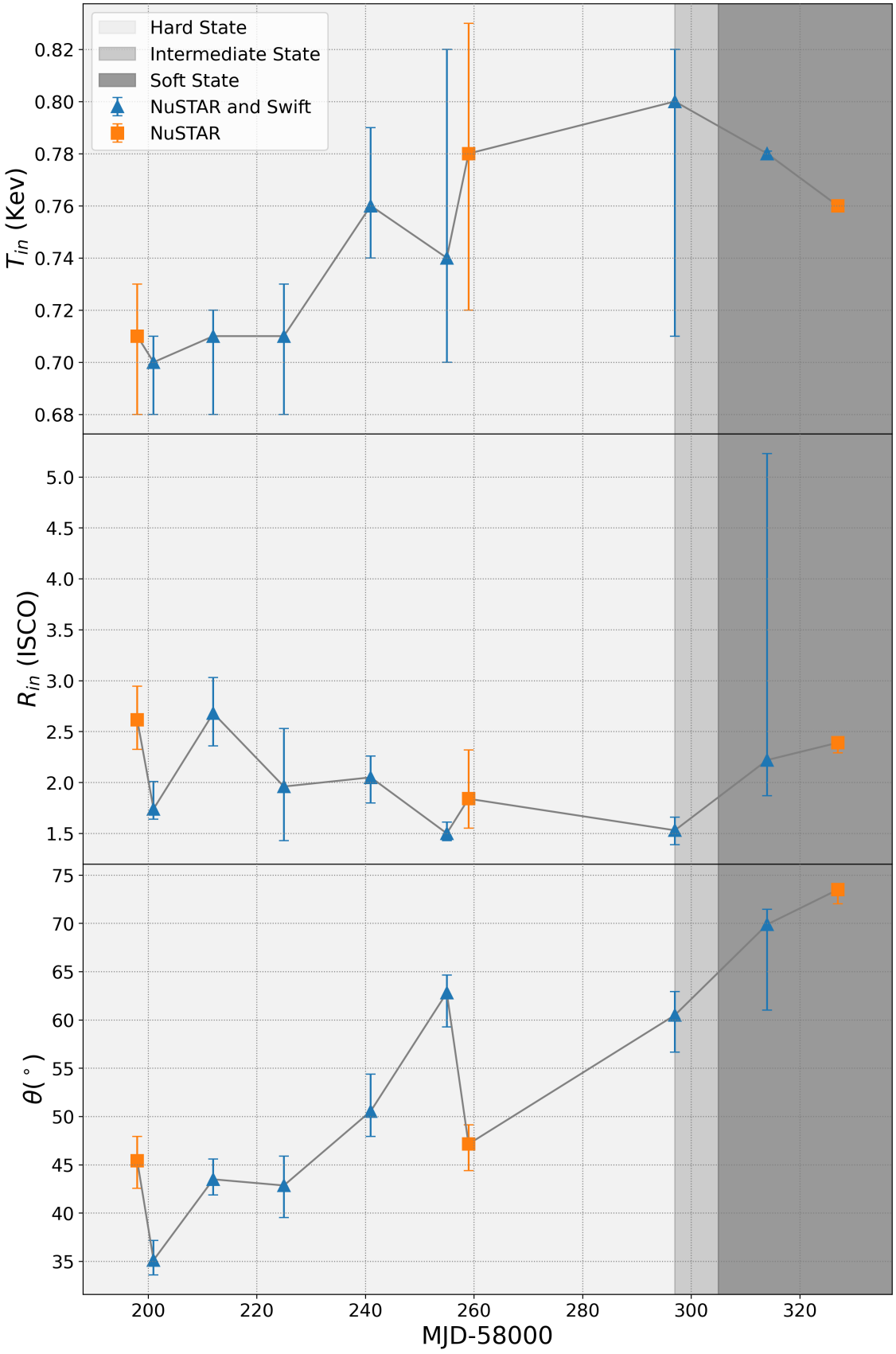

Figure 27: Plot of key spectral fit parameters of the disk against time. **Top**: Plot of the inner disk temperature. **Middle**: Plot of the inner disk radius. **Bottom**: Plot of the disk inclination.

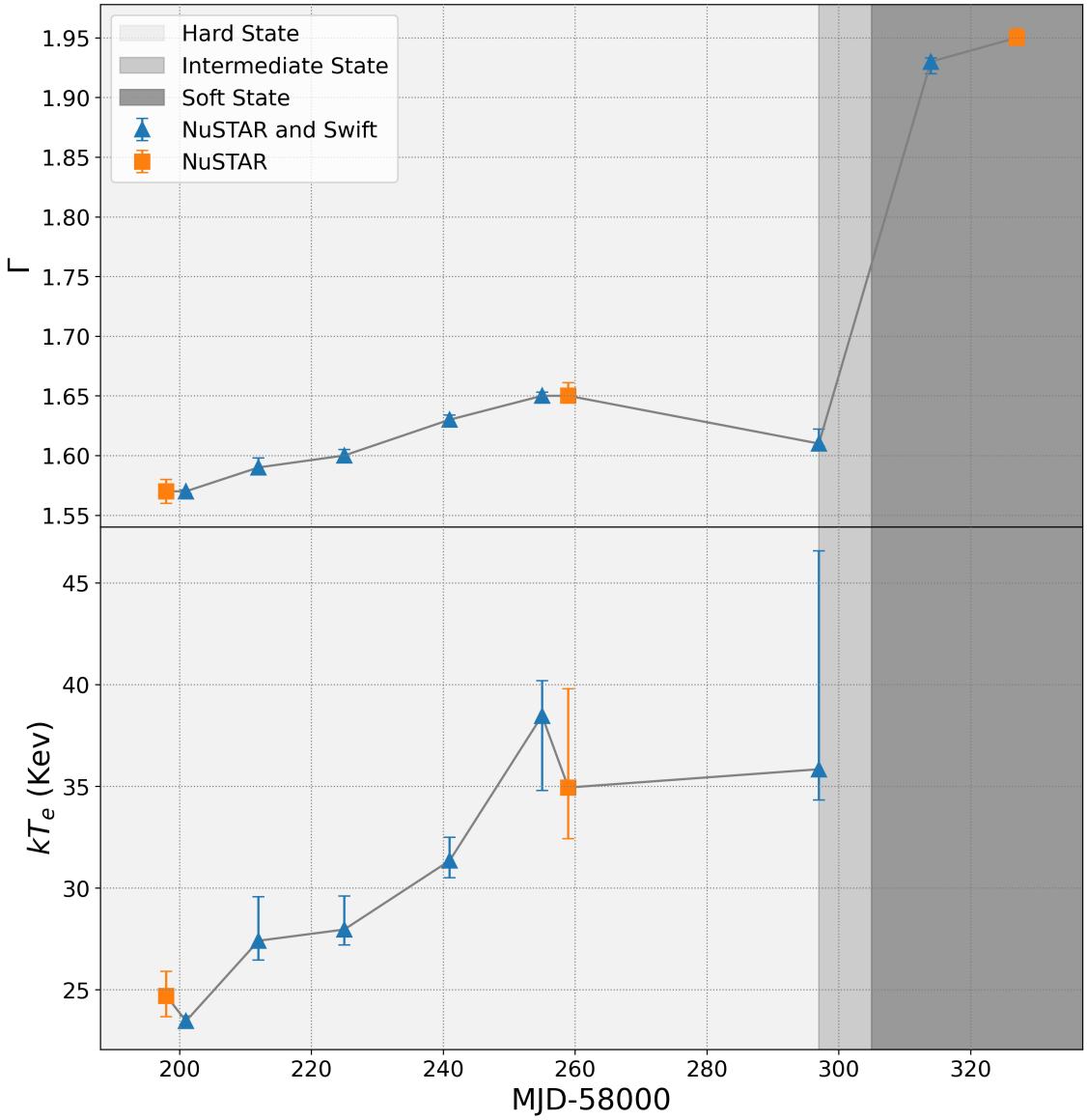

Figure 28: Plot of key spectral fit parameters of the corona against time. **Top**: Plot of the photon index. **Bottom**: Plot of the electron temperature of the corona

4.3 Temporal evolution

4.3.1 QPO analysis

The temporal variability of MAXI J1820+070 was investigated by analyzing its PDS, lag-frequency and lag-energy evolution, computed using the PYTHON package 'Stingray' version 1.1.2.4. Stingray is a versatile software package tailored for the analysis of astrophysical X-ray and related data. It unifies prior python-based spectral-timing efforts, adhering to modern open-source standards inspired by astropy. Key features of Stingray include a comprehensive library of time series methods for power spectra, cross spectra, covariance spectra, and lags. While established software exists for X-ray spectral fitting, X-ray timing has traditionally relied on custom software. Stingray fills this void and incorporates state-of-the-art spectral timing techniques from the scientific literature. Its primary goal is to make advanced spectral timing techniques accessible to the research community while maintaining statistical rigour.

Initially, the event files from *Nu*STAR and *NICER* undergo GTI filtering, followed by generating periodograms using 512-second light curve segments with 0.01-second bins. Due to *Nu*STAR's production of two event files from the FPMA and FPMB focal plane modules, we choose to create a cospectrum instead of a PDS. This decision is made to address the impact of dead time-induced noise at higher frequencies. The cospectrum method considers the phase and amplitude relationship between signals from both detectors, aiming to create a more uniform periodogram at higher frequencies. Similarly, for *NICER*, periodograms are created using 200-second light curve segments with 0.001-second bins. These periodograms are averaged to create a PDS. In both cases, the PDSs are rebinned to 0.02-second intervals for improved clarity.

The cospectra representing the complete calibrated *Nu*STAR energy band (3-79 keV) is depicted in Figure 29. This Figure illustrates the presence and evolution of QPOs observed during the hard state, persisting until the onset of the source's transition towards the soft state. Each subsequent PDS has been vertically offset by a factor of 10. When MAXI J1820+070 transitions into the soft state, QPOs are no longer visible, as evident from the soft state PDS in Figure 30. Qualitative analysis reveals a shift in the peak QPO frequency towards higher frequencies throughout the outburst duration, except for the final observation coinciding with the commencement of the intermediate state. Additionally, a second harmonic QPO is observable, albeit marginal during the early stages of the outburst.

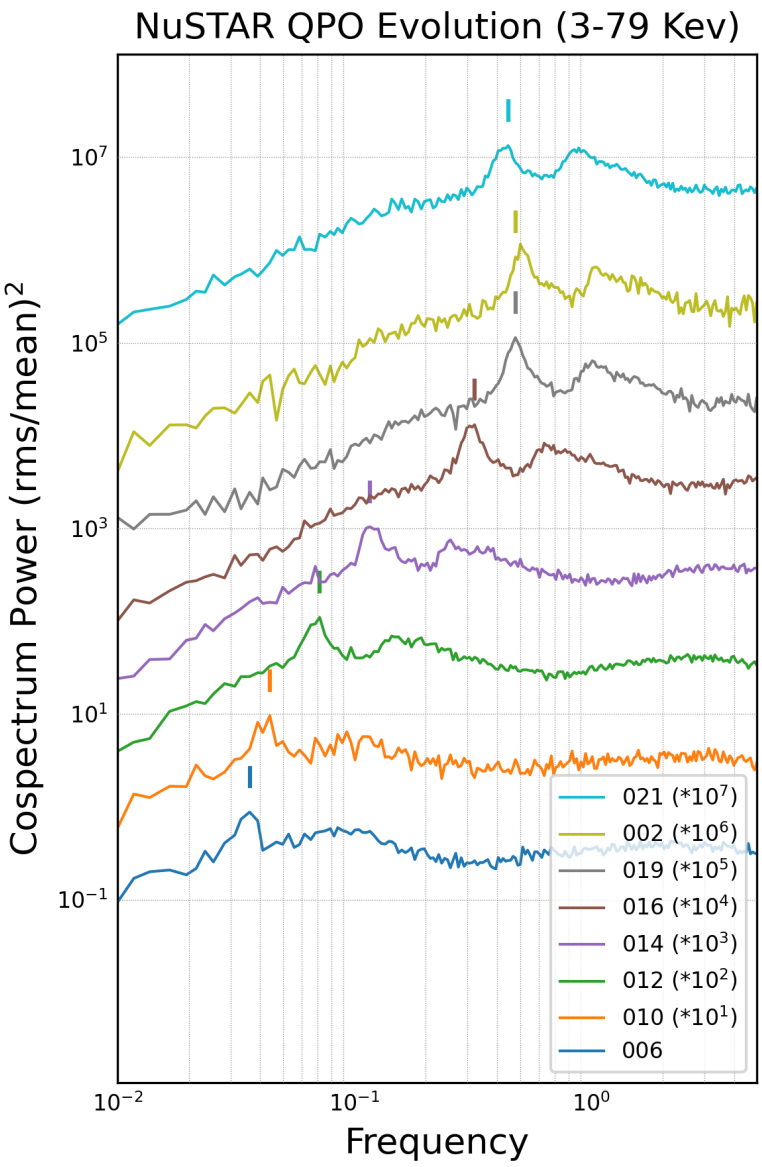

Figure 29: PDS of MAXI J1820+070 using *Nu*STAR data with Leahy normalization (Leahy et al., 1983). Subsequent PSDs are displayed with a 10x vertical offset. Each PSD has been logarithmically rebinned to 0.02 for enhanced clarity. The vertical bars above each PDS delineate the peak frequency position of each QPO. Each observation is labelled by the last three digits of their observation ID.

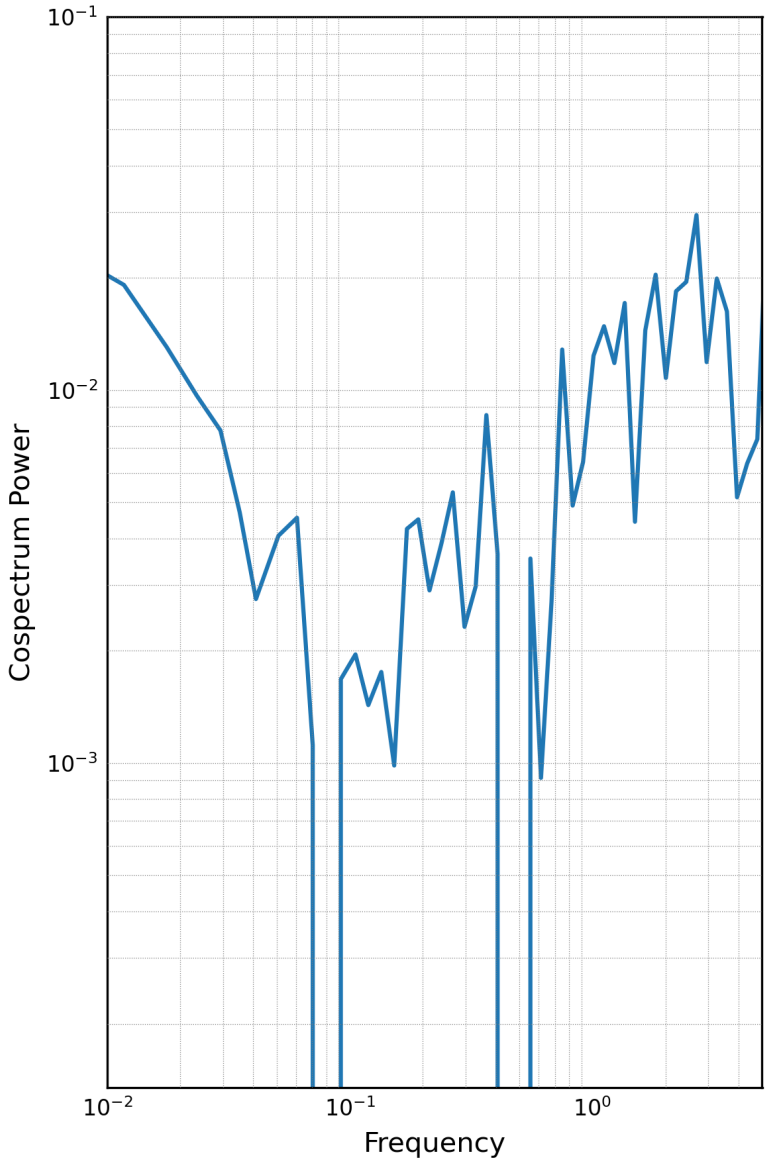

Figure 30: PDS of a *Nu*STAR observation of MAXI J1820+070 in the soft state (MJD 58306).

To investigate the energy-dependent variability, the cospectrum of the *Nu*STAR observations is split into two energy bands: 3-10 keV and 10-79 keV, displayed in Figure 31. Similar to the previous Figure, consecutive QPOs are offset by a factor of 10. Qualitative analysis indicates a concentration of most QPO power within the 3-10 keV range. Within this range, the PDS exhibits only a slight power reduction, while the QPO structure appears relatively unaffected. In the 10-79 keV range, a notable decrease in power is observed, with QPOs being substantially less prominent and only marginally visible during the later stages.

To explore the energy dependence within softer ranges below 3 keV, the *NICER* PDS was computed within the 0.2-3.0 keV energy range. For comparison with *Nu*STAR, the *NICER* PDS was also computed in the 3.0-10.0 keV energy band. The respective PDSs are displayed in Figure 32. Each PDS is vertically offset by a factor of 5, except for the final one, which is offset by 25 in both plots. The *NICER* observations

1200120[106-189] are aligned with the *Nu*STAR observations 90401309[006-021], as detailed in Table 1. A qualitative assessment comparing the 0.2-3.0 keV PDS to the 3-10 keV and 10-79 keV ranges confirms that the QPO power predominantly resides in the 3-10 keV energy range during the early stages of the hard state. However, the QPOs can be observed in the 0.2-3.0 keV range with the onset of the intermediate state, particularly during observations 1200120[190-196]. Notably, during these observations in the intermediate state, it becomes apparent that the peak frequency of the QPOs continues to shift towards higher energies, following an initial shift towards lower energies observed during the onset of the intermediate state, as depicted in the *Nu*STAR observations 90401309021 in Fig. 29. Unlike the *Nu*STAR PDSs within the energy range above 3 keV, which consistently displayed a stronger fundamental QPO, most observations within the 0.2-3.0 keV range exhibit a more pronounced second harmonic (the higher-frequency QPO). This consistent trend is evident across all observations, except for the final one illustrated in Figure 32. Upon visual comparison of the RMS power of the broadband noise on which the QPOs are superimposed, it is apparent that the noise is more intense at lower energies, gradually decreasing in strength from 0.2-3.0 keV to 3-10 keV to 10-79 keV.

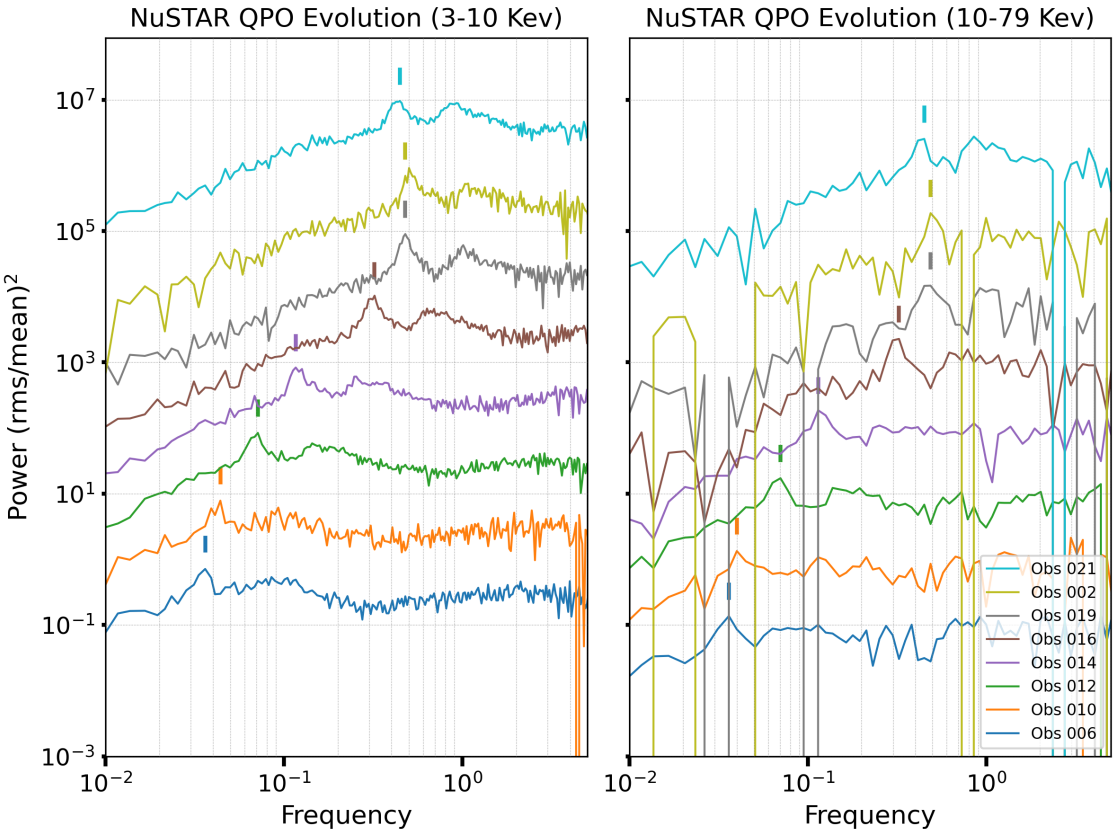

Figure 31: *Nu*STAR QPO evolution in two X-ray energy bands: 3-10 keV (left) and 10-79 keV (right). This Figure follows the same conventions from Figure 29

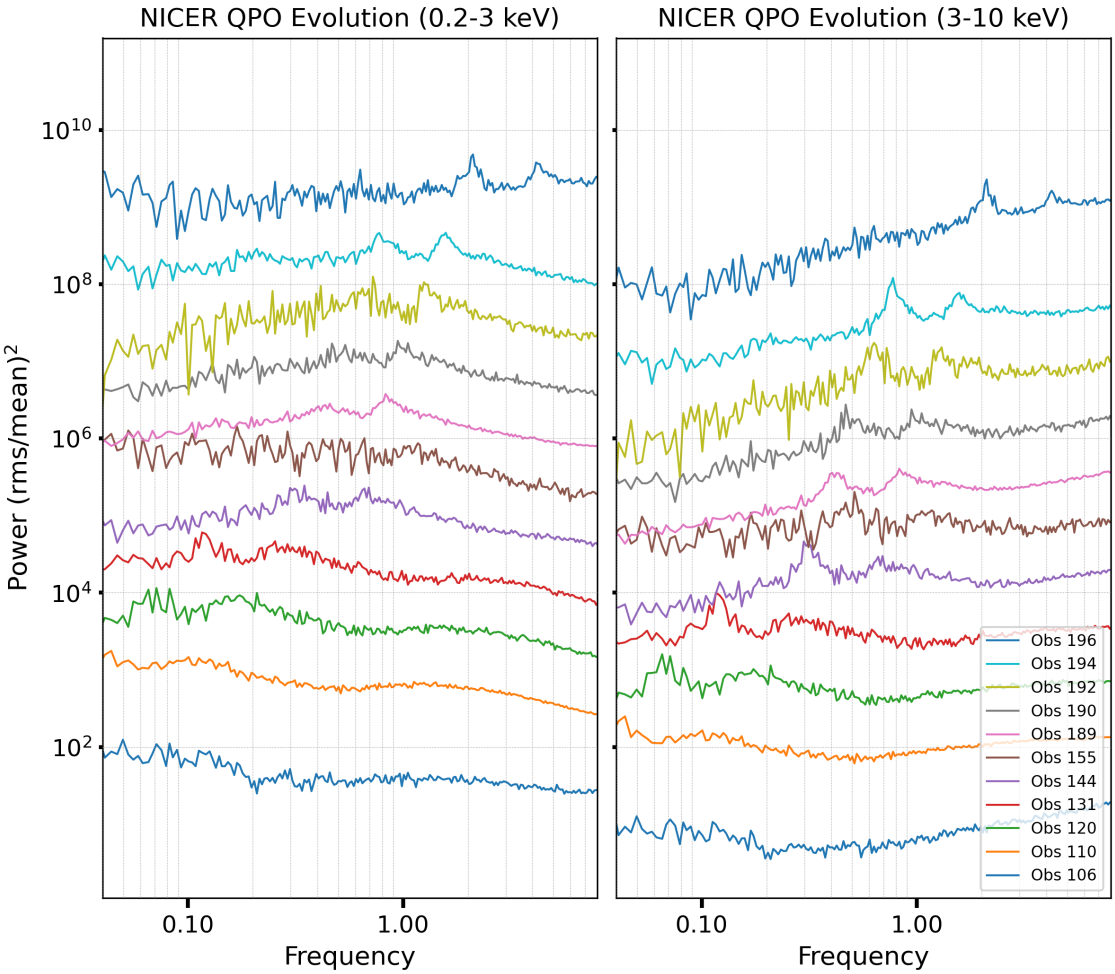

Figure 32: NICER QPO evolution in two X-ray energy bands: 0.2-3.0 keV (left) and 3.0-10.0 keV (right). Subsequent PSDs are displayed with a 5x vertical offset. Each observation is labelled by the last three digits of their observation ID.

To quantitatively analyze the evolution of QPOs across the entire *Nu*STAR energy range, the PYTHON library '**lmfit**' was utilized. This library specializes in non-linear least-squares minimization and curve fitting. The analysis involved fitting the QPOs observed in *Nu*STAR dataset 90401309[006-021] using a model that consists of a combination of 3 or 4 Lorentzian curves with the least-squares fit method. Figure 33 presents a visual representation of the fitting results for *Nu*STAR observation 90401309021, where two Lorentzians were employed to model the QPO and its second harmonic, while a third Lorentzian was used to characterize the broad-band noise component.

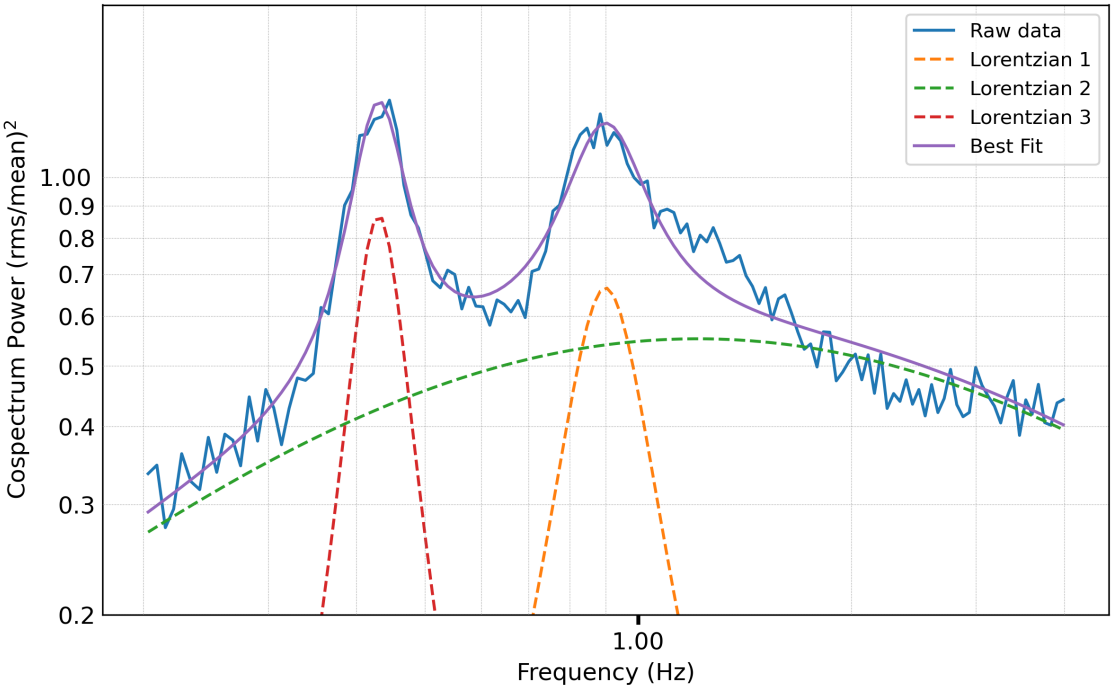

Figure 33: Example best fit plot of the QPOs observed in *Nu*STAR data (ObsID 021). The blue line corresponds to the raw data, while the purple line signifies the best fit. The red, orange, and green Lorentzians correspond to the fundamental QPO, second harmonic QPO, and broadband noise components, respectively

To estimate the uncertainty of the peak frequency and FWHM of the QPO Lorentzians, the '**emcee**' package in the '**lmfit**' library was utilized to perform Monte Carlo Markov Chain (MCMC) sampling. This process involved computing the posterior probability distribution of the model parameters, based on the maximum likelihood solutions obtained from the least squares fit. Employing a chain length of 10,000 for all observations in the MCMC sampling, with 100 walkers and a burn-in length of 2,000, the success of the method was assessed by plotting the acceptance fraction. An example plot is shown in Figure 34. Typically, an acceptable acceptance fraction falls within the range of 0.2 to 0.5. The visualization of the posterior probability distribution is presented in Figure 35. The resulting posterior probability distribution was then used to estimate the 1-σ errors associated with the parameter estimates.

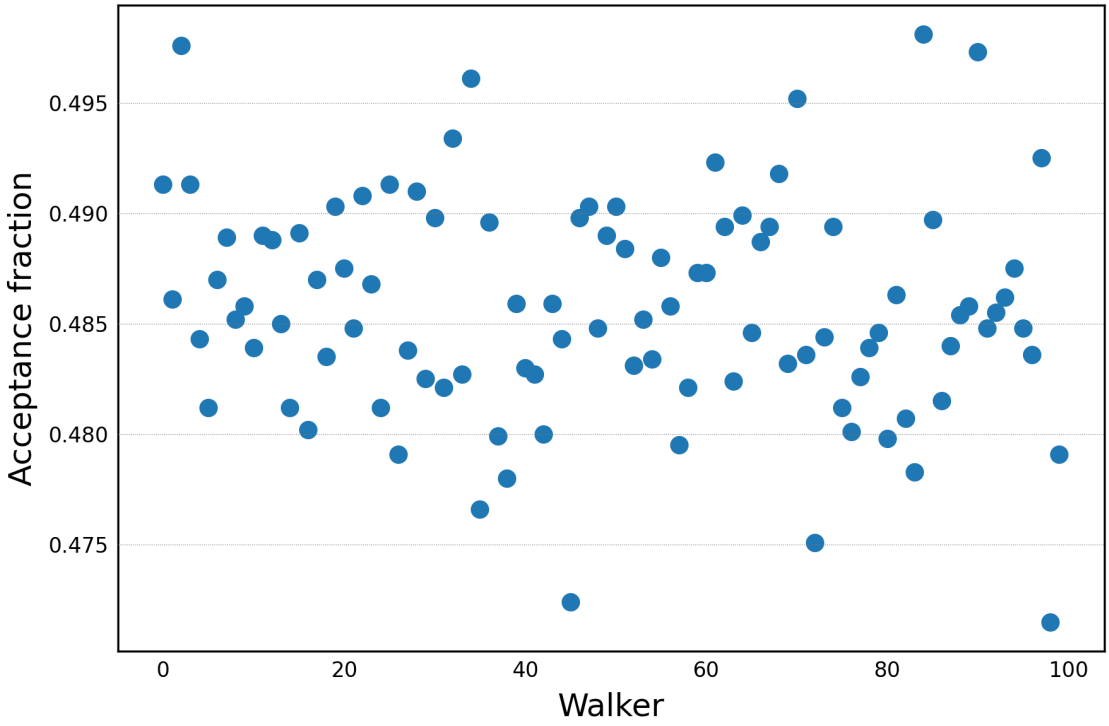

Figure 34: Plot of the acceptance fraction per walker during the MCMC sampling the *Nu*STAR observation 90401309021 fit.

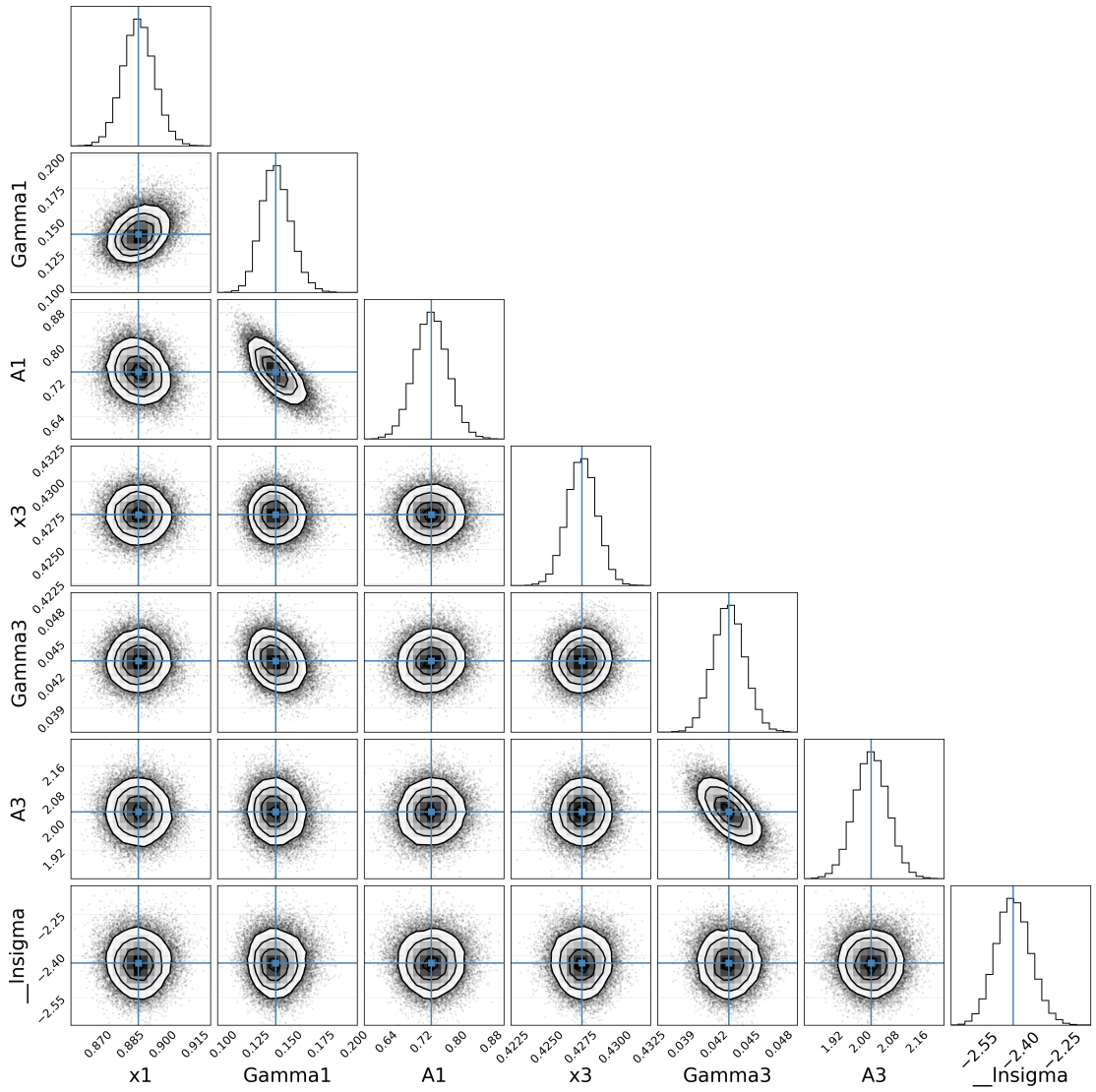

Figure 35: Visualization of the posterior probability distribution, calculated using MCMC sampling. The parameters x1/3, Gamma1/3 and A1/3 correspond to the peak frequency position of the QPO, half of the FWHM and the amplitude respectively. The 'lnsgima' variable is added automatically to estimate the uncertainty when the data is not weighted.

The process outlined above was employed for each observation in Fig. 29. The resulting best-fit solutions of the QPO peak frequency and FWHM were then used to calculate the quality factor (Q), with errors being propagated accordingly. The evolution of the QPO peak frequency, FWHM and quality factor is displayed in Figure 36. The best-fit solutions validate the earlier qualitative analysis, revealing a discernible trend: the QPO steadily transitions to higher frequencies throughout the outburst, concurrently becoming more prominent, as evidenced by the increasing Q factor. Subsequently, upon the onset of the intermediate state, both the frequency and Q factor exhibit a decline.

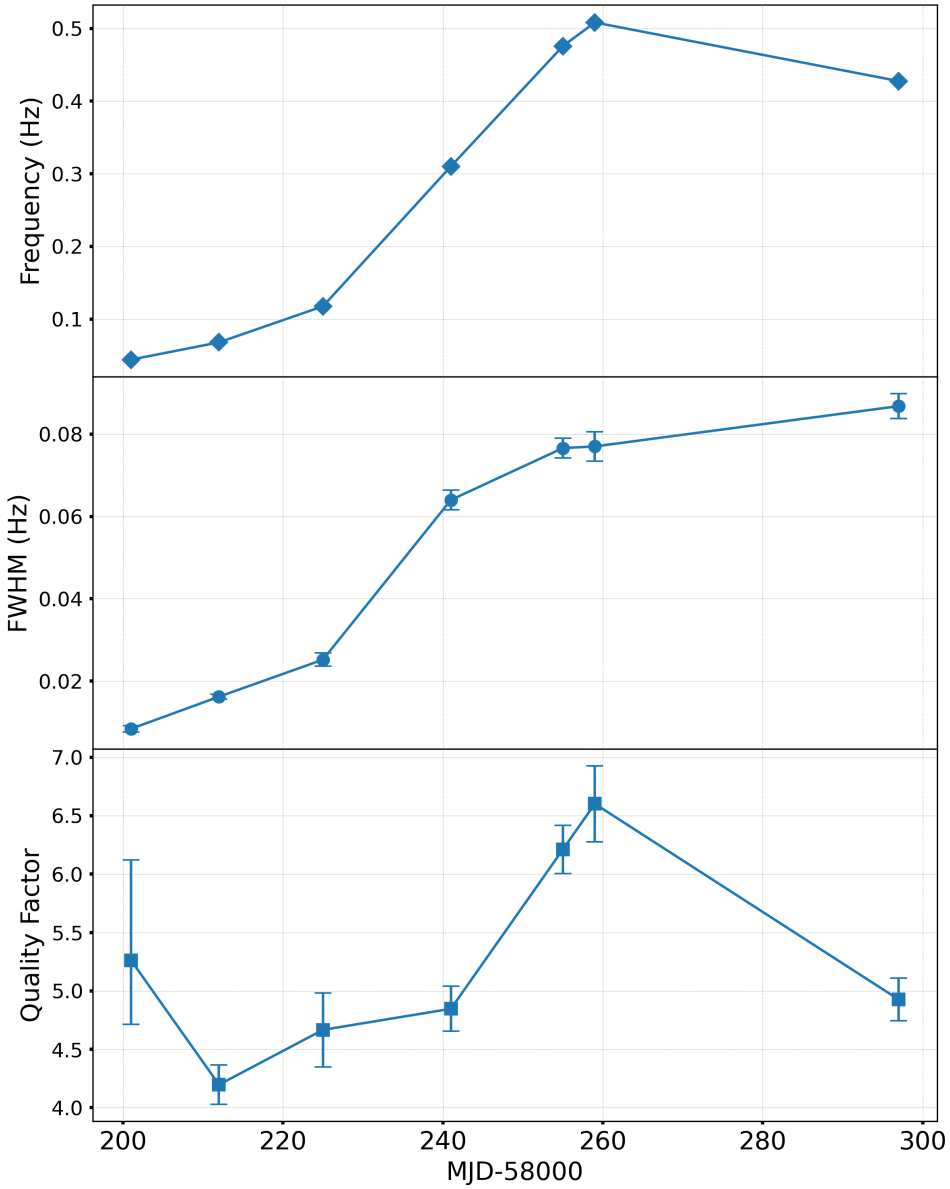

Figure 36: Time evolution of the fundamental QPO parameters. Top: The centroid frequency of the QPO. Middle: the FWHM of the QPO. Bottom: The quality factor (Q) of the QPO.

4.3.2 Lag-frequency analysis

For additional timing analysis, Stingray was employed to compute the time lag between two hard and soft energy bands across a range of frequencies. Stingray utilizes standard Fourier techniques to derive the time lag. The process begins by segmenting the light curves within each energy band into equal segments, with a user-defined length. Subsequently, the cross-spectrum between each pair of energy bands is calculated for every segment. This cross-spectrum contains information about the coherence and phase difference between the two energy bands at each frequency. Following this, the cross spectra are averaged across all segments to derive the overall averaged cross-spectrum. To determine the time-lag, Stingray employs the phase difference (ϕ) and the phase-time relationship: $\tau = \frac{\phi}{2\pi\nu}$, where τ represents the time lag in seconds, and ν denotes the centre of the frequency bins.

Following the conventions outlined by Wang, Mastroserio, et al. (2021), Marco, A. A. Zdziarski, et al. (2021), and E. Kara, J. F. Steiner, et al. (2019), the computation of time lag in this study is based on *NICER* spectra between two energy bands: 0.5-1.5 keV and 1.5-3.0 keV. The resulting lag-frequency plots for epochs 1-5 and 7-9 are presented in Figure 37. The four observations in the IMS (epoch 9) have been averaged for clarity. Analysis of these plots reveals a hard lag (positive lag) at lower frequencies with soft lag (negative lag) present at higher frequencies across all observations. Low-frequency hard lags, where the hard X-rays lag behind the soft X-rays, are seen in most Galactic BHBs in the hard or intermediate spectral states (Miyamoto and Kitamoto, 1989; Altamirano and Méndez, 2015). These lags are usually explained by fluctuations in the mass accretion rate in the disk, which travel inwards on the viscous timescale and cause the emission of soft photons earlier than hard photons (Kotov et al., 2001). The high-frequency soft lag, also known as the reverberation lag, is believed to be caused by the delay in light travel time between the direct X-ray emission from the corona and the reflected emission off the inner accretion disk. This phenomenon has been detected in both AGN and BHBs in the form of soft excess emission and Fe K emission lines lagging behind the hard X-ray band (A. C. Fabian, Zoghbi, et al., 2009; E. Kara, Alston, et al., 2016; De Marco et al., 2017).

During the hard state, a notable pattern emerges: the amplitude of the soft reverberation lag steadily decreases, accompanied by a discernible shift in the frequency range where soft lag is detected towards higher frequencies. During the state transition (epoch 9), there is a sudden increase in the reverberation lag, and concurrently, the frequency range shifts towards lower frequencies. This trend suggests a dynamic evolution in the geometric relationship between the corona and the disk throughout the state transition.

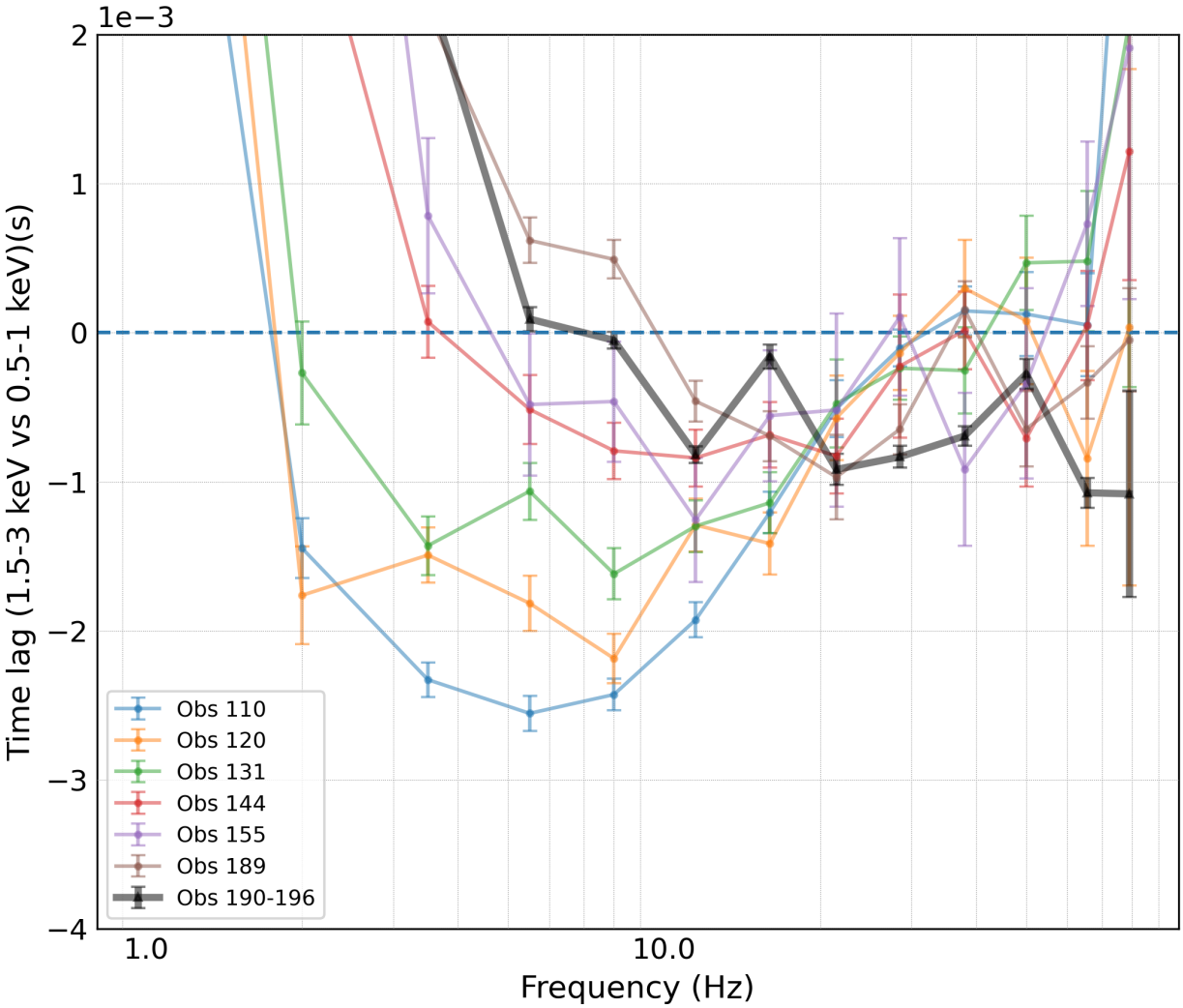

Figure 37: Time-lag vs frequency plot using *NICER* observations. For clarity, the four observations in the IMS (epoch 9) have been averaged, adopting a similar approach demonstrated by Wang, Mastroserio, et al. (2021).

5 Discussion

5.1 Light curve evolution and state transitions

The analysis of the light curve illustrated in Fig. 16, along with corroborating literature (Stiele and Kong, 2020), reveals four distinct outbursts. Initially, the source remained in the hard state during the first outburst, while the onset of the second outburst marked the transition to the soft state. Following these major outbursts, two subsequent, weaker outbursts occurred, during which MAXI J1820+070 maintained the hard state. These later outbursts have been referred to as a "re-brightening" and a "mini-outburst" (Arabacı et al., 2022). The initial pair of outbursts resembles a dual outburst event, akin to a similar occurrence observed in GX 339-4 in 2004 (Joinet et al., 2007; Plant et al., 2014).

5.2 QPO-disk connection

Our analysis of the time variability of MAXI J1820+070 reveals a dynamic evolution of the QPOs present in the PDSs in the hard state. The *Nu*STAR PDSs illustrated in Fig. 29 depict a QPO, along with a weaker harmonic, with centre frequencies shifting to higher energies during the hard state, subsequently shifting back to a lower frequency at the onset of the hard-to-soft state transition. The QPOs disappear after the state transition in the *Nu*STAR data as illustrated in Fig. 30. The evolution of the QPOs was further quantified by modelling the PDSs with a combination of Lorentzians, the results of which are plotted in Fig. 36.

Partitioning the PDSs into three distinct energy bands—0.2-3.0 keV, 3.0-10.0 keV, and 10-79 keV, as depicted in Figures 31 and 32 reveals that both the QPO and broadband noise power is concentrated within the 3.0-10.0 keV range. The QPOs are still present in the 0.2-3.0 keV range, albeit weaker but instead have stronger broadband noise. In the harder band (10-79 keV), we find that the QPOs effectively disappear. Earlier studies on other black-hole XRBs such as XTE J1859+226 and GRS 1915+105 suggest that the power of QPOs is concentrated mainly in the non-thermal emission (Casella et al., 2004; Cabanac et al., 2010). In particular, the finding of Cabanac et al. (2010) shows that while the power of the QPOs is mainly in the coronal/jet emission, their frequency variations are better correlated with the soft X-ray flux, suggesting that the accretion disk is a physical source of the QPOs. Fig. 16 in Casella et al. (2004) shows that the fractional RMS amplitude of the QPOs reaches a maximum above 20 keV where it plateaus. Our analysis of the PDS of MAXI J1820+070 challenges these findings, where we instead see the power concentrated in the 3.0-10.0 keV.

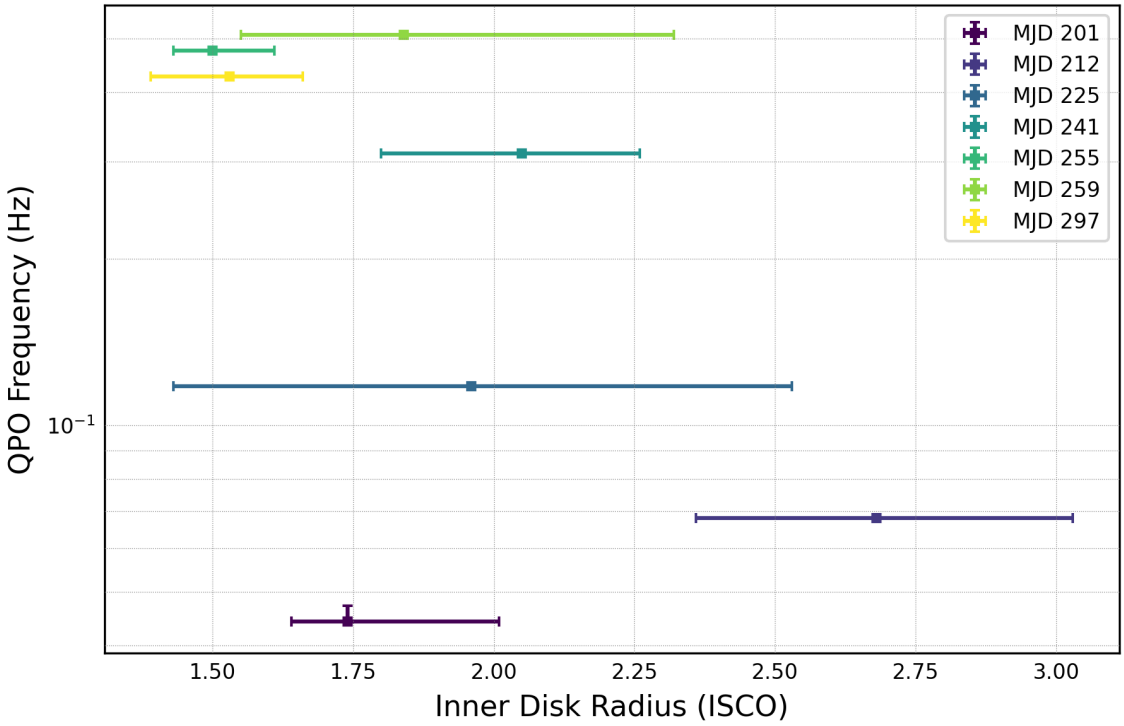

Figure 38: A comparison of the QPO centroid frequency evolution vs the inner disk radius parameter obtained from spectral fits. Each data point has been labelled based on its corresponding MJD date.

In Figure 38, the correlation between the centroid frequency of the QPOs and the inner disk radius is illustrated. The plot highlights a dynamic QPO frequency with minimal variation in the disk radius, suggesting that the QPO frequencies are not correlated with the geometry of the disk. These findings align with the investigations conducted by Buisson et al. (2019) on MAXI J1820+070. Their research indicates that the observed relationship between QPO frequency and inner disk radius diverges from the expected trends predicted by models such as Lense-Thirring precession. Instead, they propose a connection to the temporal evolution of the corona.

5.3 Shrinking Corona

The lag-frequency spectra analysis, displayed in Fig. 37, reveals a dynamic relationship between the soft and hard photons. In the hard state, there is a clear trend where the frequencies at which the soft lag is present shift to higher energies while the amplitude decreases. The evolution of the soft lag towards shorter time scales has been interpreted as a contracting emitting region, a deduction supported by both spectroscopic (Plant et al., 2014; J. A. García, James F. Steiner, et al., 2015) and timing studies (Ingram and Done, 2011; Marco, Ponti, et al., 2015), as emphasized by E. Kara, J. F. Steiner, et al. (2019). However, the nature of this soft-lag evolution remains uncertain, whether it is modulated by a shrinking corona or a truncated accretion disk extending closer to the compact object.

Our spectral modelling results suggest minimal to no change in the inner disk radius, indicating a potential contraction of the corona instead. Furthermore, our timing anal-

ysis reveals an increase in QPO frequency during the hard state. If the QPO is generated by oscillations in the corona (Zanotti et al. (2005); Cabanac et al. (2010)), then a smaller and hotter corona (inferred from spectral fitting) would oscillate at higher frequencies (Buisson et al., 2019).

These findings align with the timing study of MAXI J1820+070 conducted by E. Kara, J. F. Steiner, et al. (2019), where they observed reverberation lags evolving to higher frequencies. Additionally, using *NICER* spectra, they observed a stable broad-line component of the Fe K line profile coexisting with a narrow component, which becomes less prominent in the later stages. We have independently confirmed this evolution of the Fe K line profile with *Nu*STAR data as illustrated in Fig. 23. E. Kara, J. F. Steiner, et al. (2019) propose that an evolving corona, situated above the black hole in a 'lamp-post' geometry, vertically extends during the onset of the outburst and subsequently contracts at later times. If we assume the narrow component results from the corona irradiating the disk at larger radii (where relativistic effects are less prominent) with the relativistically broadened component resulting from the corona irradiating the disk at smaller radii, then as the corona contracts, the amount of light reaching the outer regions decreases, leading to a diminished equivalent width of the narrow component and an unchanging broad component. Additionally, as the corona contracts, its time variability decreases and the corona extends closer to the disk, causing the reverberation lag to shift to higher frequencies and reducing the amplitude of the lag.

Buisson et al. (2019) attempted to confirm the hypothesis of a contracting corona spectroscopically. They used two instances of a `Relxill` model based on a lamp-post geometry (`RelxilllpCP`) to describe a vertically extended corona. Their findings indicate a decrease in the height of the upper lamp-post corona during the hard state without definitive evidence of disk truncation.

5.4 The expansion of the corona

During the hard-to-soft state transition, we observe a regression of the frequencies dominated by soft lag to lower values, coupled with an increase in lag amplitude, as depicted in Fig. 37. Concurrently, the peak frequency of the QPO shifts to lower energies during this transition, as illustrated in Fig. 29. In the context of a lamp-post corona scenario, these findings suggest an expanding corona. As mentioned previously, a smaller corona would necessitate oscillations at higher frequencies. Therefore, the observed shift of the QPO and soft-lag frequency region to lower frequencies during an expanding corona aligns with expectations. Furthermore, as the corona extends vertically, the solid angle irradiating the outer disk increases, leading to the observed increase in soft-lag amplitude.

Our findings are in accordance with the investigation conducted by Wang, Mastroserio, et al. (2021) on the disk, corona, and jet connection of MAXI J1820+070, expanding upon the timing study initiated by E. Kara, J. F. Steiner, et al. (2019) into the intermediate state. According to their research, there is a discernible increase in coronal height during the hard-to-soft transition, as revealed by lag-energy spectra fits. Additionally, they observed a radio flare approximately 5 days later, correlating it with the launch of bi-polar relativistic ejecta (Bright et al., 2020). In the proposed model

by Wang, Mastroserio, et al. (2021), a relationship is established between the X-ray corona height and the behaviour of the radio jet. The model suggests that the X-ray corona serves as the base of the jet, which, in its final moments before transitioning to the soft state, is ejected. This model is depicted in Figure 39.

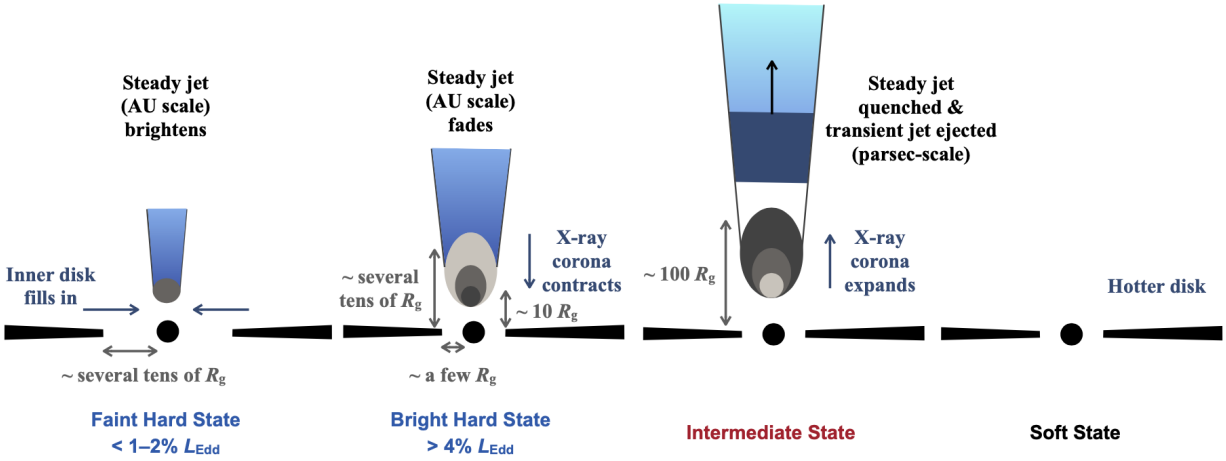

Figure 39: Evolution and geometry of the disk-corona-jet system in different states of a typical BHB illustrated by Wang, Erin Kara, et al. (2022). In the faint hard state, the disk is truncated at several tens of R_g, causing a shorter reverberation lag. In the bright hard state, the disk extends closer to the ISCO, and the X-ray corona contracts vertically from several tens of R_g to ∼10 R_g, leading to fading steady jets. In the intermediate state, the X-ray corona expands to ∼100 R_g, quenching steady jets and ejecting transient jets. In the soft state, limited variability makes analysis challenging, but evidence suggests the disk extends to the ISCO, with dominant disk emission and an inactive radio jet.

5.5 The variation of inclination angle

Our findings suggest that the inclination of MAXI J1820+070 varied throughout the observations in this study. The model indicates a preference for a low inclination at the onset of the hard state, gradually increasing as the system progresses through the hard state and transitions into the soft state. We note that the observed variation in inclination is unlikely to be attributed to physical phenomena like disk warping. Instead, it appears more likely to stem from limitations in the model's ability to precisely characterize the system.

There exists a disparity in the literature regarding the inclination of MAXI J1820+070. During the early stages of the outburst in MAXI J1820+070, X-ray light curve dips were observed (Kajava et al., 2019). Additionally, an increase in the equivalent width of the Hα emission line, interpreted as indicative of a grazing eclipse of the accretion disk, suggests a higher inclination of approximately $60° - 80°$ (Torres, J. Casares, Jiménez-Ibarra, Muñoz-Darias, et al., 2019). Moreover, a measured jet angle of $62 \pm 3°$ implies a higher disk inclination (Atri et al., 2020). This finding is reinforced by radial velocity measurements, which indicate a substantial amplitude and make a low inclination improbable (Torres, J. Casares, Jiménez-Ibarra, Muñoz-Darias, et al., 2019).

Conversely, when modelling the relativistic spectra of MAXI J1820+070 in the hard state, a consensus among various studies (Buisson et al., 2019; Bharali et al., 2019; Xu et al., 2020) suggests a preference for a low inclination of $\sim 30°$. This outcome is expected in spectral modelling, as the method used to determine inclination inherently tends to exhibit bias toward lower inclinations, particularly when a narrow Fe Kα line is detectable. If equal preference is given to both low and high inclination estimates, it suggests a strong disk warping (Xu et al., 2020).

The reflection model `RelxillCp` we have used does not make assumptions about the geometry of the corona, and thus, it cannot directly account for changes in the vertical extent of the corona. We posit that it compensates for the variation in coronal height through the inclination parameter. This rationale is grounded in the observation of the diminishing narrow component of the Fe Kα line (Fig. 23). A more face-on orientation (lower inclination) would theoretically yield a stronger narrow line, as relativistic effects causing line broadening become less pronounced. Conversely, at higher inclinations, relativistic broadening becomes more apparent and may overshadow the narrow line component.

Alternatively, according to the discoveries made by Wang, Mastroserio, et al. (2021), the inclination of MAXI J1820+070 in its spectral fits is pegged at a higher value as the source transitions to the soft state, primarily attributed to the observed blue shift in the Fe K line. If indeed the Fe K line exhibits a blue shift, it follows that the Relxillcp model would adapt to this shift by increasing the inclination, as higher inclination systems are anticipated to experience more pronounced Doppler shifting.

5.6 Potential wind outflows

Our spectral analyses necessitated the incorporation of an additional Gaussian absorption line within the $\sim 6.9 - 7.3$ keV range, as detailed in section 4.2.3.2. These distinctive absorption features potentially signify the existence of photo-ionized absorbing material, manifested in the form of equatorial accretion disk winds. Such wind outflows have been long-standing phenomena observed in BHB systems, initially identified in GRO J1655-40 (Ueda et al., 1998) and GRS 1915+105 (Kotani et al., 2000) through the presence of highly ionized Fe K lines, specifically Fe XXV and Fe XXVI. The Fe XXV and Fe XXVI Kα lines are centred around ~ 6.72 and ~ 7.0 keV, respectively.

Consequently, our detected absorption feature aligns with a hydrogen-like Fe XXVI kα line. It is crucial to emphasize that we identify these absorption features in the hard-state spectra. Disk winds are predominantly observed in the soft state of BHBs with a high inclination (Ponti et al., 2012). This observation challenges the prevalent paradigm associating the hard state with jet dominance and an absence of substantial evidence for wind-like outflows.

Caution is advised when analyzing the presence of narrow absorption features in both *Nu*STAR and *Swift*-XRT spectra due to their limited spectral resolution. For more accurate modelling, grating spectra would be required to better parameterize any outflows

that may be present. Grating spectra can provide more detailed information about the spectral features of the outflows, which can help in photoionization modelling to better understand the outflows' properties. Furthermore, the necessity of adding an absorption feature may be due to the failure of the spectral model to accurately characterise the spectrum.

6 Conclusion

In this thesis, we aimed to understand the spectral and temporal characteristics of the Low-Mass X-ray Binary MAXI J1820+070 and its evolution throughout a historical outburst that started on 11 March 2018. Through these studies, we attempted to develop in-depth knowledge of the geometry, disk-corona connection, outflows and different emission processes responsible for the X-ray emission in BHBs. Additionally, we aimed to test whether a relatively simplistic spectral model can provide a reasonable caveat for explaining the spectra across different accretion states or luminosities.

Due to the fact that the BHXRBs emit over a broad spectrum (a few eVs to hundreds of keV), for the parameterization of the spectral properties, we utilized both joint spectra from *Nu*STAR and *Swift*-XRT, observed nearly simultaneously. For temporal analysis, we utilized *Nu*STAR and *NICER* light curves in different energy bands (ref. to §3 for details). As per long-term lightcurve by the *MAXI*, (§4.1), distinct flaring episodes of MAXI J1820+070 are observed at approximately MJD 58200 and 58300 (23rd May and 1st July 2018, respectively). The first flaring episode corresponds to a prolonged period in the hard state, while the onset of the second flare marks a transition to the soft state. Two subsequent weaker outbursts, termed "re-brightening" and "mini-outburst", maintain the hard state. Additionally, we generated an HID of MAXI J1820+070 (Fig. 17) which depicts a characteristic Q-shaped trajectory, typical of the BHXRBs.

The initial spectral analysis involved choosing a model that accurately describes all the spectral features present in the *Nu*STAR and *Swift*-XRT X-ray spectra, such as the soft photon excess, direct non-thermal emission, reflection component and the Compton hump. Using our simplistic model, we extracted key parameters of the disk and corona (§4.2). In the hard state, MAXI J1820+070's inner disk temperature remains relatively stable until a gradual increase occurs, with a notable spike reaching approximately 0.8 keV during the state transition, indicating the onset of thermal emission. Due to the degeneracy between the spin parameter and the inner disk radius, the spin was frozen to 0.998 to assume a maximally spinning black hole. The inner disk radius ($R_{\rm in}$) gradually extends towards the ISCO as the system progresses to the soft state, but no substantial evidence of disk truncation is observed. The disk inclination varies throughout the transition, likely due to modelling limitations rather than physical factors.

The photon index gradually increases during the hard state, dips briefly at the state transition, and then increases in the soft state. Caution is prompted here, as the sudden increase in photon index during the soft state may be due to challenges in characterizing the decreasing non-thermal emission. The temperature of Comptonizing electrons in the corona steadily rises throughout the hard state, plateauing before the transition,

where it then pegs at a maximum of 1000 keV in the soft state, again attributed to limitations in the model due to the diminishing non-thermal emission. Consequently, the electron temperature was fixed during spectral fits in the soft state.

To investigate the temporal variability of MAXI J1820+070, we constructed power-density spectra for each *Nu*STAR and simultaneous *NICER* observations (§4.3.1). The PDS of the complete calibrated *Nu*STAR energy band (3-79 keV) depict the presence and evolution of QPOs during the hard state, disappearing as the source transitions towards the soft state. Qualitative analysis shows a shift in peak QPO frequency towards higher frequencies throughout the outburst, except at the start of the intermediate state. A second harmonic QPO is also observable, albeit marginally, in the early stages. To explore energy dependence, the *Nu*STAR observations were split into 3-10 keV and 10-79 keV bands, showing a concentration of QPO power in the 3-10 keV range. In the 10-79 keV range, QPOs are less prominent, especially in later stages. *NICER* observations within 0.2-3.0 keV and 3.0-10.0 keV ranges confirm that QPO power mainly resides in the 3.0-10 keV range during the hard state. However, QPOs are observed in the 0.2-3.0 keV range during the intermediate state. The peak frequency of QPOs shifts towards higher energies during the intermediate state. Quantitative analysis using a combination of Lorentzians to fit the *Nu*STAR QPO data, using the lmfit library, reveals a steady transition of QPOs to higher frequencies and increasing prominence throughout the outburst, with a decline in frequency and prominence at the onset of the intermediate state.

In section 4.3.2 we describe the computation of the time lags between hard and soft energy bands using Fourier techniques. This involved segmenting light curves, calculating cross-spectra, and averaging them to determine time lags. *NICER* spectra in the 0.5-1.5 keV and 1.5-3.0 keV bands were used for time lag computation. The resulting lag-frequency plots showed a hard lag at lower frequencies and a soft lag at higher frequencies across observations, consistent with known patterns in Galactic BHBs. During the hard state, there was a decrease in the amplitude of the soft reverberation lag and a shift in the frequency range where soft lag was observed towards higher frequencies. At the onset of the state transition, there was a sudden increase in reverberation lag and a shift towards lower frequencies, indicating a dynamic evolution in the geometric relationship between the corona and the disk.

In conclusion, our investigation into the spectral and temporal evolution of MAXI J1820+070 has uncovered significant insights. The QPOs in the hard state exhibit dynamic centre frequency shifts, quantified through Lorentzian modelling of the PDS. We find that the QPO and broadband noise power are concentrated within the 3.0-10.0 keV range. This result challenges previous findings in other black-hole XRBs, where instead the QPO power dominates in the non-thermal energy bands. Comparing the QPO frequencies and the inner disk radius, we see a dynamic frequency with minimal disk radius variation, challenging expected trends and suggesting the QPOs to the corona's temporal evolution.

During the hard state, lag-frequency spectra analysis suggests a possible contraction of the emitting region, supported by both spectroscopic and timing studies. Spectral modelling implies minimal change in the inner disk radius, pointing towards a poten-

tial contracting corona as the emitting region. An increase in QPO frequency during the hard state aligns with expectations if the QPOs originate from coronal oscillations. The hard-to-soft state transition reveals a regression of soft lag frequencies to lower values, coupled with an increase in lag amplitude. These results, coupled with the concurrent shift of QPO to lower frequencies, suggest an expanding corona following the initial contraction.

The inclination of MAXI J1820+070 appears to vary, with a preference for low inclination at the onset of the hard state, gradually increasing through the hard state and into the soft state. While there are discrepancies in the literature regarding the inclination of MAXI J1820+070, our varied inclination angle can be attributed to modelling precision limitations, underlining the system's complexity. An additional Gaussian absorption line in the hard state, possibly a Fe XXVI Kα absorption line, suggests the presence of equatorial accretion disk winds. Detection of such features challenges the prevalent paradigm associating hard states with jet dominance and raises questions about the role of outflows in different spectral states. However, caution is necessary due to limited spectral resolution, highlighting the need for more detailed grating spectra analysis to understand the properties of potential outflows better.

These findings underscore the complexity of MAXI J1820+070 and highlight the need for further research. The current model's limitations in fully explaining spectral evolution across different states indicate the need for more sophisticated modelling approaches. Improved spectral resolution is essential for more precise and conclusive interpretations of the observed phenomena. Furthermore, extending this investigation into the later stages of the outbursts may uncover additional insights into the system's behaviour and evolution.

7 Future Perspectives

Throughout this study, I've acquired invaluable tools essential for the comprehensive analysis of X-ray data. This includes proficiency in reducing X-ray spectra, developing and validating models, and employing Fourier techniques to explore temporal characteristics in XRBs, all of which are pivotal for a holistic understanding of these systems.

My future research endeavours will focus on a deeper investigation into the spectral and temporal evolution of MAXI J1820+070 and similar low-mass X-ray binaries like the newly discovered Swift J1727.8-1613. I intend to employ more intricate models to capture the complexities of observed spectra across diverse accretion states and luminosities. Incorporating additional physical processes such as disk winds, radio jets, and accretion disk truncation will enhance the precision of spectral characterization.

Expanding upon the temporal analysis techniques acquired during this study, I aim to conduct a comprehensive examination of variability in MAXI J1820+070 and Swift J1727.8-1613. This involves exploring the correlation between the QPOs and broadband noise across various energy bands and accretion states to gain deeper insights into the variability sources in BHBs. Leveraging high-resolution spectroscopic instruments like *XMM*-Newton's reflection grating spectrometer (RGS) and the recently

launched X-Ray Imaging and Spectroscopy Mission (XRISM) telescope, I plan to obtain detailed grating spectra to study absorption lines and emission features, thereby gaining deeper insight into the role of accretion disk winds in the accretion process and its surroundings.

Furthermore, integrating multiwavelength observations, including radio, optical, and infrared, with X-ray data will be pivotal for my future research. By correlating X-ray variability with emissions from other wavelengths, I aim to unravel the mechanisms governing jet formation, disk winds, and the overall accretion-ejection paradigm in BHBs. In summary, my future research will advance our understanding of MAXI J1820+070 and similar systems through detailed spectral and temporal analyses, high-resolution spectroscopy, and multiwavelength studies, thereby contributing significantly to our understanding of the complexities of black hole accretion physics and fundamental astrophysical processes in extreme environments.

References

[1] Diego Altamirano et al. “The evolution of the X-ray phase lags during the outbursts of the black hole candidate GX 339–4”. In: *Monthly Notices of the Royal Astronomical Society* 449.4 (Apr. 2015), pp. 4027–4037. ISSN: 1365-2966. DOI: 10.1093/mnras/stv556. URL: http://dx.doi.org/10.1093/mnras/stv556 (cit. on p. 69).

[2] Jeremy J. Drake Ann A. Esin Jeffrey E. McClintock et al. “Modeling the Low-State Spectrum of the X-Ray Nova XTE J1118+480”. In: *The Astrophysical Journal* 555.1 (July 2001), p. 483. DOI: 10.1086/321450. URL: https://dx.doi.org/10.1086/321450 (cit. on p. 16).

[3] M. Özbey Arabacı et al. “Multiwavelength observations of MAXI J1820+070 during its outburst decay and subsequent mini-outburst”. In: *Monthly Notices of the Royal Astronomical Society* 514.3 (June 28, 2022), pp. 3894–3909. ISSN: 0035-8711, 1365-2966. DOI: 10.1093/mnras/stac1574. arXiv: 2206.02461[astro-ph]. URL: http://arxiv.org/abs/2206.02461 (visited on 01/23/2023) (cit. on p. 71).

[4] K. A. Arnaud. “XSPEC: The First Ten Years”. In: *Astronomical Data Analysis Software and Systems V*. Ed. by George H. Jacoby et al. Vol. 101. Astronomical Society of the Pacific Conference Series. Jan. 1996, p. 17 (cit. on p. 44).

[5] P Atri et al. “A radio parallax to the black hole X-ray binary MAXI-J1820+070”. In: *Monthly Notices of the Royal Astronomical Society: Letters* 493.1 (Jan. 2020), pp. L81–L86. ISSN: 1745-3933. DOI: 10.1093/mnrasl/slaa010. URL: http://dx.doi.org/10.1093/mnrasl/slaa010 (cit. on pp. 28, 74).

[6] Australia Telescope National Facility. *Binary Stars*. 1999. URL: https://www.atnf.csiro.au/outreach/education/senior/astrophysics/binary_intro.html (visited on 12/08/2023) (cit. on p. 6).

[7] M. Cristina Baglio et al. “Optical observations of MAXI J1820+070 suggest it is a black hole X-ray binary”. In: *The Astronomer’s Telegram* 11418 (Mar. 2018), p. 1 (cit. on p. 28).

[8] Steven A. Balbus et al. “A Powerful Local Shear Instability in Weakly Magnetized Disks. I. Linear Analysis”. In: *The Astrophysical Journal* 376 (July 1991), p. 214. DOI: 10.1086/170270 (cit. on p. 16).

[9] Cosimo Bambi et al. *Testing General Relativity with Black Hole X-Ray Data and ABHModels*. 2023. arXiv: 2307.12755 [astro-ph.IM] (cit. on p. 17).

[10] Scott Barthelmy et al. “The burst alert telescope (BAT) on the SWIFT midex mission”. In: *Space Science Reviews* 120 (Oct. 2005), pp. 143–164. DOI: 10.1007/s11214-005-5096-3 (cit. on p. 32).

[11] T. Belloni et al. “The evolution of the timing properties of the black-hole transient GX 339-4 during its 2002/2003 outburst”. In: *Astronomy & Astrophysics* 440.1 (Aug. 2005), pp. 207–222. DOI: 10.1051/0004-6361:20042457. URL: https://doi.org/10.1051%2F0004-6361%3A20042457 (cit. on p. 13).

[12] Tomaso Belloni. "Black Hole States: Accretion and Jet Ejection". In: *AIP Conference Proceedings*. Vol. 797. ISSN: 0094243X. 2005, pp. 197–204. DOI: 10.1063/1.2130233. arXiv: astro-ph/0504185. URL: http://arxiv.org/abs/astro-ph/0504185 (visited on 05/09/2023) (cit. on p. 22).

[13] N. Ben Bekhti et al. "HI4PI: a full-sky Hi survey based on EBHIS and GASS". In: *Astronomy & Astrophysics* 594 (Oct. 2016), A116. ISSN: 1432-0746. DOI: 10.1051/0004-6361/201629178. URL: http://dx.doi.org/10.1051/0004-6361/201629178 (cit. on p. 51).

[14] Philip R. Bevington. *Data reduction and error analysis for the physical sciences*. 1969 (cit. on p. 46).

[15] Priya Bharali et al. "Broad-band spectral study of X-ray transient MAXI J1820+070 using Swift/XRT and NuSTAR". In: *Monthly Notices of the Royal Astronomical Society* 487.4 (Aug. 21, 2019), pp. 5946–5951. ISSN: 0035-8711. DOI: 10.1093/mnras/stz1686. URL: https://doi.org/10.1093/mnras/stz1686 (visited on 01/23/2023) (cit. on pp. 54, 75).

[16] Niek Bollemeijer et al. *Evidence for a dynamic corona in the short-term time lags of black hole X-ray binary MAXI J1820+070*. 2023. arXiv: 2312.09835 [astro-ph.HE] (cit. on p. 29).

[17] J. S. Bright et al. "An extremely powerful long-lived superluminal ejection from the black hole MAXI J1820+070". In: *Nature Astronomy* 4.7 (Mar. 2020), pp. 697–703. ISSN: 2397-3366. DOI: 10.1038/s41550-020-1023-5. URL: http://dx.doi.org/10.1038/s41550-020-1023-5 (cit. on pp. 29, 73).

[18] D J K Buisson et al. "MAXI J1820+070 with NuSTAR I. An increase in variability frequency but a stable reflection spectrum: coronal properties and implications for the inner disc in black hole binaries". In: *Monthly Notices of the Royal Astronomical Society* 490.1 (Nov. 21, 2019), pp. 1350–1362. ISSN: 0035-8711, 1365-2966. DOI: 10.1093/mnras/stz2681. URL: https://academic.oup.com/mnras/article/490/1/1350/5575196 (visited on 01/23/2023) (cit. on pp. 29, 42, 72, 73, 75).

[19] David N. Burrows et al. "The Swift X-Ray Telescope". In: *Space Science Reviews* 120.3-4 (Oct. 2005), pp. 165–195. DOI: 10.1007/s11214-005-5097-2. URL: https://doi.org/10.1007%2Fs11214-005-5097-2 (cit. on pp. 32–34).

[20] C. Cabanac et al. "Variability of X-ray binaries from an oscillating hot corona". In: *Monthly Notices of the Royal Astronomical Society* 404.2 (May 2010), pp. 738–748. DOI: 10.1111/j.1365-2966.2010.16340.x. URL: https://doi.org/10.1111%2Fj.1365-2966.2010.16340.x (cit. on pp. 25, 71, 73).

[21] B. Carter. "Axisymmetric Black Hole Has Only Two Degrees of Freedom". In: *Phys. Rev. Lett.* 26 (6 Jan. 1971), pp. 331–333. DOI: 10.1103/PhysRevLett.26.331. URL: https://link.aps.org/doi/10.1103/PhysRevLett.26.331 (cit. on p. 9).

[22] Jorge Casares et al. “X-Ray Binaries”. In: *Handbook of Supernovae*. Ed. by Athem W. Alsabti et al. Cham: Springer International Publishing, 2017, pp. 1499–1526. ISBN: 978-3-319-21846-5. DOI: 10.1007/978-3-319-21846-5_111. URL: https://doi.org/10.1007/978-3-319-21846-5_111 (cit. on p. 6).

[23] P. Casella et al. “A study of the low-frequency quasi-periodic oscillations in the X-ray light curves of the black hole candidate XTE J1859+226”. In: *Astronomy & Astrophysics* 426.2 (Oct. 2004), pp. 587–600. ISSN: 1432-0746. DOI: 10.1051/0004-6361:20041231. URL: http://dx.doi.org/10.1051/0004-6361:20041231 (cit. on p. 71).

[24] Oberto Citterio et al. “Characteristics of the flight model optics for the JET-X telescope onboard the Spectrum-X-Gamma satellite”. In: *Multilayer and Grazing Incidence X-Ray/EUV Optics III*. Ed. by Richard B. Hoover et al. Vol. 2805. International Society for Optics and Photonics. SPIE, 1996, pp. 56–65. DOI: 10.1117/12.245112. URL: https://doi.org/10.1117/12.245112 (cit. on p. 32).

[25] S. Corbel et al. *Coupling of the X-ray and radio emission in the black hole candidate a nd compact jet source GX 339-4*. 2000. arXiv: astro-ph/0003460 [astro-ph] (cit. on p. 14).

[26] T. Dauser, J. Garcia, et al. “Irradiation of an accretion disc by a jet: general properties and implications for spin measurements of black holes”. In: *Monthly Notices of the Royal Astronomical Society* 430.3 (Feb. 2013), pp. 1694–1708. ISSN: 0035-8711. DOI: 10.1093/mnras/sts710. URL: http://dx.doi.org/10.1093/mnras/sts710 (cit. on pp. 11, 17).

[27] T. Dauser, J. García, et al. “The role of the reflection fraction in constraining black hole spin”. In: *Monthly Notices of the Royal Astronomical Society: Letters* 444.1 (Aug. 2014), pp. L100–L104. ISSN: 1745-3925. DOI: 10.1093/mnrasl/slu125. eprint: https://academic.oup.com/mnrasl/article-pdf/444/1/L100/54653706/mnrasl_444_1_l100.pdf. URL: https://doi.org/10.1093/mnrasl/slu125 (cit. on p. 52).

[28] T. Dauser, J. Garcìa, et al. “Irradiation of an accretion disc by a jet: general properties and implications for spin measurements of black holes”. In: *Monthly Notices of the Royal Astronomical Society* 430.3 (Apr. 2013), pp. 1694–1708. DOI: 10.1093/mnras/sts710. arXiv: 1301.4922 [astro-ph.HE] (cit. on p. 52).

[29] Shane W. Davis et al. “Relativistic Accretion Disk Models of High-State Black Hole X-Ray Binary Spectra”. In: *The Astrophysical Journal* 621.1 (Mar. 2005), p. 372. DOI: 10.1086/427278. URL: https://dx.doi.org/10.1086/427278 (cit. on p. 16).

[30] B. De Marco et al. “Evolution of the reverberation lag in GX 339-4 at the end of an outburst”. In: *Monthly Notices of the Royal Astronomical Society* 471.2 (Oct. 2017), pp. 1475–1487. DOI: 10.1093/mnras/stx1649. arXiv: 1706.10053 [astro-ph.HE] (cit. on p. 69).

[31] Jean-Pierre De Villiers et al. “Magnetically Driven Accretion Flows in the Kerr Metric. I. Models and Overall Structure”. In: *The Astrophysical Journal* 599.2 (Dec. 2003), p. 1238. DOI: 10.1086/379509. URL: https://dx.doi.org/10.1086/379509 (cit. on p. 16).

[32] D. Denisenko. “Optical follow-up of MAXI J1820+070 and possible identity with ASASSN-18ey”. In: *The Astronomer’s Telegram* 11400 (Mar. 2018), p. 1 (cit. on p. 28).

[33] V. Dhawan et al. “AU-Scale Synchrotron Jets and Superluminal Ejecta in GRS 1915+105”. In: *The Astrophysical Journal* 543.1 (Nov. 2000), pp. 373–385. DOI: 10.1086/317088. arXiv: astro-ph/0006086 [astro-ph] (cit. on p. 14).

[34] M. Dovčiak et al. “An Extended Scheme for Fitting X-Ray Data with Accretion Disk Spectra in the Strong Gravity Regime”. In: *The Astrophysical Journal Supplement Series* 153.1 (July 2004), p. 205. DOI: 10.1086/421115. URL: https://dx.doi.org/10.1086/421115 (cit. on p. 16).

[35] ESA: XMM-Newton SOC. *XMM-Newton Users Handbook*. 2.21. European Space Agency, XMM-Newton Science Operations Centre. 2023 (cit. on pp. 29, 30).

[36] Ann A. Esin, Jeffrey E. McClintock, et al. “Advection-Dominated Accretion and the Spectral States of Black Hole X-Ray Binaries: Application to Nova Muscae 1991”. In: *The Astrophysical Journal* 489.2 (Nov. 1997), p. 865. DOI: 10.1086/304829. URL: https://dx.doi.org/10.1086/304829 (cit. on pp. 19–22).

[37] Ann A. Esin, Ramesh Narayan, et al. “Spectral Transitions in Cygnus X-1 and Other Black Hole X-Ray Binaries”. In: *The Astrophysical Journal* 505.2 (Oct. 1998), pp. 854–868. DOI: 10.1086/306186. URL: https://doi.org/10.1086%2F306186 (cit. on p. 20).

[38] A. C. Fabian, M. J. Rees, et al. “X-ray fluorescence from the inner disc in Cygnus X-1”. In: *Monthly Notices of the Royal Astronomical Society* 238.3 (June 1989), pp. 729–736. ISSN: 0035-8711. DOI: 10.1093/mnras/238.3.729. eprint: https://academic.oup.com/mnras/article-pdf/238/3/729/3564470/mnras238-0729.pdf. URL: https://doi.org/10.1093/mnras/238.3.729 (cit. on p. 11).

[39] A. C. Fabian, A. Zoghbi, et al. “Broad line emission from iron K- and L-shell transitions in the active galaxy 1H0707-495”. In: *Nature* 459.7246 (May 2009), pp. 540–542. DOI: 10.1038/nature08007 (cit. on p. 69).

[40] R. P. Fender et al. “Towards a unified model for black hole X-ray binary jets”. In: *Monthly Notices of the Royal Astronomical Society* 355.4 (Dec. 2004), pp. 1105–1118. ISSN: 0035-8711. DOI: 10.1111/j.1365-2966.2004.08384.x. eprint: https://academic.oup.com/mnras/article-pdf/355/4/1105/6271740/355-4-1105.pdf. URL: https://doi.org/10.1111/j.1365-2966.2004.08384.x (cit. on pp. 22, 23).

[41] Rob Fender. *Relativistic outflows from X-ray binaries (a.k.a. ‘Microquasars’)*. 2001. arXiv: astro-ph/0109502 [astro-ph] (cit. on p. 8).

[42] Robert Fender et al. “Quenching of the Radio Jet during the X-Ray High State of GX 339–4”. In: *The Astrophysical Journal* 519.2 (June 1999), p. L165. DOI: 10.1086/312128. URL: https://dx.doi.org/10.1086/312128 (cit. on p. 14).

[43] E. Gallo et al. “A universal radio–X-ray correlation in low/hard state black hole binaries”. In: *Monthly Notices of the Royal Astronomical Society* 344.1 (Sept. 2003), pp. 60–72. ISSN: 0035-8711. DOI: 10.1046/j.1365-8711.2003.06791.x. eprint: https://academic.oup.com/mnras/article-pdf/344/1/60/18651408/344-1-60.pdf. URL: https://doi.org/10.1046/j.1365-8711.2003.06791.x (cit. on p. 14).

[44] Charles F. Gammie. “The Magnetorotational Instability in the Kerr Metric”. In: *The Astrophysical Journal* 614.1 (Aug. 2004), p. 309. DOI: 10.1086/423443. URL: https://dx.doi.org/10.1086/423443 (cit. on p. 16).

[45] Chenxu Gao et al. “Low-frequency quasi-periodic oscillation in MAXI J1820+070: Revealing distinct Compton and reflection contributions”. In: *Monthly Notices of the Royal Astronomical Society* 520.4 (Feb. 2023), pp. 5544–5551. ISSN: 1365-2966. DOI: 10.1093/mnras/stad434. URL: http://dx.doi.org/10.1093/mnras/stad434 (cit. on p. 29).

[46] J. García, T. Dauser, et al. “IMPROVED REFLECTION MODELS OF BLACK HOLE ACCRETION DISKS: TREATING THE ANGULAR DISTRIBUTION OF X-RAYS”. In: *The Astrophysical Journal* 782.2 (Jan. 2014), p. 76. DOI: 10.1088/0004-637X/782/2/76. URL: https://dx.doi.org/10.1088/0004-637X/782/2/76 (cit. on p. 52).

[47] J. García et al. “X-RAY REFLECTED SPECTRA FROM ACCRETION DISK MODELS. I. CONSTANT DENSITY ATMOSPHERES”. In: *The Astrophysical Journal* 718.2 (July 2010), p. 695. DOI: 10.1088/0004-637X/718/2/695. URL: https://dx.doi.org/10.1088/0004-637X/718/2/695 (cit. on p. 11).

[48] Javier A. García, Matteo Bachetti, et al. *Probing the Black Hole Engine with Measurements of the Relativistic X-ray Reflection Component*. 2019. arXiv: 1903.07130 [astro-ph.HE] (cit. on p. 11).

[49] Javier A. García, James F. Steiner, et al. “X-RAY REFLECTION SPECTROSCOPY OF THE BLACK HOLE GX 339–4: EXPLORING THE HARD STATE WITH UNPRECEDENTED SENSITIVITY”. In: *The Astrophysical Journal* 813.2 (Oct. 2015), p. 84. ISSN: 1538-4357. DOI: 10.1088/0004-637x/813/2/84. URL: http://dx.doi.org/10.1088/0004-637X/813/2/84 (cit. on p. 72).

[50] N. Gehrels. “The Swift Gamma-Ray Burst Mission”. In: *AIP Conference Proceedings*. AIP, 2004. DOI: 10.1063/1.1810924. URL: https://doi.org/10.1063%2F1.1810924 (cit. on pp. 32, 33).

[51] Marek Gierliński et al. “Application of a relativistic accretion disc model to X-ray spectra of LMC X-1 and GRO J1655-40”. In: *Monthly Notices of the Royal Astronomical Society* 325 (2001), pp. 1253–1265. URL: https://api.semanticscholar.org/CorpusID:14901025 (cit. on p. 15).

[52] J. E. Grove et al. “Gamma-Ray Spectral States of Galactic Black Hole Candidates”. In: *The Astrophysical Journal* 500.2 (June 1998), p. 899. DOI: 10.1086/305746. URL: https://dx.doi.org/10.1086/305746 (cit. on p. 13).

[53] Francesco Haardt et al. “X-Ray Spectra from Two-Phase Accretion Disks”. In: *The Astrophysical Journal* 413 (Aug. 1993), p. 507. DOI: 10.1086/173020 (cit. on p. 16).

[54] Fiona A. Harrison et al. “THE *NUCLEAR SPECTROSCOPIC TELESCOPE ARRAY* (*NuSTAR*) HIGH-ENERGY X-RAY MISSION”. In: *The Astrophysical Journal* 770.2 (May 30, 2013), p. 103. ISSN: 0004-637X, 1538-4357. DOI: 10.1088/0004-637X/770/2/103. URL: https://iopscience.iop.org/article/10.1088/0004-637X/770/2/103 (visited on 03/01/2023) (cit. on p. 31).

[55] J. Homan et al. “Correlated X-Ray Spectral and Timing Behavior of the Black Hole Candidate XTE J1550-564: A New Interpretation of Black Hole States”. In: *The Astrophysical Journal Supplement Series* 132.2 (Feb. 2001), pp. 377–402. DOI: 10.1086/318954. URL: https://doi.org/10.1086%2F318954 (cit. on pp. 13, 24).

[56] Adam Ingram, Chris Done, and P. Chris Fragile. “Low-frequency quasi-periodic oscillations spectra and Lense-Thirring precession”. In: *Monthly Notices of the Royal Astronomical Society: Letters* 397.1 (July 2009), pp. L101–L105. DOI: 10.1111/j.1745-3933.2009.00693.x. URL: https://doi.org/10.1111%2Fj.1745-3933.2009.00693.x (cit. on p. 25).

[57] Adam Ingram et al. “A physical model for the continuum variability and quasi-periodic oscillation in accreting black holes”. In: *Monthly Notices of the Royal Astronomical Society* 415.3 (Aug. 2011), pp. 2323–2335. DOI: 10.1111/j.1365-2966.2011.18860.x. arXiv: 1101.2336 [astro-ph.SR] (cit. on p. 72).

[58] A. Joinet et al. “Hard X-Ray Emission of the Microquasar GX 339-4 in the Low/Hard State”. In: *The Astrophysical Journal* 657.1 (Mar. 2007), pp. 400–408. DOI: 10.1086/510326. URL: https://doi.org/10.1086%2F510326 (cit. on p. 71).

[59] J. S. Kaastra et al. “Optimal binning of X-ray spectra and response matrix design”. In: *Astronomy & Astrophysics* 587 (Mar. 2016), A151. DOI: 10.1051/0004-6361/201527395. URL: https://doi.org/10.1051%5C%2F0004-6361%5C%2F201527395 (cit. on pp. 37, 38).

[60] J J E Kajava et al. “X-ray dips and a complex UV/X-ray cross-correlation function in the black hole candidate MAXI J1820+070”. In: *Monthly Notices of the Royal Astronomical Society: Letters* 488.1 (June 2019), pp. L18–L23. ISSN: 1745-3925. DOI: 10.1093/mnrasl/slz089. eprint: https://academic.oup.com/mnrasl/article-pdf/488/1/L18/28898322/slz089.pdf. URL: https://doi.org/10.1093/mnrasl/slz089 (cit. on p. 74).

[61] E. Kara, W. N. Alston, et al. “A global look at X-ray time lags in Seyfert galaxies”. In: *Monthly Notices of the Royal Astronomical Society* 462.1 (Oct. 2016), pp. 511–531. DOI: 10.1093/mnras/stw1695. arXiv: 1605.02631 [astro-ph.HE] (cit. on p. 69).

[62] E. Kara, A. C. Fabian, et al. “The Compton hump and variable blue wing in the extreme low-flux NuSTAR observations of 1H0707-495”. In: *Monthly Notices of the Royal Astronomical Society* 449.1 (Mar. 2015), pp. 234–242. ISSN: 0035-8711. DOI: 10.1093/mnras/stv304. eprint: https://academic.oup.com/mnras/article-pdf/449/1/234/4143009/stv304.pdf. URL: https://doi.org/10.1093/mnras/stv304 (cit. on p. 11).

[63] E. Kara, J. F. Steiner, et al. “The corona contracts in a black-hole transient”. In: *Nature* 565.7738 (Jan. 2019), pp. 198–201. DOI: 10.1038/s41586-018-0803-x. URL: https://doi.org/10.1038%2Fs41586-018-0803-x (cit. on pp. 29, 69, 72, 73).

[64] S. Kato et al. *Black-Hole Accretion Disks — Towards a New Paradigm —*. 2008 (cit. on p. 9).

[65] T. Kawamuro et al. “MAXI/GSC detection of a probable new X-ray transient MAXI J1820+070”. In: *The Astronomer’s Telegram* 11399 (Mar. 2018), p. 1 (cit. on p. 28).

[66] M. van der Klis. *A review of rapid X-ray variability in X-ray binaries*. 2004. arXiv: astro-ph/0410551 [astro-ph] (cit. on pp. 11, 12).

[67] Taro Kotani et al. “ASCA Observations of the Absorption Line Features from the Superluminal Jet Source GRS 1915+105”. In: *The Astrophysical Journal* 539.1 (Aug. 2000), pp. 413–423. DOI: 10.1086/309200. arXiv: astro-ph/0003237 [astro-ph] (cit. on p. 75).

[68] O. Kotov et al. “On the X-ray time-lags in the black hole candidates”. In: *Monthly Notices of the Royal Astronomical Society* 327.3 (Nov. 2001), pp. 799–807. DOI: 10.1046/j.1365-8711.2001.04769.x. arXiv: astro-ph/0103115 [astro-ph] (cit. on p. 69).

[69] Peter Kretschmar et al. “Stellar Winds in Massive X-ray Binaries”. In: *Proceedings of the International Astronomical Union* 12.S329 (Nov. 2016), pp. 355–358. ISSN: 1743-9221. DOI: 10.1017/s1743921317002411. URL: http://dx.doi.org/10.1017/S1743921317002411 (cit. on p. 7).

[70] Aya Kubota, Ken Ebisawa, et al. “On the Temperature Profile of Radiatively Efficient Geometrically Thin Disks in Black Hole Binaries with the ASCA GIS”. In: *The Astrophysical Journal* 631.2 (Oct. 2005), pp. 1062–1071. DOI: 10.1086/432900 (cit. on p. 15).

[71] Aya Kubota et al. “The Three Spectral Regimes Found in the Stellar Black Hole XTE J1550-564 in Its High/Soft State”. In: *The Astrophysical Journal* 601.1 (Jan. 2004), pp. 428–438. DOI: 10.1086/380433 (cit. on pp. 15, 18).

[72] D.A. Leahy et al. “On searches for pulsed emission with application to four globular cluster X-ray sources : NGC 1851, 6441, 6624 and 6712.” In: *The Astrophysical Journal* 266 (Mar. 1983), pp. 160–170. DOI: 10.1086/160766 (cit. on pp. 11, 61).

[73] Li-Xin Li et al. “Multitemperature Blackbody Spectrum of a Thin Accretion Disk around a Kerr Black Hole: Model Computations and Comparison with Observations”. In: *The Astrophysical Journal Supplement Series* 157.2 (Apr. 2005), p. 335. DOI: 10.1086/428089. URL: https://dx.doi.org/10.1086/428089 (cit. on p. 16).

[74] Matteo Lucchini et al. “Investigating the Impact of Vertically Extended Coronae on X-Ray Reverberation Mapping”. In: *The Astrophysical Journal* 951.1 (June 2023), p. 19. ISSN: 1538-4357. DOI: 10.3847/1538-4357/acd24f. URL: http://dx.doi.org/10.3847/1538-4357/acd24f (cit. on p. 29).

[75] Dipankar Maitra et al. “Constraining jet/disc geometry and radiative processes in stellar black holes XTE J1118+480 and GX 339-4”. In: *Monthly Notices of the Royal Astronomical Society* 398.4 (Sept. 2009), pp. 1638–1650. ISSN: 0035-8711. DOI: 10.1111/j.1365-2966.2009.14896.x. eprint: https://academic.oup.com/mnras/article-pdf/398/4/1638/3040843/mnras0398-1638.pdf. URL: https://doi.org/10.1111/j.1365-2966.2009.14896.x (cit. on p. 17).

[76] K. Makishima et al. “Simultaneous X-Ray and Optical Observations of GX 339-4 in an X-Ray High State”. In: *The Astrophysical Journal* 308 (Sept. 1986), p. 635. DOI: 10.1086/164534 (cit. on p. 15).

[77] B. De Marco, G. Ponti, et al. *Tracing the reverberation lag in the hard state of black hole X-ray binaries*. 2015. arXiv: 1510.02798 [astro-ph.HE] (cit. on p. 72).

[78] B. De Marco, A. A. Zdziarski, et al. “The inner flow geometry in MAXI J1820+070 during hard and hard-intermediate states”. In: *Astronomy & Astrophysics* 654 (Oct. 2021), A14. DOI: 10.1051/0004-6361/202140567. URL: https://doi.org/10.1051%2F0004-6361%2F202140567 (cit. on p. 69).

[79] Sera Markoff, Michael Nowak, and Jörn Wilms. “Going with the Flow: Can the Base of Jets Subsume the Role of Compact Accretion Disk Coronae?” In: *The Astrophysical Journal* 635.2 (Dec. 2005), p. 1203. DOI: 10.1086/497628. URL: https://dx.doi.org/10.1086/497628 (cit. on p. 17).

[80] Sera Markoff et al. “Constraining X-Ray Binary Jet Models via Reflection”. In: *The Astrophysical Journal* 609.2 (July 2004), pp. 972–976. DOI: 10.1086/421099. arXiv: astro-ph/0403468 [astro-ph] (cit. on p. 16).

[81] Craig Markwardt et al. *The Neutron Star Interior Composition Explorer Mission Guide*. https://heasarc.gsfc.nasa.gov/docs/nicer/mission_guide/. 2023 (cit. on p. 31).

[82] Ryoji Matsumoto et al. “Global 3D MHD Simulations of Optically Thin Black Hole Accretion Disks”. In: *Progress of Theoretical Physics Supplement* 155 (May 2004), pp. 124–131. DOI: 10.1143/PTPS.155.124 (cit. on p. 16).

[83] G. Matt et al. “Iron K-alpha line from X-ray illuminated relativistic disks.” In: *Astronomy and Astrophysics* 257 (Apr. 1992), pp. 63–68 (cit. on p. 16).

[84] Jeffrey E. McClintock et al. “Black hole binaries”. In: *Compact stellar X-ray sources*. Vol. 39. 2006, pp. 157–213. DOI: 10.48550/arXiv.astro-ph/0306213 (cit. on pp. 11, 13–15, 17, 18, 22).

[85] Jonathan C. McKinney et al. “A Measurement of the Electromagnetic Luminosity of a Kerr Black Hole”. In: *The Astrophysical Journal* 611.2 (Aug. 2004), p. 977. DOI: 10.1086/422244. URL: https://dx.doi.org/10.1086/422244 (cit. on p. 16).

[86] A. Merloni. “Beyond the standard accretion disc model: coupled magnetic disc–corona solutions with a physically motivated viscosity law”. In: *Monthly Notices of the Royal Astronomical Society* 341.3 (May 2003), pp. 1051–1056. ISSN: 0035-8711. DOI: 10.1046/j.1365-8711.2003.06496.x. eprint: https://academic.oup.com/mnras/article-pdf/341/3/1051/3220439/341-3-1051.pdf. URL: https://doi.org/10.1046/j.1365-8711.2003.06496.x (cit. on p. 16).

[87] A. Merloni et al. “Coronal outflow dominated accretion discs: a new possibility for low-luminosity black holes?” In: *Monthly Notices of the Royal Astronomical Society* 332.1 (May 2002), pp. 165–175. ISSN: 0035-8711. DOI: 10.1046/j.1365-8711.2002.05288.x. eprint: https://academic.oup.com/mnras/article-pdf/332/1/165/2967446/332-1-165.pdf. URL: https://doi.org/10.1046/j.1365-8711.2002.05288.x (cit. on p. 16).

[88] K. Mitsuda et al. “Energy spectra of low-mass binary X-ray sources observed from Tenma.” In: *Publications of the Astronomical Society of Japan* 36 (Jan. 1984), pp. 741–759 (cit. on p. 15).

[89] Sigenori Miyamoto, Sayuri Iga, et al. “Another Canonical Time Variation of X-Rays from Black Hole Candidates in the Very High Flare State?” In: *The Astrophysical Journal* 403 (Jan. 1993), p. L39. DOI: 10.1086/186716 (cit. on p. 12).

[90] Sigenori Miyamoto et al. “A Jet Model for a Very High State of GX 339-4”. In: *The Astrophysical Journa* 374 (June 1991), p. 741. DOI: 10.1086/170158 (cit. on pp. 12, 24).

[91] Sigenori Miyamoto et al. “X-ray time variations from Cygnus X-1 and implications for the accretion process”. In: *Nature* 342.6251 (Dec. 1989), pp. 773–774. DOI: 10.1038/342773a0 (cit. on p. 69).

[92] M. A. Moret et al. “Fluctuation analysis of stellar x-ray binary systems”. In: *Phys. Rev. E* 68 (4 Aug. 2003), p. 041104. DOI: 10.1103/PhysRevE.68.041104. URL: https://link.aps.org/doi/10.1103/PhysRevE.68.041104 (cit. on p. 9).

[93] E. H. Morgan et al. “RXTE Observations of QPOs in the Black Hole Candidate GRS 1915+105”. In: *The Astrophysical Journal* 482.2 (June 1997), pp. 993–1010. DOI: 10.1086/304191 (cit. on p. 13).

[94] S. Motta, J. Homan, et al. “Discovery of two simultaneous non-harmonically related quasi-periodic oscillations in the 2005 outburst of the black hole binary GRO J1655-40”. In: *Monthly Notices of the Royal Astronomical Society* 427.1 (Nov. 2012), pp. 595–606. DOI: 10.1111/j.1365-2966.2012.22037.x. URL: https://doi.org/10.1111%2Fj.1365-2966.2012.22037.x (cit. on p. 24).

[95] S. Motta, T. Muñ oz-Darias, et al. “Low-frequency oscillations in black holes: a spectral-timing approach to the case of GX 339-4”. In: *Monthly Notices of the Royal Astronomical Society* 418.4 (Nov. 2011), pp. 2292–2307. DOI: 10.1111/j.1365-2966.2011.19566.x. URL: https://doi.org/10.1111%2Fj.1365-2966.2011.19566.x (cit. on pp. 4, 24, 26).

[96] S. E. Motta, P. Casella, et al. “Geometrical constraints on the origin of timing signals from black holes”. In: *Monthly Notices of the Royal Astronomical Society* 447.2 (Jan. 2015), pp. 2059–2072. DOI: 10.1093/mnras/stu2579. URL: https://doi.org/10.1093%2Fmnras%2Fstu2579 (cit. on p. 24).

[97] S. E. Motta, T. Muñ oz-Darias, et al. “Black hole spin measurements through the relativistic precession model: XTE J1550-564”. In: *Monthly Notices of the Royal Astronomical Society: Letters* 439.1 (Jan. 2014), pp. L65–L69. DOI: 10.1093/mnrasl/slt181. URL: https://doi.org/10.1093%2Fmnrasl%2Fslt181 (cit. on p. 25).

[98] S.E. Motta et al. “The INTEGRAL view on black hole X-ray binaries”. In: *New Astronomy Reviews* 93 (2021), p. 101618. ISSN: 1387-6473. DOI: https://doi.org/10.1016/j.newar.2021.101618. URL: https://www.sciencedirect.com/science/article/pii/S1387647321000063 (cit. on p. 10).

[99] Ramesh Narayan. “Advection-dominated Models of Luminous Accreting Black Holes”. In: *The Astrophysical Journal* 462 (May 1996), p. 136. DOI: 10.1086/177136. arXiv: astro-ph/9510028 [astro-ph] (cit. on p. 16).

[100] Ramesh Narayan, Jeffrey E. McClintock, et al. “A New Model for Black Hole Soft X-Ray Transients in Quiescence”. In: *The Astrophysical Journal* 457 (Feb. 1996), p. 821. DOI: 10.1086/176777. arXiv: astro-ph/9508014 [astro-ph] (cit. on p. 16).

[101] Ramesh Narayan et al. “Advection-dominated Accretion: A Self-similar Solution”. In: *The Astrophysical Journal* 428 (June 1994), p. L13. DOI: 10.1086/187381. arXiv: astro-ph/9403052 [astro-ph] (cit. on p. 16).

[102] E. Nespoli et al. “A transient variable 6 Hz QPO from GX 339-4”. In: *Astronomy & Astrophysics* 412.1 (Nov. 2003), pp. 235–240. DOI: 10.1051/0004-6361:20031423. URL: https://doi.org/10.1051%2F0004-6361%3A20031423 (cit. on p. 24).

[103] M. A. Nowak. “Are there three peaks in the power spectra of GX 339-4 and Cyg X-1?” In: *Monthly Notices of the Royal Astronomical Society* 318.2 (Aug. 2000), pp. 361–367. DOI: 10.1046/j.1365-8711.2000.03668.x. arXiv: astro-ph/0005232 [astro-ph] (cit. on p. 12).

[104] *NuSTAR Instrumentation*. NuSTAR. URL: https://nustar.caltech.edu/page/instrumentation (visited on 03/01/2023) (cit. on p. 31).

[105] D. S. Plant et al. "Revealing accretion on to black holes: X-ray reflection throughout three outbursts of GX 339-4". In: *Monthly Notices of the Royal Astronomical Society* 442.2 (June 2014), pp. 1767–1785. ISSN: 0035-8711. DOI: 10.1093/mnras/stu867. URL: http://dx.doi.org/10.1093/mnras/stu867 (cit. on pp. 71, 72).

[106] G. Ponti et al. "Ubiquitous equatorial accretion disc winds in black hole soft states". In: *Monthly Notices of the Royal Astronomical Society: Letters* 422.1 (May 2012), pp. L11–L15. ISSN: 1745-3925. DOI: 10.1111/j.1745-3933.2012.01224.x. URL: http://dx.doi.org/10.1111/j.1745-3933.2012.01224.x (cit. on p. 75).

[107] Juri Poutanen et al. "Spectral evolution of magnetic flares and time lags in accreting black hole sources". In: *Monthly Notices of the Royal Astronomical Society* 306.3 (July 1999), pp. L31–L37. ISSN: 0035-8711. DOI: 10.1046/j.1365-8711.1999.02735.x. eprint: https://academic.oup.com/mnras/article-pdf/306/3/L31/11934845/306-3-L31.pdf. URL: https://doi.org/10.1046/j.1365-8711.1999.02735.x (cit. on p. 18).

[108] J. E. Pringle. "Accretion discs in astrophysics". In: *The Annual Review of Astronomy and Astrophysics* 19 (Jan. 1981), pp. 137–162. DOI: 10.1146/annurev.aa.19.090181.001033 (cit. on p. 15).

[109] Dimitrios Psaltis. "Probes and Tests of Strong-Field Gravity with Observations in the Electromagnetic Spectrum". In: *Living Reviews in Relativity* 11.1, 9 (Nov. 2008), p. 9. DOI: 10.12942/lrr-2008-9. arXiv: 0806.1531 [astro-ph] (cit. on p. 7).

[110] Dimitrios Psaltis et al. "Correlations in Quasi-periodic Oscillation and Noise Frequencies among Neutron Star and Black Hole X-Ray Binaries". In: *The Astrophysical Journal* 520.1 (July 1999), pp. 262–270. DOI: 10.1086/307436. URL: https://doi.org/10.1086%2F307436 (cit. on p. 24).

[111] Pablo Reig. "Be/X-ray binaries". In: *Astrophysics and Space Science* 332.1 (Mar. 2011), pp. 1–29. DOI: 10.1007/s10509-010-0575-8. arXiv: 1101.5036 [astro-ph.HE] (cit. on p. 7).

[112] Ronald A. Remillard, Michael P. Muno, et al. "Evidence for Harmonic Relationships in the High-Frequency Quasi-periodic Oscillations of XTE J1550-564 and GRO J1655-40". In: *The Astrophysical Journal* 580.2 (Dec. 2002), pp. 1030–1042. DOI: 10.1086/343791. URL: https://doi.org/10.1086%2F343791 (cit. on p. 24).

[113] Ronald A. Remillard et al. "X-Ray Properties of Black-Hole Binaries". In: *Annual Review of Astronomy and Astrophysics* 44.1 (Sept. 2006), pp. 49–92. ISSN: 1545-4282. DOI: 10.1146/annurev.astro.44.051905.092532. URL: http://dx.doi.org/10.1146/annurev.astro.44.051905.092532 (cit. on p. 19).

[114] Peter W. A. Roming et al. “The Swift Ultra-Violet/Optical Telescope”. In: *Space Science Reviews* 120.3-4 (Oct. 2005), pp. 95–142. DOI: 10.1007/s11214-005-5095-4. URL: https://doi.org/10.1007%2Fs11214-005-5095-4 (cit. on p. 32).

[115] R. R. Ross et al. “The effects of photoionization on X-ray reflection spectra in active galactic nuclei.” In: *Monthly Notices of the Royal Astronomical Society* 261 (Mar. 1993), pp. 74–82. DOI: 10.1093/mnras/261.1.74 (cit. on p. 11).

[116] G. J. Savonije. “Roche-lobe overflow in X-ray binaries.” In: *Astronomy & Astrophysics* 62.3 (Jan. 1978), pp. 317–338 (cit. on p. 7).

[117] N. I. Shakura et al. “Black holes in binary systems. Observational appearance.” In: *Astronomy & Astrophysics* 24 (Jan. 1973), pp. 337–355 (cit. on p. 15).

[118] Stuart L. Shapiro et al. *Black holes, white dwarfs and neutron stars. The physics of compact objects*. 1983. DOI: 10.1002/9783527617661 (cit. on p. 9).

[119] Gregory J. Sobczak et al. “Correlations between Low-Frequency Quasi-periodic Oscillations and Spectral Parameters in XTE J1550–564 and GRO J1655–40”. In: *The Astrophysical Journal* 531.1 (Mar. 2000), p. 537. DOI: 10.1086/308463. URL: https://dx.doi.org/10.1086/308463 (cit. on p. 13).

[120] Aristotle Socrates et al. “Turbulent Comptonization in Black Hole Accretion Disks”. In: *The Astrophysical Journal* 601.1 (Jan. 2004), p. 405. DOI: 10.1086/380301. URL: https://dx.doi.org/10.1086/380301 (cit. on p. 16).

[121] Luigi Stella, Mario Vietri, and Sharon M. Morsink. “Correlations in the Quasi-periodic Oscillation Frequencies of Low-Mass X-Ray Binaries and the Relativistic Precession Model”. In: *The Astrophysical Journal* 524.1 (Oct. 1999), pp. L63–L66. DOI: 10.1086/312291. URL: https://doi.org/10.1086%2F312291 (cit. on p. 25).

[122] Luigi Stella et al. “Lense-Thirring Precession and Quasi-periodic Oscillations in Low-Mass X-Ray Binaries”. In: *The Astrophysical Journal* 492.1 (Jan. 1998), pp. L59–L62. DOI: 10.1086/311075. URL: https://doi.org/10.1086%2F311075 (cit. on p. 25).

[123] H. Stiele et al. “A Timing Study of MAXI J1820+070 Based on Swift/XRT and NICER Monitoring in 2018/19”. In: *The Astrophysical Journal* 889.2 (Feb. 2020), p. 142. DOI: 10.3847/1538-4357/ab64ef. URL: https://doi.org/10.3847%2F1538-4357%2Fab64ef (cit. on p. 71).

[124] A.M. Stirling et al. “A relativistic jet from Cygnus X-1 in the low/hard X-ray state”. In: *Monthly Notices of the Royal Astronomical Society* 327.4 (Nov. 2001), pp. 1273–1278. ISSN: 0035-8711. DOI: 10.1046/j.1365-8711.2001.04821.x. eprint: https://academic.oup.com/mnras/article-pdf/327/4/1273/3278054/327-4-1273.pdf. URL: https://doi.org/10.1046/j.1365-8711.2001.04821.x (cit. on p. 14).

[125] H. Tananbaum et al. “Observation of a Correlated X-Ray Transition in Cygnus X-1”. In: *The Astrophysical Journal* 177 (Aug. 1972), p. L5. DOI: 10.1086/181042 (cit. on p. 12).

[126] B. E. Tetarenko et al. “WATCHDOG: A COMPREHENSIVE ALL-SKY DATABASE OF GALACTIC BLACK HOLE X-RAY BINARIES”. In: *The Astrophysical Journal Supplement Series* 222.2 (Feb. 2016), p. 15. DOI: 10.3847/0067-0049/222/2/15. URL: https://dx.doi.org/10.3847/0067-0049/222/2/15 (cit. on p. 10).

[127] Lev Titarchuk et al. “Observational Signatures of Black Holes: Spectral and Temporal Features of XTE J1550–564”. In: *The Astrophysical Journal* 567.2 (Mar. 2002), p. 1057. DOI: 10.1086/338661. URL: https://dx.doi.org/10.1086/338661 (cit. on p. 18).

[128] Lev Titarchuk et al. “Spectral Index and Quasi-Periodic Oscillation Frequency Correlation in Black Hole Sources: Observational Evidence of Two Phases and Phase Transition in Black Holes”. In: *The Astrophysical Journal* 612.2 (Sept. 2004), pp. 988–999. DOI: 10.1086/422573. URL: https://doi.org/10.1086%2F422573 (cit. on p. 25).

[129] John A. Tomsick et al. “Broadband X-Ray Spectra of the Black Hole Candidate GRO J1655-40”. In: *The Astrophysical Journal* 512.2 (Feb. 1999), pp. 892–900. DOI: 10.1086/306797. arXiv: astro-ph/9809098 [astro-ph] (cit. on p. 13).

[130] M. A. P. Torres, J. Casares, F. Jiménez-Ibarra, A. Álvarez-Hernández, et al. “The Binary Mass Ratio in the Black Hole Transient MAXI J1820+070”. In: *The Astrophysical Journal* 893.2 (Apr. 2020), p. L37. ISSN: 2041-8213. DOI: 10.3847/2041-8213/ab863a. URL: http://dx.doi.org/10.3847/2041-8213/ab863a (cit. on p. 28).

[131] M. A. P. Torres, J. Casares, F. Jiménez-Ibarra, T. Muñoz-Darias, et al. “Dynamical Confirmation of a Black Hole in MAXI J1820+070”. In: *The Astrophysical Journal* 882.2 (Sept. 2019), p. L21. ISSN: 2041-8213. DOI: 10.3847/2041-8213/ab39df. URL: http://dx.doi.org/10.3847/2041-8213/ab39df (cit. on p. 74).

[132] Roberto Turolla et al. “Power-Law Tails from Dynamical Comptonization in Converging Flows”. In: *The Astrophysical Journal* 576.1 (Sept. 2002), p. 349. DOI: 10.1086/341631. URL: https://dx.doi.org/10.1086/341631 (cit. on p. 18).

[133] Y. Ueda et al. *Errarum: Detection of Absorption-Line Features in the X-Ray Spectra of the Galactic Superluminal Source GRO J1655-40*. The Astrophysical Journal, Volume 500, Issue 2, pp. 1069-1069. June 1998. DOI: 10.1086/305784 (cit. on p. 75).

[134] P. Uttley et al. “NICER observations of MAXI J1820+070 suggest a rapidly-brightening black hole X-ray binary in the hard state”. In: *The Astronomer’s Telegram* 11423 (Mar. 2018), p. 1 (cit. on p. 29).

[135] Jingyi Wang, Erin Kara, et al. “The NICER “Reverberation Machine”: A Systematic Study of Time Lags in Black Hole X-Ray Binaries”. In: *The Astrophysical Journal* 930.1 (May 2022), p. 18. ISSN: 1538-4357. DOI: 10.3847/1538-4357/ac6262. URL: http://dx.doi.org/10.3847/1538-4357/ac6262 (cit. on p. 74).

[136] Jingyi Wang, Guglielmo Mastroserio, et al. “Disk, Corona, Jet Connection in the Intermediate State of MAXI J1820+070 Revealed by NICER Spectral-timing Analysis”. In: *The Astrophysical Journal Letters* 910.1 (Mar. 2021), p. L3. DOI: 10.3847/2041-8213/abec79. URL: https://doi.org/10.3847%2F2041-8213%2Fabec79 (cit. on pp. 29, 69, 70, 73–75).

[137] Alan A. Wells, C.M. Castelli, et al. “X-ray imaging performance of the flight model JET-X telescope”. In: *EUV, X-Ray, and Gamma-Ray Instrumentation for Astronomy VIII*. Ed. by Oswald H. W. Siegmund et al. Vol. 3114. International Society for Optics and Photonics. SPIE, 1997, pp. 392–403. DOI: 10.1117/12.283782. URL: https://doi.org/10.1117/12.283782 (cit. on p. 32).

[138] Alan A. Wells, G. C. Stewart, et al. “JET-X instrument for the USSR Spectrum-RG mission: its design and performance”. In: *Multilayer and Grazing Incidence X-Ray/EUV Optics*. Ed. by Richard B. Hoover. Vol. 1546. International Society for Optics and Photonics. SPIE, 1992, pp. 205–220. DOI: 10.1117/12.51259. URL: https://doi.org/10.1117/12.51259 (cit. on p. 32).

[139] Ralph A. M. J. Wijers et al. “Warped accretion discs and the long periods in X-ray binaries”. In: *Monthly Notices of the Royal Astronomical Society* 308.1 (Sept. 1999), pp. 207–220. ISSN: 1365-2966. DOI: 10.1046/j.1365-8711.1999.02720.x. URL: http://dx.doi.org/10.1046/j.1365-8711.1999.02720.x (cit. on p. 57).

[140] R. Wijnands, J. Homan, et al. “The Complex Phase-Lag Behavior of the 3–12 H[CLC]z[/CLC] Quasi-Periodic Oscillations during the Very High State of XTE J1550-564”. In: *The Astrophysical Journal* 526.1 (Nov. 1999), pp. L33–L36. DOI: 10.1086/312365. URL: https://doi.org/10.1086%2F312365 (cit. on p. 24).

[141] R. Wijnands et al. “The Broadband Power Spectra of X-Ray Binaries”. In: *The Astrophysical Journal* 514.2 (Apr. 1999), p. 939. DOI: 10.1086/306993. URL: https://dx.doi.org/10.1086/306993 (cit. on p. 24).

[142] J. Wilms et al. “On the Absorption of X-Rays in the Interstellar Medium”. In: *The Astrophysical Journal* 542.2 (Oct. 2000), pp. 914–924. ISSN: 1538-4357. DOI: 10.1086/317016. URL: http://dx.doi.org/10.1086/317016 (cit. on p. 51).

[143] Yanjun Xu et al. “Evidence for Disk Truncation at Low Accretion States of the Black Hole Binary MAXI J1820+070 Observed by NuSTAR and XMM-Newton”. In: *The Astrophysical Journal* 893.1 (Apr. 14, 2020), p. 42. ISSN: 1538-4357. DOI: 10.3847/1538-4357/ab7cdb. arXiv: 2003.01778[astro-ph]. URL: http://arxiv.org/abs/2003.01778 (visited on 01/23/2023) (cit. on p. 75).

[144] Feng Yuan et al. “An Accretion-Jet Model for Black Hole Binaries: Interpreting the Spectral and Timing Features of XTE J1118+480”. In: *The Astrophysical Journal* 620.2 (Feb. 2005), p. 905. DOI: 10.1086/427206. URL: https://dx.doi.org/10.1086/427206 (cit. on p. 17).

[145] Olindo Zanotti et al. “Dynamics of oscillating relativistic tori around Kerr black holes”. In: *Monthly Notices of the Royal Astronomical Society* 356.4 (Feb. 2005), pp. 1371–1382. DOI: 10.1111/j.1365-2966.2004.08567.x. arXiv: astro-ph/0411116 [astro-ph] (cit. on p. 73).

[146] A. A. Zdziarski et al. “Broad-band gamma-ray and X-ray spectra of NGC 4151 and their implications for physical processes and geometry”. In: *Monthly Notices of the Royal Astronomical Society* 283.1 (Oct. 1996), pp. 193–206. ISSN: 1365-2966. DOI: 10.1093/mnras/283.1.193. URL: http://dx.doi.org/10.1093/mnras/283.1.193 (cit. on p. 51).

[147] Andrzej A. Zdziarski, Marek Gierlinski, et al. “GRS 1915+105: the distance, radiative processes and energy-dependent variability”. In: *Monthly Notices of the Royal Astronomical Society* 360.3 (July 2005), pp. 825–838. ISSN: 0035-8711. DOI: 10.1111/j.1365-2966.2005.09112.x. eprint: https://academic.oup.com/mnras/article-pdf/360/3/825/3195244/360-3-825.pdf. URL: https://doi.org/10.1111/j.1365-2966.2005.09112.x (cit. on p. 17).

[148] Andrzej A. Zdziarski et al. “Radiative Processes, Spectral States and Variability of Black-Hole Binaries”. In: *Progress of Theoretical Physics Supplement* 155 (May 2004), pp. 99–119. ISSN: 0375-9687. DOI: 10.1143/PTPS.155.99. eprint: https://academic.oup.com/ptps/article-pdf/doi/10.1143/PTPS.155.99/5353498/155-99.pdf. URL: https://doi.org/10.1143/PTPS.155.99 (cit. on p. 17).

[149] S. N. Zhang, W. Cui, et al. “The 1996 Soft State Transition of Cygnus X-1”. In: *The Astrophysical Journal* 477.2 (Mar. 1997), pp. L95–L98. DOI: 10.1086/310530. arXiv: astro-ph/9701027 [astro-ph] (cit. on p. 13).

[150] S. N. Zhang, Wei Cui, et al. “Black Hole Spin in X-Ray Binaries: Observational Consequences”. In: *The Astrophysical Journal* 482.2 (June 1997), pp. L155–L158. ISSN: 0004-637X. DOI: 10.1086/310705. URL: http://dx.doi.org/10.1086/310705 (cit. on p. 16).

[151] E. R. Zimmerman et al. “Multitemperature Blackbody Spectra of Thin Accretion Disks with and without a Zero-Torque Inner Boundary Condition”. In: *The Astrophysical Journal* 618.2 (Jan. 2005), p. 832. DOI: 10.1086/426071. URL: https://dx.doi.org/10.1086/426071 (cit. on p. 16).

[152] P. T. Zycki et al. “The 1989 May outburst of the soft X-ray transient GS 2023+338 (V404 Cyg)”. In: *Monthly Notices of the Royal Astronomical Society* 309.3 (Nov. 1999), pp. 561–575. ISSN: 1365-2966. DOI: 10.1046/j.1365-8711.1999.02885.x. URL: http://dx.doi.org/10.1046/j.1365-8711.1999.02885.x (cit. on p. 51).